A Computational Analysis of the Leading-Edge Vortex Dynamics and its Control During Transient Pitching Cycles

Quentin Martinez

Doctor of Philosophy

City St. George's, University of London

Department of Engineering

08-2026

Declaration

I, Quentin Martinez confirm that the work presented in this thesis is my own. Where information has been derived from other sources, I confirm that this has been indicated in the thesis.

Acknowledgements

To my academic advisors, Dr. Mohammad Omidyeganeh, Dr. Chetan Jagadeesh, and Dr. Marinos Manolesos, thank you all for always providing support related to my research, health, and stability throughout this project. I am grateful to have worked and learned alongside each of you.

To my friends and family back home, thank you for the years of continued comfort, engagement, and shared laughs while I have studied abroad. I look forward to seeing where your futures lead you and endeavour to always remain close.

To Chris Marshall, thank you for recovering my data after I executed ‘rm -r’ on my entire working directory prior to submission.

To the Kiran Family, thank you for your mentorship throughout my academic career and support during my MSc program. I always enjoy our visits in London and hope to continue these international meetings for many years to come.

Finally, to my parents, Christine and Medardo Martinez, I would like to thank you for all the years of support and love that you have provided to help foster my professional and personal growth. I am immensely grateful for your efforts to ensure I always had opportunities to explore my interests in science, sports, and art throughout my childhood. I would also like to thank you for the countless travel hours spent between home and my continuously eastward migration around the globe. Thank you, Nacho and Cooper for being good boys.

Table of Contents

List of Figures

List of Tables

“And thence we came forth to see again the stars.”

— Dante Alighieri, *Inferno*, Canto XXXIV, line 139

Chapter 1

1.1 Introduction

In an effort to combat global greenhouse gas (GHG) emissions, sustainable energy harvesting alternatives like offshore wind turbines have garnered international attention across industrial, legislative, and academic sectors. Despite substantial efforts to enhance wind turbine efficiency and aggregate power output in large-scale farms, structural fatigue related downtime remains to be a considerable logistical and financial burden. Some authors have estimated between 4% and 10% average downtime for offshore wind turbines (Horn and Leira, 2019) due to a combination of electrical and mechanical failures. Cevasco et al. (2021), reported an appreciably larger downtime range, 0.9-19.8%, based on a comprehensive survey of various reliability studies in Europe. They also note a disparity in operational availability between mega-watt range, off and onshore wind turbines (onshore being less susceptible to failure) supported by a prior correlation of turbine failure rate and unfavourable environmental conditions (Tavner et al., 2012).

To broaden the mechanical lifetime of offshore wind turbines, modern research efforts have been focused towards structural fatigue mitigation by means of both active and passive flow control devices. Commonly employed devices/technologies include camber morphing, pop-up tabs, suction/blowing, and variations thereof (Gardner et al., 2023). The primary end-goal of such devices is to assist in load alleviation during transient conditions like gusts, crosswinds, or wake that can potentially excite a dynamic aeroelastic response of the wind turbine blades during operational and stand still conditions. When operating at high mean incidence angles, this response to volatile environmental conditions can be further augmented due to various dynamic stall related events. In general, these events consist of the formation, migration, and detachment of a strong leading-edge vortex (LEV) from the aerofoil which are essential for driving the single degree of freedom instability known as stall flutter (Dimitriadis and Li, 2009). Prolonged exposure to these conditions can lead to sustained oscillations causing premature wind turbine blade wear, mechanical failure, and eventual decommissioning. Thus, accurately characterising these dynamic stall related events is a crucial endeavour to inform design strategies and operational regimes that alleviate unwanted aerodynamic loading and vibratory modes.

The dynamic stall processes during high amplitude aeroelastic pitching cycles and its induced effects are highly nonlinear due to a complex coupling between inertial, restorative, and aerodynamic forces. This coupling has shown to be sensitive to various operational parameters such as the reduced frequency, aerofoil shape, and free stream turbulence intensity, for example. Consequently, the rich fluid dynamics associated with stall flutter has been mostly restricted to a phenomenological understanding of how the LEV contributes to unsteady aerodynamic loading and energy extraction rather than an analytical one. During transient conditions like aeroelastic starting cycles or one-shot pitching/plunging motions, this knowledge gap is even more evident. This is because stall flutter is known to approach a limit cycle oscillation (LCO) (Culler and Farnsworth, 2019) where initial transients are effectively ‘washed out’ at sufficiently long timescales. Though, the transient dynamic stall processes that precede stable orbits are critically important from the purview of topics such as subcritical bypass transition, non-normality, and stall flutter suppression. Specifically, the LEV saturation and detachment phenomenon are sources of nonlinearity that have proven difficult to incorporate in reduced order models. Thus, a step-change in our understanding of these processes through high fidelity simulations is warranted for informing industry relevant objectives such as modelling, mapping operational envelopes, and designing flow control methods.

One promising method to achieve active load attenuation is by using aerofoil surface blowing. Several groups (Chen et al., 2022), (Müller-Vahl et al., 2015), (Seidel, Fagley and McLaughlin, 2015) have implemented constant blowing via surface jet to successfully suppress dynamic stall events in high amplitude aeroelastic pitching cycles. One mechanism responsible for this achievement is attributed to an injection of chordwise momentum which aids in delaying trailing-edge flow separation (Towne and Buter, 1994). This can be achieved via 'tangential' or nearly tangential jet orientations relative to the aerofoil surface such that the boundary layer attachment is maintained during high amplitude pitching motions. By delaying stall, the leading-edge shear layer development and vortex rollup are absent which promotes positive aerodynamic damping. Consequently, the stall flutter instability can either be maintained at a lower amplitude or suppressed entirely making it an effective method for fatigue mitigation in large-scale wind turbines. Though, this capability requires careful tuning of the jet intensity/momentum injection to be effective. For example, the required momentum injection from a constant blowing jet increases when transitioning between shallow and deep dynamic stall regimes to maintain boundary layer attachment (Gardner et al., 2023). This potentially makes active blowing quite expensive to apply in practice due to control system requisites such as the jet influx rate. Thus, it is crucial to explore an active jet control authority that satisfies a conservative influent capacity. Current efforts in this faculty have sought the use of adaptive (Müller-Vahl et al., 2016) or scheduled jet pulses (Kim and Jee, 2023) to disrupt the dynamic stall process without the need for constant blowing. While both methods demonstrated potential for unsteady aerodynamic load alleviation in flexible structures, the parameter space encompassing this control authority remains largely unexplored. In particular, the role of the jet orientation angle in scheduled blowing has not been thoroughly examined within the current literature. Consequently, an investigation into conservative control authorities that can achieve unsteady aerodynamic load attenuation but at a reduced injection cost, i.e. lower momentum influx or jet intensity, is fundamentally necessary for deployment in real-world engineering systems.

1.2 Objectives

The objectives of this thesis are two-fold as an understanding of the transient dynamic stall processes is complementary to controlling unsteady aerodynamic loads at high mean incidence angles. First, we aim to provide fresh insight into the dynamic stall processes by rigorously analysing the leading-edge vortex dynamics during stall flutter starting cycles via high fidelity large-eddy simulations (LES) and over a wide range of parametric conditions. This transient aeroelastic regime is largely unexplored but is important for understanding how the stall flutter instability is first enabled. An emphasis will be placed on the LEV detachment process and its initiating mechanism as these remain to be highly complex fluid dynamic phenomena that complicate reduced order modelling. We will attempt to link the unsteady aerodynamic loading to the LEV state by using a range of conventional and unique descriptors/metrics like its morphology, trajectory path, strength, etc. These will be necessary to help identify tendencies that can either promote or attenuate unsteady aerodynamic loads.

Next, an assessment of surface jet blowing will be conducted to inform how the dynamic stall processes are altered during transient starting cycles. We will assess the implications of the jet orientation angle on scheduled jet blowing for LEV control. This is warranted because surface jets operating at non-optimal conditions have the potential to interact with the LEV development but not completely suppress the dynamic stalling process. In some cases, surface jet blowing can even encourage the LEV growth which may be detrimental to flexible aeroelastic systems. Thus, it is important to consider parametric influences that either attenuate or encourage transient aerodynamic load augmentation. This investigation will provide new insight into a relatively unexplored control parameter space regarding actuated blowing as it is typically difficult to vary the jet orientation during experimental campaigns.

1.3 Outline

The contents of this thesis consist of several chapters that aim to address the aforementioned project objectives. Chapter 2: a literature review on stall flutter, LEV dynamics, and control of the dynamic stall process. Chapter 3: a methodological summary of our numerical simulation setup, its implementation, and an experimental validation study. Chapters 4-7: results highlighting a range of parametric influences on the transient dynamic stall process including the reduced frequency, mean incidence angle, and perturbation starting time. An emphasis is placed on the LEV detachment mechanism and its variability in single shot pitching cycles. The suppression/disruption effects of surface jet blowing on this transient dynamic stall process is assessed as a potential active flow control method. Specifically, we assess how the LEV development process is altered by varying the jet orientation angle in actuated jet blowing scenarios. Finally, a novel vortex tracking pipeline is proposed to aid in future numerical campaigns related to stall flutter and dynamic stall. Conclusions are drawn regarding the evolution and control of the LEV structure in transient pitching cycles. Future work paths are presented to bridge these results between a theoretical and applied framework in real-world aeroelastic systems.

The following conference proceedings and journal manuscripts form the basis of this thesis where I contributed to the code base development, data processing, analysis, and writing. Specifically, I updated our in-house Navier-Stokes solver to simulate the aeroelastic pitching motion of a NACA 63(3)418 aerofoil section with a toggle capability for flow control via surface jet blowing. Most of the data analysis was conducted using bespoke Matlab or Python scripts that I developed throughout my candidacy. Finally, I designed and fabricated a wall-to-wall wing section for experimental validation of our computational results.

1) Transient Leading-Edge Vortex Dynamics and its Role in Unsteady Aerodynamic Load Variations. *Physics of Fluids*. 30/01/2026. DOI: 10.1063/5.0310207.

2) Leading-Edge Vortex Monitoring in Dynamically Stalled Flows via Persistent Homology. *Computers and Fluids*. 29/11/2025. DOI: 10.1016/j.compfluid.2025.10693.

3) High Amplitude Stall Flutter Simulations of a NACA 63(3)418 Aerofoil. *AIAA Aviation Forum and Ascend 2025 Proceedings*. 16/07/2025. DOI: 10.2514/6.2025-3839.

4) Large Eddy Simulations of a NACA 63(3)418 Aerofoil Undergoing One-Shot Starting Cycles at Highly Unsteady Conditions. *59th 3AF International Conference on Applied Aerodynamics*. 26/03/25. DOI: 10.60711/AERO2025.20250402.8753383450051228.

5) Effects of the jet angle orientation on actuated blowing for leading-edge vortex control. *Journal of Fluids and Structures*. Manuscript submitted on 01/02/26.

Chapter 2

2.1 Stall Flutter

Preceding the so called 'stalling flutter' phenomenon, international scale research regarding the classical bending-torsion flutter was already prevalent throughout the 1920's. Studer's (1936) pioneering experimental campaign demonstrated that critical flutter speeds drop significantly near the stall angle of attack where a new flutter type instability was shown to be possible in a single degree of freedom. Bollay and Brown (1941) and Victory (1943) later confirmed that the decrease in critical flutter speed near stall could be attributed to a variation in torsional aerodynamic damping with incidence. It was then speculated that the stall flutter phenomenon manifests as a combination of 3 potential instability sources (Mendelson, 1948):

1) A static instability condition associated with a negative slope in the lift polar above the stall angle of attack.

2) Kármán vortices shed at a frequency coincident with the natural frequency of the system.

3) Energy extraction due to a complex hysteresis effect in the aerodynamic loading of an oscillating aerofoil caused by the LEV structure.

While these conditions are not mutually exclusive, it is generally accepted that condition three is the most dominant contribution to the stall flutter instability and has been a primary source of investigation for several decades. Carta and Niebanck (1969) ascribed the stall flutter stability criteria to the aerodynamic damping coefficient (eqn. 1). A negative damping coefficient indicates energy extraction while a positive value indicates energy dissipation.

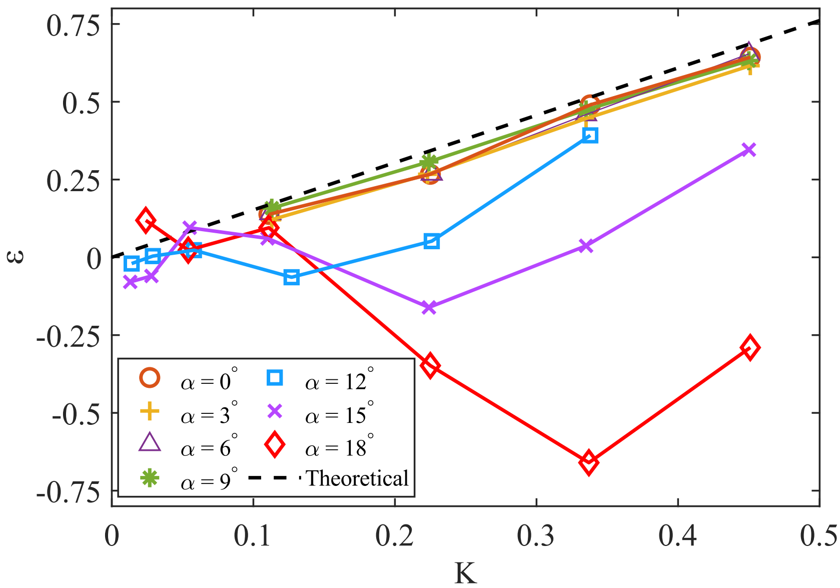

Figure 1. *Effect of incidence angle on predicted aerodynamic damping coefficient, sourced and adapted from Carta and Niebanck (1969). ε and K are the aerodynamic damping coefficient (eqn. 1) and the reduced frequency (eqn. 48), respectively.*

C_w is the dimensionless form of the per-cycle energy transfer between the free stream fluid and aeroelastic system which can be evaluated experimentally by computing the area enclosed in a pitching moment loop. Note that $\bar{\alpha}$ is the pitching amplitude taken in radians and is typically computed as a phase average over many cycles ($N > 10$). U_∞, c, and ρ are the free stream velocity, aerofoil chord, and fluid density, respectively.

$$\varepsilon = -\frac{C_w}{\pi\bar{\alpha}^2} \qquad (1)$$

$$C_w = \frac{W}{0.5\rho U_\infty^2 c^2} = \oint C_M d\bar{\alpha} \qquad (2)$$

For low angles of attack in a pitch degree of freedom system, this damping parameter is always positive and well predicted by an idealised potential flow. Near the static stall angle though, this value tends to become negative and deviates severely from theoretical expectations as shown in figure 1.

The fluid dynamic mechanisms that give rise to this discrepancy are largely attributed to a complex dynamic stall process which has mostly been treated from a statistical, empirical, or phenomenological perspective. Carr et al. (1977) were some of the first authors to describe, in detail, the events and phenomenology associated with dynamic stall in an experimental setting. The characteristics of this process are only summarised here for brevity. In general, the dynamic stall process consists of five distinct stages:

1) The static stall angle is exceeded while flow remains attached to the suction side surface. Incipient flow reversal is present, but the boundary layer remains completely attached. This is not the case for a static aerofoil where the flow reversal and boundary layer separation point are coincident.

2) The leading-edge shear layer continuously feeds the dynamic stall induced LEV. This leads to an augmentation in lift beyond static conditions.

3) As the LEV is advected over the aerofoil surface, its trajectory influences a chordwise shift in the centre of pressure. This influences a pitch down moment known as 'moment stall'.

4) The LEV structure reaches its terminal position along the aerofoil chord and separates from the suction surface. This leads to a dramatic reduction in lift termed conventionally as 'dynamic lift stall'.

5) The pitch-down motion of the aerofoil allows for fluid recovery starting from the leading-edge to the trailing edge, re-introducing a positive pitching moment. Complete flow reattachment occurs at an angle less than its static counterpart.

These stages have also been referred to as: the flow stage; the stall development stage; stall onset stage; the stalled stage; and flow reattachment stage (Mulleners and Raffel, 2012). An overview schematic description of this process for the case for an aerofoil pitching about $x = 0.25c$ is provided in figure 2 where the dashed blue line indicates the static lift and moment polars. Note that moving the flexural axis rearward alters the phase angle when moment stall occurs.

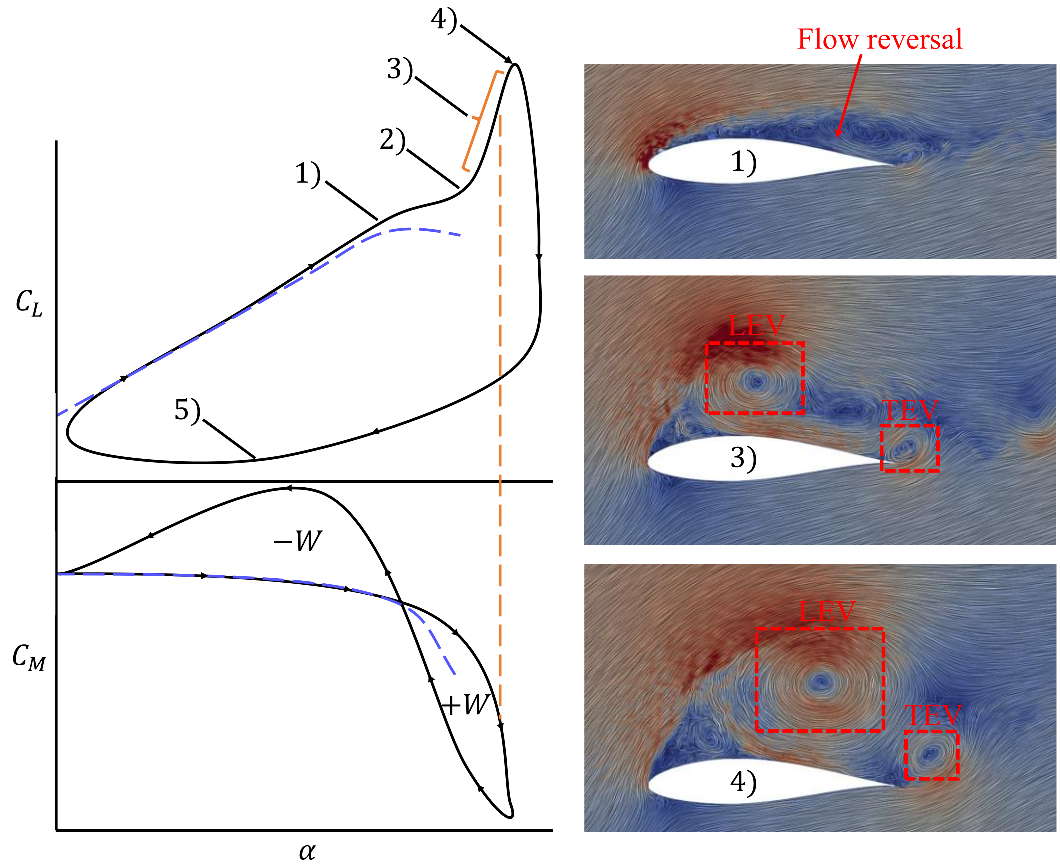

Figure 2. *Lift and moment hysteresis schematic for a pitching aerofoil. Velocity magnitude contours with line integral convolution overlay are shown to highlight different canonical stages of the dynamic stall process. Contour scaled between,* $0 \leq \|\boldsymbol{u}\| \leq 2.3$.

These fluid dynamic events lead to a complicated loading hysteresis which accounts for, in part, the highly non-linear behaviour of stall flutter. Stall flutter is often conflated with the flow-physics associated with prescribed oscillatory motions (usually sinusoidal) near the stall angle of attack. At this point it should be made fervently clear that whilst interconnected phenomena, stall flutter and dynamic stall are distinct. Dimitriadis and Li (2009) clarified this notion by stating that dynamic stall is a purely aerodynamic phenomenon while stall flutter is a limited amplitude instability caused by the interaction of dynamic stall events coupled with the structural characteristics of a wing. Throughout this thesis, the term 'dynamic stall process' is only used to describe the generalised flow stages encountered during these transient pitching cycles.

The stall flutter instability manifests as a supercritical Hopf bifurcation when varying a critical bifurcation parameter such as the free stream speed. This can be considered as a soft route to stall flutter as the instability gradually grows to form an LCO. Conversely, it has also been shown that environmental impulses like gusts can trigger a subcritical transition to flutter even when operating below the critical flutter speed (Schwartz et al., 2009). This can be the result of a phenomenon known as transient energy growth that leads to a temporary amplification of energy occurring both in linear and nonlinear systems (Schmid and de Langre, 2003). These routes are exemplified in figure 3 where the '2' and '3' traces represent the subcritical and supercritical flutter routes subject to an initial impulse, respectively.

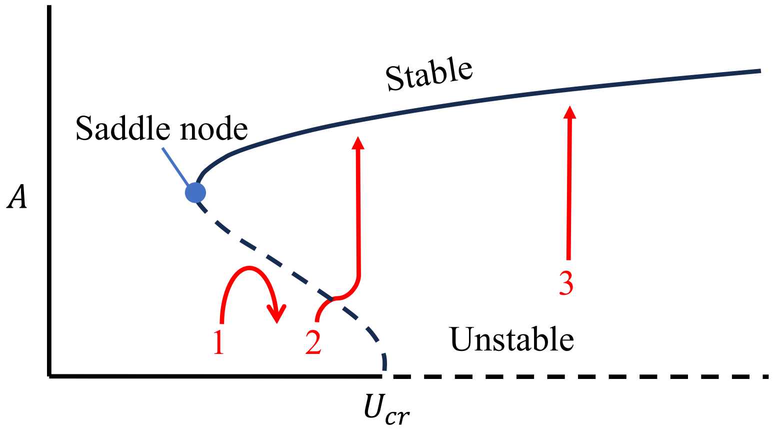

Figure 3. *Stall flutter stability diagram with three possible routes. 1) Transient energy growth decays back to stable branch. 2) Transient energy growth with bypass transition to LCO. 3) Fully unstable regime. Dashed and bold lines represent the repelling and attracting branches of a dynamical system. Saddle node indicates where the stable and unstable equilibria annihilate as the free stream speed is reduced below a critical free stream speed,* U_{cr}.

A subcritical route to stall flutter is highly dependent on the initial conditions produced by the perturbation as the transient energy amplification may still be insufficient to achieve bypass transition (trace '1' in figure 3). Conventional transition to a stable orbit can also occur if the initial impulse is simply strong enough to traverse the unstable branch. These instability routes have prompted efforts to explore gust, wake, impulse, or other transient conditions to better understand subcritical transition and how to mitigate this phenomenon in real-world operating environments (Schwartz et al., 2009), (Wang and Feng, 2025), (Whiting et al., 2005). To this end though, the transient fluid dynamic conditions that permit this behaviour are still not fully understood. This is because transient dynamic stall processes can be weakly repeatable if, for example, the generated LEV motion is not synchronous with the static aerofoil shed wake (Fernandez et al., 2021). This out-of-lock condition was shown to cause massive variations in the LEV position and size when subjected to gust impulses. Menon and Mittal (2019) demonstrated a similar transient discrepancy when applying a small pitching perturbation to their aeroelastic system that varied within the shedding wake phase angle. It was shown that the unsteady pitching moment coefficient can experience large variations due to either constructive or destructive fluid-structure interactions. Thus, better understanding of transient dynamic stall processes preceding either sustained or convergent aeroelastic behaviour is necessary to help mitigate unwanted aerodynamic load augmentation.

2.2 Leading-Edge Vortex Dynamics

The dynamic stall process is widely recognised as the primary driving mechanism for stall flutter in aeroelastic systems. Research within this faculty typically requires instantaneous field snapshots or phase averaged snapshots to accurately determine the causality of meaningful fluid dynamic interactions that permit this instability. While the dynamic stall process generally encompasses the complete fluid dynamic trajectory during high amplitude pitching cycles, the LEV dynamics can be further condensed into a subset of the aeroelastic pitching motion that encompass its attachment, transition, and detachment stages. When analysing this subset, the position and strength of the LEV structure are two of the most commonly quantified metrics that are used to link the chronology of the LEV dynamics events to unsteady aerodynamic loading (Mulleners and Raffel, 2013), (Lee et al., 2022), (Prangemeier et al., 2010). It has been shown that the LEV roll-up dynamics and its incipient formation have demonstrated a degree of repeatability across various numerical and experimental campaigns. For example, (Li et al., 2020) found that the LEV trajectory in both one-shot and cyclically prescribed motions of a flat plate experiences an approximately linear path during its formation and attachment stage. When varying the maximum effective incidence angle between $\alpha = 16^{\circ}$ and $\alpha = 24^{\circ}$, the time-dependant strength of the LEV also grew approximately linearly up to a saturation point that precedes its detachment from the flat plate. Lee et al. (2022) demonstrated nearly linear LEV trajectories for a pitching aerofoil prior to saturation. They also showed that Q-criterion point clouds within this linear regime are tightly clustered indicating a strongly coherent vortical structure. Kissing et al. (2020) showed that the LEV strength grows in an approximately linear fashion up until some critical saturation point. These tendencies point towards repeatable and scalable LEV dynamics over a range of parametric conditions that are well predicted by reduced order models.

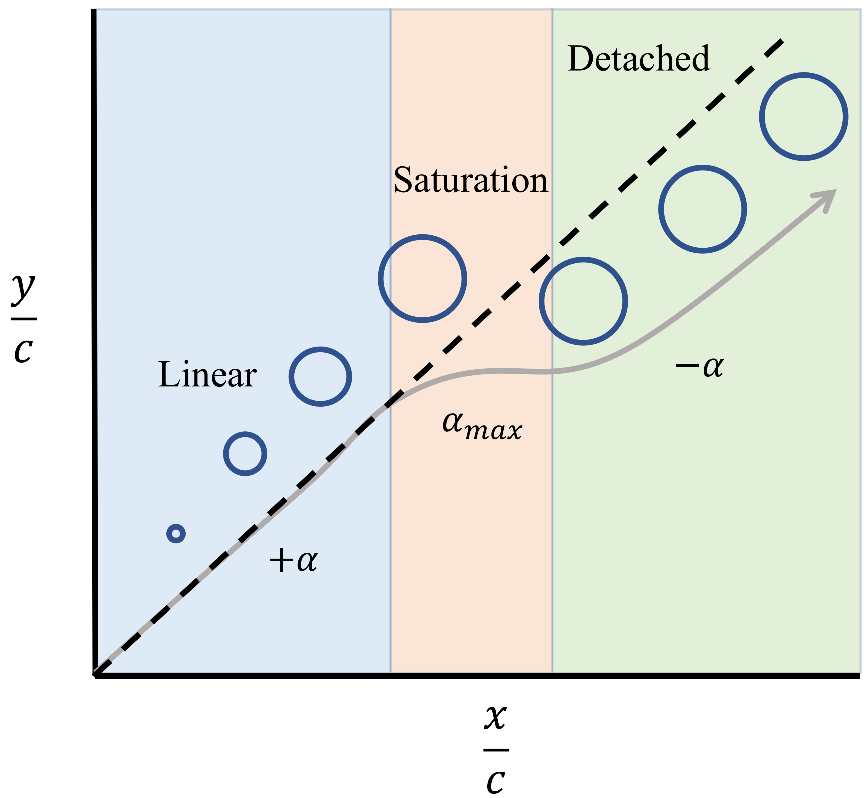

Figure 4. *LEV growth and trajectory schematic for a generalised dynamic stall process.*

Conversely, many authors have reported strong variations in the LEV detachment and recovery regime that has made post-stall aerodynamic loading quite difficult to predict (Damiola et al., 2024), (Mulleners and Raffel, 2013), (Gardner et al., 2023). This variability has been linked to the semi-stochastic nature of the boundary layer when fully stalled (Gardner et al., 2023), (Küppers and Reinicke, 2022). Other groups have attributed this variability to secondary vortex interactions with the LEV structure (Tseng and Cheng, 2015). Indeed, the LEV dynamics within this regime are complicated by parametric sensitivities that are relatively dormant within the linear portion of this lifecycle. For this reason, the LEV detachment mechanism and its initiating criteria have received significant attention to help clarify this post-stall variability.

Currently, several LEV detachment mechanism(s) associated with pitching or plunging lifting body motions have been proposed within the literature. One accepted mechanism is termed as a 'spike' where boundary layer eruption ahead of the LEV aids in severing its source vorticity (Doligalski et al., 1994). This type of mechanism can lead to the LEV detachment that is independent of the aerofoil chord. A second, inviscid detachment mechanism has also been proposed due to a trailing-edge interaction with the LEV. (Kissing et al., 2020) observed that the termination of vorticity accumulation in the LEV is correlated to a counter-rotating circulation event about the trailing-edge. More specifically, as the rear stagnation point of the LEV passes beyond the trailing-edge, fluid becomes entrained between the fluid structure and suction side surface acting to restrict vorticity influx to the LEV. This introduces counter-rotating fluid between the lifting body surface and LEV that acts to sever the supplying shear layer to this structure (Kissing et al., 2020). Topologically, this detachment mechanism can be described in figure 5 as the downstream merging of 2 half-saddle nodes, $S_5{}'$ and $S_6{}'$, about the trailing edge to create a full saddle (Rival et al., 2014). This detachment mechanism has been referred to as a 'bluff body' type.

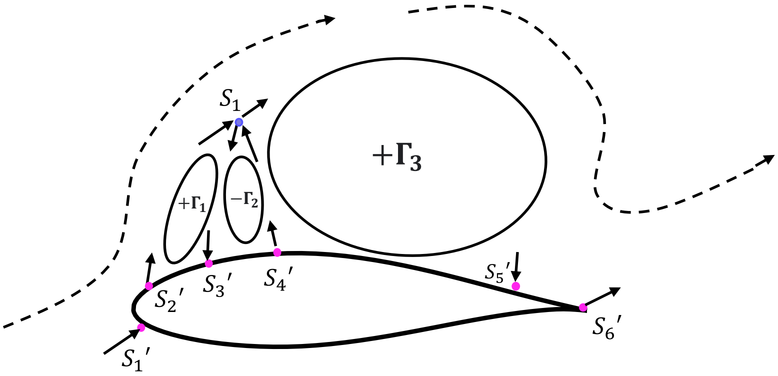

a)

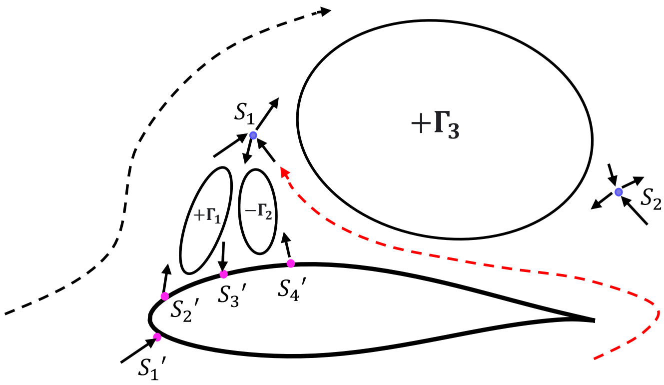

b)

***Figure 5**. Topological scenarios representing a) LEV growth over aerofoil and b) 'bluff body' detachment due to merging of downstream half saddle nodes.*

Here, $S_i{}'$ and S_i indicate half saddle and full saddle nodes, respectively. This particular mechanism implicates that the profile chord is the most relevant detachment length scale. A tertiary detachment mechanism has been demonstrated where early LEV drifting is possible across various parametric conditions like the aerofoil chord thickness, for example. This is due to an invasive interaction with a counter rotating vortex that migrates onto the suction side surface. Jain and Saha, (2020) demonstrated that for relatively thick aerofoils, $\frac{t}{c} = 21\%$, a TEV can form which tends to impede both the motion and growth of an LEV. For a reflex cambered aerofoil, a similar phenomenon was also observed which reduced the cycle-averaged aerodynamic loads due to early snap-off (Xing, Xu and Zhang, 2022).

These mentioned scenarios are non-exhaustive but provide a testimony as to the variability and complexity of observed LEV detachment processes. These mechanisms and their respective initiating criteria complicate the phenomenology of dynamically stalled flows by introducing strongly nonlinear interactions between primary and secondary flow structures and the lifting body. During transient pitching cycles, understanding the range of this variability is necessary when implementing active flutter suppressions methods to determine suitable operating regimes.

2.3 Control of Dynamically Stalled Flows

To effectively suppress the stall flutter instability, several active and passive flow control methods have been proposed to alter or completely eliminate the dynamic stall events present during high amplitude pitching/plunging scenarios. By doing so, the coupling between inertial, structural, and aerodynamic forces can become energy defeating which is beneficial for susceptible structures like wind-turbine blades, for example. Various methods have been proposed and applied successfully such as pop-up flaps, camber-morphing, slats, jets, and more. The wide-ranging mechanisms that enable this energy deficit are inherently based on the type of flow control method utilised. See Gardner et al., (2023) for a review of current methods used for controlling dynamic stall. For this work though, we will focus primarily on surface jets as an active flow control technique for stall flutter suppression.

Active blowing for flow control has received tremendous attention across various engineering disciplines owing to its inherent methodological simplicity. Towne and Buter (1994) demonstrated quiet early on that tangential blowing, applied near the leading-edge of an aerofoil, can delay the onset of dynamic stall and increase the lift coefficient over a wide range of incidence angles. A schematic example of this type of setup is given in figure 6 for reference.

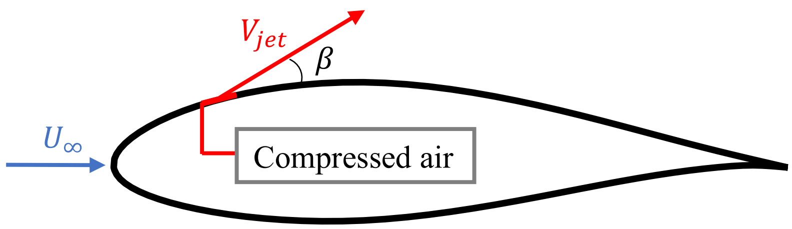

Figure 6. *Schematic of a jet flow control authority along a small suction side patch. β represents the jet orientation angle relative to the aerofoil tangent.*

The delaying mechanism was attributed to an increase of near-surface momentum that keeps reverse-flowing fluid from pooling under the leading-edge shear layer. More recent efforts have demonstrated that constant leading-edge blowing can increase the critical bifurcation velocity for stall flutter (Chen et al., 2022). This was done by either promoting early LEV shedding or delaying the LEV formation. Both cases are favourable from the purview of stall flutter suppression or delay. Müller-Vahl et al. (2015) showed via particle image velocimetry (PIV) that a leading-edge blowing slot is more favourable for attenuating the formation of an LEV than a mid-chord slot. They also showed that leading-edge separation can be promoted if the injection momentum is not high enough. In this case, the LEV lifecycle may not be suppressed but altered. Weaver, McAlister and Tso (2004) demonstrated experimentally that tangential blowing modified the shape of the moment hysteresis during dynamic stall such that positive aerodynamic damping was achieved. In many case studies implementing constant blowing, the jet momentum coefficient, is the primary parameter of concern. This is given by equation 3 where, $\dot{m}_j$, V_j, and S are the jet mass flow rate, jet speed, and aerofoil projected area, respectively.

$$C_\mu = \frac{\dot{m}_j V_j}{0.5\rho U_\infty^2 S} \qquad 3$$

To achieve complete stall flutter suppression, C_μ should generally be large enough to ensure that the attached boundary layer is able to overcome an adverse pressure gradient within a given pitching amplitude range. This prevents separation, shear layer development, and its eventual roll-up into an LEV. The issue with this kind of blanket criteria is that real-world systems are restricted by the jet flow injection rate. This restriction means that simply making C_μ large may not necessarily be feasible in practical applications.

Alternative methods such as scheduled blowing may provide a route to addressing this problem as actuation is only enabled after reaching a control set-point or via scheduling. Kim and Jee. (2023) demonstrated that timed jet pulses can interact with the LEV to alleviate pitching moment overshoot. Most notably, scheduled multi-jet pulses throughout the pitching phase could suppress the magnitude of moment hysteresis. Matalanis et al. (2017) also demonstrated that multiple scheduled jet pulses can reduce the unsteady lift hysteresis in a pitching aerofoil undergoing deep dynamic stall. Chen et al. (2022) triggered steady jet blowing during an established LCO to suppress the instability. It should be clarified that this technique is fundamentally different from pre-emptive actuation preceding the instability. The primary difference being that constant blowing preconditions the boundary layer ahead of an instability while actuated blowing may initiate via feedback or scheduling. For this reason, we will refer to this type of control authority as ‘scheduled actuation’, ‘actuated blowing’, and similar variations throughout this work to detach from the notion of constant blowing. A schematic diagram differentiating between constant jet blowing, scheduled pulses, and scheduled jet actuation is provided in figure 7 for clarity. While all three methods demonstrated potential for unsteady aerodynamic load alleviation in flexible structures, the parameter space encompassing both constant and scheduled control authorities remains to be largely unexplored. In particular, the role of the orientation angle, β, in scheduled flow control methodologies is not wholly understood during dynamic scenarios. One potential reason for this is because varying β in an experimental setting can be quite costly due to fabrication constraints. In contrast, the momentum coefficient (eqn. 3) is much easier to adjust during parametric campaigns and is often contextualised as the most relevant control setting along with the jet location placement. The combination of these two parameters has a significant influence on the static boundary layer separation point when operating at constant blowing conditions. In general, constant jet blowing tends to yield favourable lift recovery potential at stalled static angle of attacks when operating between $0 \leq \frac{x}{c} \leq 0.3$. If the jet location is placed closer to the trailing-edge, the benefits of tangential blowing are marginal as it does not tend to greatly alter the static stall angle of attack (Yousefi and Saleh, 2014).

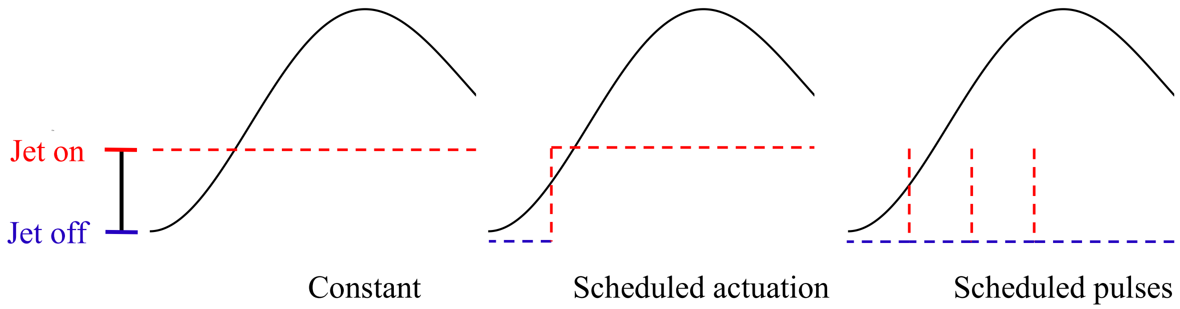

Figure 7. *Schematic comparison of constant (steady) blowing, scheduled pulses, and scheduled actuation control authorities applied within a subset of the aerofoil pitching cycle.*

The jet orientation angle, β, has demonstrated to be a sensitive parameter for obstructing the LEV formation in constant blowing jets. Towne and Buter (1994) documented the effects of varying the jet orientation angle between $\beta = 5^{\circ}$, $\beta = 10^{\circ}$, and $\beta = 20^{\circ}$ via numerical simulations. It was determined that $\beta = 5^{\circ}$ is the optimal choice for delaying the LEV formation when maintaining a constant C_{μ}. At higher orientation angles, the jet was actually counter productive to delaying the formation of an LEV. Despite this evidence, many other case studies have successfully reported stall flutter or dynamic stall suppression over a wide range orientation angles suggesting a range of useful flow control mechanisms. A non-exhaustive list of stall flutter and dynamic stall related work utilising constant blowing jets is given in table 1 along with their respective jet orientation angle range.

Authors	**Aerofoil**	C_{μ}	$\beta(°)$	**Jet Location**	**Type of Study**
Kim *et al*. (2019)	Onera OA209	0.06	22, 80	$0.1c$	N
Weaver, McAlister and Tso (2004)	Boeing-Vertol VR-7	0.16-0.66	'Tangential'	0.25c	E
Chen *et al*. (2022)	NACA 0012	0.007-0.315	45	0.1c	E
Müller-Vahl et al. (2015)	NACA 0018	0.003-0.05	20	0.05c,0.5c	E
Seidel, Fagley and McLaughlin, (2015)	NACA 0018	$8.3x10^{-9} - 8.3x10^{-5}$	-17.02	0.1c	N
Towne and Buter (1994)	NACA 0015	0.169	5, 10, 20	0c	N

Table 1. *Non-exhaustive list of steady jet blowing studies for stall flutter/dynamic stall control. 'N' and 'E' denote numerical and experimental type studies, respectively.*

In all of the case studies reported in table 1, at least one set of successful conditions was documented for suppressing or completely eliminating the LEV. Though, the exact relationship between the jet orientation angle and LEV dynamics is presently unclear due to the large parameter space associated with jet control authorities. This is because unsteady aerodynamic load alleviation is possible through several mechanisms like early LEV drifting, disruption, or roll-up prevention. These mechanisms may achieve similar end goals but through dramatically different pathways. As such, a thorough computational investigation into how β affects the dynamic stall process in resource efficient control authorities such as scheduled blowing is warranted.

Chapter 3

3.1 Finite Volume Method

For an incompressible, unsteady, and 3-dimensional flow, equations 4 and 5 represent the dimensionless governing equations for momentum and mass conservation when taken at an inertial and cartesian frame of reference where u_i, p, f_i, and Re are the i^{th} velocity component, modified pressure, volumetric force, and Reynolds number, respectively.

$$\frac{\partial u_i}{\partial t} \quad \frac{\partial u_i}{\partial x_j} u_j = -\frac{\partial p}{\partial x_i} \quad \frac{1}{Re}\frac{\partial^2 u_i}{\partial x_j\,\partial x_j} \quad f_i \tag{4}$$

$$\frac{\partial u_i}{\partial x_i} = 0 \tag{5}$$

In this work, equations 4 and 5 are non dimensionalised by using relevant characteristic length and velocity scales which are taken to be the aerofoil chord, c, and free stream speed, U_∞. The Reynolds number is then given by equation 6 where ρ and μ are the fluid density and dynamic viscosity, respectively.

$$Re = \frac{\rho U_\infty c}{\mu} \tag{6}$$

An approximate numerical solution to equations 4 and 5 can be obtained by utilising the finite volume method (FVM) as documented extensively by Ferziger and Peric (2002).

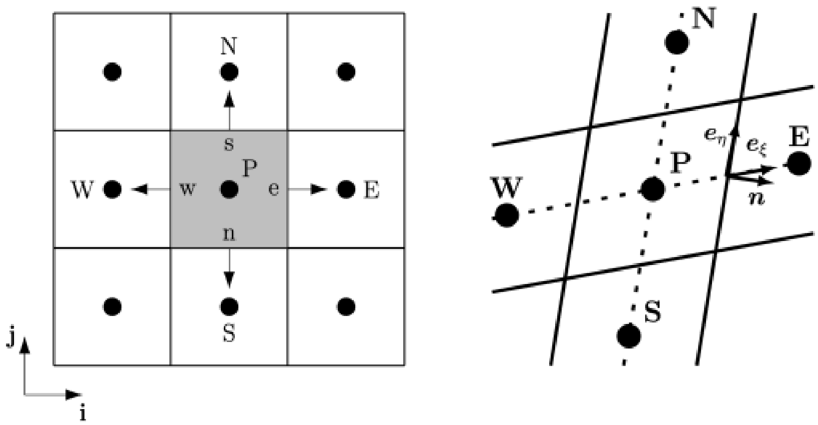

Figure 8. *2D finite volume method spatial convention stencil for cartesian (left) and skewed structured grid (right).*

The so-called 'weak' form of the Navier-Stokes equations can be obtained by integrating over an arbitrary control volume to yield equations 7 and 8, respectively. V and S represent the control volume and bounding surface of the control volume, respectively. n_i represents the i^{th} component of the outward normal vector of S as shown by figure 8 where North, South, East, and West compass directions are used as a common labelling convection.

$$\frac{\partial}{\partial t}\int_V u_i dV \quad \int_S u_i u_j n_j dS = -\int_V \frac{\partial p}{\partial x_i} dV \quad \int_S \tau_{ij} dS \quad \int_V f_i dV \tag{7}$$

$$\int_S u_i n_i dS = 0 \tag{8}$$

τ_{ij} represents the viscous stress tensor of the diffusive flux term and is given by equation 9 below.

$$\tau_{ij} = \frac{1}{Re}\left(\frac{\partial u_i}{\partial x_j} \quad \frac{\partial u_j}{\partial x_i}\right) \tag{9}$$

The convective and diffusive flux terms in equation 7 are the result of applying Gauss' divergence theorem where the surface integral of the vector field over an enclosed surface is equal to the volumetric integral of the divergence over the region enclosed by its surface. For a generic differentiable vector field, F_i, this application is represented by equation 10.

$$\int_V \frac{\partial F_i}{\partial x_i} dV = \int_S F_i n_i dS \tag{10}$$

A solution to equation 7 can be approximated numerically by spatial discretisation of a domain into many contiguous and non-overlapping control volumes (CV's) where the conservation equations are applied to each individual CV. This method is inherently conservative when the flux terms are equal between CV shared faces. Volumetric averages of the field variables u_i and p are stored at each CV centroid as per a collocated arrangement that simplifies both the programming and data storage requirements for complex geometries like an aerofoil section. A well-known limitation of this cell centroid collocation approach is the emergence of spurious pressure oscillations referred to as checkerboarding. This numerical instability is typically handled by using the Rhie and Chow interpolation method (Rhie and Chow, 1983) and will be discussed at a later point.

In this work, a 3D structured grid is utilised where the CV shape is cuboidal and consists of six bounding faces. A single integration point is fixed at the centre of each of the surfaces which simplifies the surface integration at each face. The total flux through the surface of a CV boundary can be computed by summing over the contributions at each of the six faces as represented by equation 11. Here, k is an index for the number of faces bounding the CV.

$$\int_S f dS = \sum_k \int_{S_k} f dS \tag{11}$$

f is regarded as any component of the flux vector that is normal to the CV face like the normal convective and diffusive flux terms present in equation 7. Note that for constant viscosity and an incompressible fluid, the diffusive flux term can be reduced to a simplified form given by equation 12.

$$\int_S \tau_{ij} n_j dS = \frac{1}{Re}\int_S \frac{\partial u_i}{\partial x_j} n_j dS \tag{12}$$

Surface integrals are evaluated using the second order accurate mid-point rule. Equation 11 can be approximated as the product of the integrand at the cell face centroid and the associated surface area. In a 2-dimensional cell, the right-hand side of equation 11 reads as a summation of four surface flux components through a CV as shown by equation 13. Here, e, w, n, and s refer to the faces of a 2D CV as per the direction component convention illustrated previously in figure 8.

$$\sum_k \int_{S_k} f dS \approx f_e S_e \quad f_w S_w \quad f_n S_n \quad f_s S_s \tag{13}$$

In order to compute this approximation though, the flux components at each face must be determined using the values stored at the neighbouring CV centroids (eqn. 14). For example, f_e is determined using a linear interpolation of stored values at points P and E, where the distances between the two nodes and the shared face are known beforehand.

$$f_e = f_E \gamma_e \quad f_P(1 - \gamma_e) \tag{14}$$

$$\gamma_e = \frac{x_e - x_P}{x_E - x_P} \tag{15}$$

Similar to the surface integral approximation used to compute the convective and diffusive flux terms, the midpoint rule can be extended to approximate volumetric integrals. The integral is estimated as the product of the integrand at the cell centre and the associated CV volume as shown by equation 16. Here, q represents an integrand to be evaluated at the integration point P. For constant source terms like gravitational acceleration for example, this integral is exact.

$$Q_P = \int_V q dV \approx q_P V_P \tag{16}$$

Utilising the above approximations for surface and volumetric integrals, equation 7 can be spatially discretised. The volumetric integral terms including the unsteady, pressure, and auxiliary forcing terms are simply computed using equation 16. The convective flux term can be computed using equation 11 assuming face interpolated values are known. For example, the x-component of the convective flux vector, F_e^c, can be approximated through the east face of the CV using equation 17.

$$F_e^c = \int_{S_e} u\boldsymbol{u} \cdot \boldsymbol{n} \, dS \approx u_e (\boldsymbol{u} \cdot \boldsymbol{n})_e S_e \tag{17}$$

Similarly, the x-component of the diffusive flux, F_e^D, through the east face of the CV can be approximated using equation 18.

$$F_e^D = \int_{S_e} \frac{1}{Re} \frac{\partial u}{\partial x_j} n_j dS \approx \frac{1}{Re} (\boldsymbol{\nabla} u \cdot \boldsymbol{n})_e S_e \tag{18}$$

Equation 18 requires that the gradient of u at the CV face is known beforehand. This can be obtained by first approximating the derivative at the CV centroid using equation 19.

$$\left(\frac{\partial u}{\partial x_i}\right)_P \approx \frac{\int_V \frac{\partial u}{\partial x_i} dV}{V_P} \tag{19}$$

Equation 20 is then the result of applying Gauss' theorem to the numerator of equation 19 for a 2D CV where $k = e, w, n, s$ are faces of the cell and $\boldsymbol{e_i}$ is a unit vector in the i^{th} direction.

$$\int_V \frac{\partial u}{\partial x_i} dV = \int_S u\boldsymbol{e_i} \cdot \boldsymbol{n}\, dS \approx \sum_k u_k S_k^i \tag{20}$$

Plugging this result back into equation 19 yields the final numerical approximation for velocity derivative at the cell centroid location, P.

$$\left(\frac{\partial u}{\partial x_i}\right)_P \approx \frac{\sum_k u_k S_k^i}{V_P} \tag{21}$$

The use of face interpolated values to compute this derivative can lead to oscillations in the flow field which can be corrected using the method proposed by Muzaferija (1994). In this formulation, a corrector is added which is the difference between the correct and approximated flux. This correction, applied to the diffusive flux on the east face of a CV is given by equation 22.

$$F_e^D = F_{e,\ implicit}^D \quad \left(F_{e,\ explicit}^D - F_{e,\ implicit}^D\right)^{old} \tag{22}$$

Here, the 'old' components are the value from the previous iteration or time step and explicit or implicit signifies the respective treatment of each term. For a cartesian grid, where the line connecting points P and E is orthogonal to the intersecting plane, the implicit diffusive flux term is simplified to the form of equation 23 where ξ is the component direction along the axis of this intersecting line.

$$F_{e,\ implicit}^D = \frac{1}{Re} S_e \left(\frac{\partial u}{\partial \xi}\right)_e \tag{23}$$

If the grid is non-orthogonal as shown in figure 8, equation 23 must include the difference between the gradient in $\boldsymbol{n}$ and $\boldsymbol{\xi}$ directions as contained in the 'old' term of equation 24. The first term on the right-hand side is treated implicitly where the second term is computed by interpolation of the cell centred gradients.

$$F_e^D = \frac{1}{Re} S_e \left(\frac{\partial u}{\partial \xi}\right) \quad \frac{1}{Re} S_e \left[\left(\frac{\partial u}{\partial n}\right)_e - \left(\frac{\partial u}{\partial \xi}\right)_e\right]^{old} \tag{24}$$

The computation of this corrected diffusive flux through the eastern face is finally given as equation 25 which maintains second order accuracy on non-orthogonal grids.

$$F_e^D = \frac{1}{Re} S_e \left(\frac{u_E - u_P}{L_{P,E}}\right) \quad \frac{1}{Re} S_e (\boldsymbol{\nabla} u)^{old}{}_e \cdot (\boldsymbol{n} - \boldsymbol{e}_\xi) \tag{25}$$

3.2 Temporal Discretisation

For an incompressible fluid, a numerical solution to the momentum equation is complicated by the lack of an independent equation of state to determine p. This limitation necessitates that the mass conservation equation be imposed as a constraint on the computed velocity field at each time step. This can be achieved by using a fractional step method as communicated by Chorin (1968) and later adapted by Kim and Moin (1985). Their method is based on a decomposition of the velocity field into solenoidal and irrotational components that involves two distinct steps. First, a prediction step computes the intermediate velocity, $\boldsymbol{u}^*$,field based on equation 26 where $\boldsymbol{u^n}, N, G$, D, and L are the solenoidal velocity field, non-linear, gradient, divergence, and Laplacian operators, respectively. φ^n is the projection variable at the current time step. Here, the implicit Crank-Nicolson scheme is used for the wall normal diffusive terms, and the explicit Adams-Bashforth scheme is employed for all the other terms.

$$\frac{\boldsymbol{u}^* - \boldsymbol{u}^n}{\Delta \boldsymbol{t}} = -N_l(\boldsymbol{u}^n, \boldsymbol{u}^{n-1}) \quad \frac{1}{Re} L(\boldsymbol{u}^*, \boldsymbol{u}^n) - G(\varphi^n) \tag{26}$$

The updated solenoidal velocity at $\boldsymbol{u}^{n+1}$ is then computed using the predicted velocity field from the previous step.

$$\frac{\boldsymbol{u^{n+1}} - \boldsymbol{u}^*}{\Delta t} = -G(\varphi^{n+1}) \tag{27}$$

φ^{n+1} can be computed by solving a Poisson equation that is derived by applying $D(\boldsymbol{u}^{n+1}) = 0$ as a constraint to the divergence of equation 27.

$$L\varphi^{n+1} = \frac{1}{\Delta t} D(\boldsymbol{u}^*) \tag{28}$$

The boundary condition applied here is given by equation 29 where $\boldsymbol{n}$ is the outward normal vector.

$$\frac{\partial \varphi^{n+1}}{\partial \boldsymbol{n}} = 0 \tag{29}$$

For conditions that allow for spanwise homogeneity and periodic boundary conditions can be applied, the 3D Poisson equation can be simplified to a series of 2D Helmholtz equations in wave number space by utilising the Discrete Fast Fourier Transform. In this work, the z-component is considered to be the spanwise direction of the domain. φ can be transformed in the wave number space by using the discrete anti-transform given by equation 30.

$$\varphi(x, y, z) = \sum_{l=0}^{N-1} \hat{\varphi}_l(x, y) \exp(ilz) \tag{30}$$

$\hat{\varphi}_l$ is the the l^{th} Fourier coefficient of φ and N is the number of modes to be specified. A set of decoupled Helmholtz equations can be formed for this Fourier system where k_l and $\hat{r}_l$ are the modified wave number and Fourier transform of the right side of equation 28, respectively.

$$\frac{\partial^2 \hat{\varphi}_l}{\partial x^2} \quad \frac{\partial^2 \hat{\varphi}_l}{\partial y^2} - k_l \hat{\varphi}_l = \hat{r}_l \tag{31}$$

Returning to the issue of pressure checkerboarding on collocated grids, the divergence term in equation 28 requires a centroid based interpolation to determine values at the CV faces. This necessitates that the Poisson equation be spatially discretised on a grid that is coarser than the grid for predicted variables $\boldsymbol{u}$ and p. This mismatch in discrete values gives rise to non-trivial solutions in the kernel of pressure operator which can affect the uniqueness of the computed solution, i.e. spurious pressure modes. To eliminate these modes, the mass fluxes obtained with the interpolated velocity are corrected by subtracting the difference between the pressure gradient and the interpolated gradient at the cell face location obtained at the previous time step. An example of this is given for the mass flux computed on the east face of a CV.

$$m_e = (\boldsymbol{u} \cdot \boldsymbol{n}) S_e - \Delta t S_e \left[(p_E - p_P) - \boldsymbol{\nabla} p \cdot e_\xi \right]^{old} \tag{32}$$

This step is performed prior to solving the Poisson equation and acts to smooth out the oscillations at each time step.

3.3 Large-Eddy Simulation

In this work we utilise LES which aims to resolve turbulent fluctuations larger than a defined filter width, Δ. Below this length, small scale contributions require modelling which is commonly fulfilled by a sub-grid scale eddy viscosity model. The unresolved stresses can be modelled by the inclusion of an isotropic scalar, ν_τ, that represents an apparent eddy viscosity. Sub-grid scale stresses can be modelled by equation 33 where $\overline{S_{ij}}$ is the resolved strain rate and δ_{ij} is the Kronecker delta.

$$\tau_{ij} - \frac{\delta_{ij}}{3} \tau_{kk} = -2\nu_\tau \overline{S_{ij}} \tag{33}$$

Conventionally, a filter width that determines the size of resolved eddies can be evaluated in proportion to the grid spacing, i.e. $\Delta \sim h$. This creates an inherent dependency between the grid and the modelling of unresolved scale eddies that complicates the notion of grid independence. This is because LES asymptotically approaches DNS results as grid spacing is decreased. Local grid refinement in areas of expected high shear can also lead to aliasing errors associated with the eddy viscosity which further complicates this turbulence modelling approach.

An alternative approach to traditional sub grid scale modelling can be implemented where the filter width is decoupled from grid spacing. Piomelli, Rouhi and Geurts (2015) developed an LES model, ILSA, where the filter with is determined in proportion to the integral length scale ($\Delta \sim L_{approx.}$). First, the filtered conservation of mass and momentum equations are given in traditional nomenclature by equations 34 and 35 where the overbar represents a filtering operation applied to the variable and $\tau_{ij} = \overline{u_i u_j} - \overline{u_i}\,\overline{u_j}$.

$$\frac{\partial \overline{u_i}}{\partial t} \quad \frac{\partial \overline{u_i}\,\overline{u_j}}{\partial x_j} = -\frac{\partial \bar{p}}{\partial x_i} \quad \frac{1}{Re} \frac{\partial^2 \overline{u_i}}{\partial x_j x_j} - \frac{\partial \tau_{ij}}{\partial x_j} \quad f_i \tag{34}$$

$$\frac{\partial \overline{u_i}}{\partial x_i} = 0 \tag{35}$$

Due to the decoupling of the filter width and grid spacing, Piomelli, Rouhi and Geurts (2015) rephrased the sub grid scale viscosity to a ‘sub filter’ scale viscosity but it retains an analogous role. Unresolved eddies are modelled using the form of equation 33 where ν_{SFS} is the sub filter scale eddy viscosity.

$$\tau_{ij} - \frac{\delta_{ij}}{3}\tau_{kk} = -2\nu_{SFS}\,\overline{S_{ij}} \tag{36}$$

ν_{SFS} is computed using equation 37 where C_k is a limiter constant that determines the turbulence resolution. A high value of C_k implies that a large range of turbulent eddies are modelled while a low value means most are resolved.

$$\nu_{SFS} = \left(C_k L_{approx}\right)^2 |\overline{S_{ij}}| \tag{37}$$

L_{approx} can be estimated from the resolved contribution of the turbulent kinetic energy, $k_{est} = \langle \frac{\overline{u_i'}\,\overline{u_j'}}{2} \rangle$. $\varepsilon_{tot} = \langle 2(\nu_{SFS} \quad \nu)\overline{S_{ij}}'\,\overline{S_{ij}}' \rangle$ is the total eddy dissipation rate which includes both modelled and resolved eddy contributions. This estimation is computed locally and instantaneously where the brackets, $\langle\cdot\rangle$, represent a spatial averaging operator applied in the homogenous spanwise direction.

$$L_{approx} = \frac{{k_{est}}^{3/2}}{\varepsilon_{tot}} \tag{38}$$

Substitution of equation 38 back into 37 yields an expression for the sub filter scale viscosity based on an approximate definition of the integral length scale.

$$\nu_{SFS} = C_k^2 \frac{\langle \frac{\overline{u_i'}\,\overline{u_j'}}{2} \rangle^3}{\langle 2(\nu \quad \nu_{SFS})\,\overline{S_{ij}}'\,\overline{S_{ij}}' \rangle^2} |\overline{S_{ij}}| \tag{39}$$

It can be seen that the ILSA model is entirely dependent on the assignment of C_k which can be determined either from a coarse grid error minimisation procedure or by simply assigning a value based on the available computational resources.

3.4 Numerical Implementation

The previously described methodologies used to numerically approximate a solution to the Navier-Stokes equations have been implemented into an in-house code, SUSA, that is written in Fortran 77. This code utilises the Open MPI message passing library for transferring and exchanging data between sections of a parallelised computational domain. SUSA has been built onto the City St. George’s, University of London supercomputer, Hyperion, using the gfortran compiler. This code has been extensively applied to a variety of LES and direct numerical simulation (DNS) case studies including a turbulent channel (Nicholas, 2022), canopy flows (Nicholas et al., 2022), static aerofoil at high angle of attack (Rosti, 2016), and aerofoil during ramp up motion (Rosti, 2016). The current work extends the validation of

SUSA for the case of a static NACA 63(3)418 aerofoil section over a range of incidence angles to serve as a pipeline for our stall flutter simulations.

A 2D, C-type computational domain was generated with a body conformal mesh using Pointwise. This mesh was translated to a third spatial component by a uniform extrusion in the aerofoil spanwise direction. Due to the computational limitations of high-fidelity parametric studies associated with both static and dynamic conditions, the spanwise length was restricted to $L_z = 0.1c$.

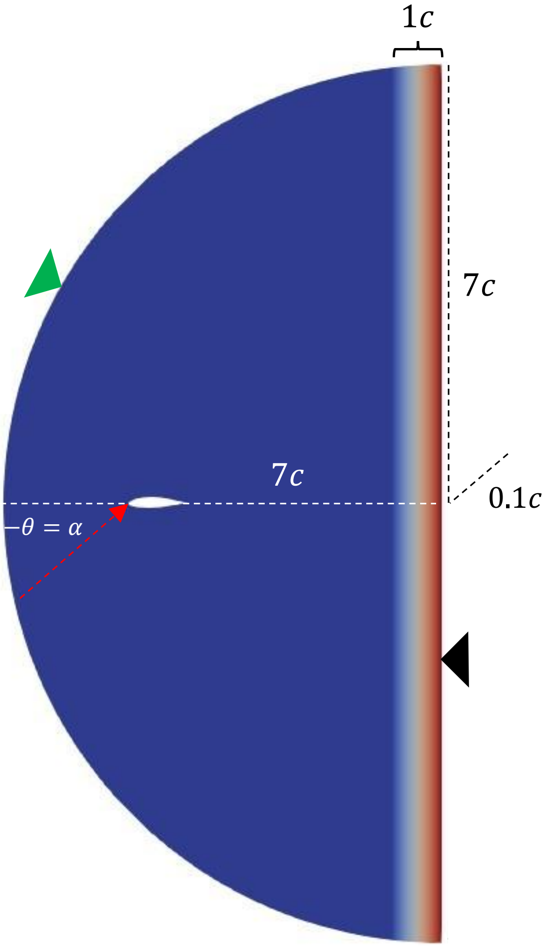

Figure 9. *C-grid schematic of computational domain with in-time updated inlet (green) and outlet (black) boundary conditions. Colour gradient denotes a sponge region applied along the domain outlet.*

The computational domain was segmented into structured x-z slabs where the y-component extends in the chord normal direction. The aerofoil leading-edge to inlet and outlet distances are $d_1 = 2c$ and $d_2 = 5c$ similar to the unsteady pitching setup of both Kern et al. (2024) and Negi et al. (2018) that utilised $d_1 = 3.5c$, $d_2 = 4c$, and $d_1 = 2c$, $d_2 = 4c$, respectively. Periodic boundary conditions are imposed in the z-direction to approximate the behaviour of an infinite span wing. The location of inlet and outlet boundaries are determined at each time step based on a local spanwise average of fluid velocity near the domain border. The direction of this velocity vector determines whether a boundary node is assigned as an inlet or outlet as illustrated by the green and black triangles in figure 9. Specifically, if the near wall averaged velocity vector points into the domain, a Dirichlet type condition is imposed onto the corresponding boundary. The value assigned to this region is determined by solving a companion potential equation via vortex panel method. Otherwise, the boundary is labelled as a convective outlet. Finally, a no penetration and no slip boundary condition is applied to the aerofoil surface for wall treatment.

In a time-dependent rotating reference frame, the conservation of momentum equation must be modified to include several fictitious forces. For an aerofoil section pitching within the $x - y$ plane, the incidence angle of attack is defined in the counter clockwise direction from the chord line as shown in figure 9. The conservation of momentum is adjusted to equation 40 where the Euler, Coriolis, and centrifugal forces are included in brackets as a right-hand side term and I^{θ} is an auxiliary matrix.

$$\frac{\partial u_i}{\partial t} \quad \frac{\partial u_i u_j}{\partial x_j} = \frac{-\partial p}{\partial x_i} \quad \frac{1}{Re}\frac{\partial^2 u_i}{\partial x_j \partial x_j} \quad (\ddot{\theta} I^{\theta}_{ij} x_j \quad 2\dot{\theta} I^{\theta}_{ij} u_j \quad \dot{\theta}^2 x_i) \tag{40}$$

$$I^{\theta} = \begin{bmatrix} 0 & 1 & 0 \\ -1 & 0 & 0 \\ 0 & 0 & 1 \end{bmatrix} \tag{41}$$

The inlet condition, to be updated in time, is also modified to equation 42 where v_i is the Dirichlet value assigned to the inlet boundary in an inertial frame and R^{θ} is the pitch degree of freedom rotation matrix.

$$u_i = R^{\theta}_{ij} v_j \quad \dot{\theta} I^{\theta}_{ij} \tag{42}$$

$$R^{\theta} = \begin{bmatrix} \cos(\theta) & \sin(\theta) & 0 \\ -\sin(\theta) & \cos(\theta) & 0 \\ 0 & 0 & 1 \end{bmatrix} \tag{43}$$

A more simplified approach to representing the pitch angle variation in a dynamic aerofoil simulation is by adjusting the velocity components assigned to the Dirichlet portion of the domain at each timestep. In this case, the fictitious forces are neglected, and the inlet condition simply takes the form of equation 44.

$$u_i = R^{\theta}_{ij} v_j \tag{44}$$

While this simplification does not reproduce the same conditions associated with wind tunnel experiments, it has been shown that for low values of angular velocity and acceleration, integral quantities like the lift and drag coefficient remain fairly consistent. Rosti (2016) demonstrated this similarity for the case study of an aerofoil undergoing ramp-up motion between $\alpha = 0^{\circ} - 20^{\circ}$ at a chord based reduced frequency of $K = 0.12$. They reported marginal differences between the computed lift and drag coefficients throughout this transient motion when compared to the case including inertial forces. The largest discrepancy appeared during the LEV growth phase which manifested as an approximately 10% underprediction of lift near the maximum dynamic stall angle. Overall, both cases demonstrated similar behaviour regarding aerodynamic hysteresis owing to the generation, advection, and shedding of a coherent vortex over the aerofoil. Due to the inherent similarity between aerofoil ramp-up motion and high angle attack oscillations, the current work utilises an inertial frame of reference with rotated inlet conditions to simplify the computational requirements of all stall flutter simulations.

Finally, a sponge region is constructed along the domain outlet boundary to help address stability issues for our dynamic case studies when large scale vortices attempt to penetrate a convective outlet. This sponge region takes the form of a linearly varying source term applied to the u velocity component given by equation 45.

$$\sigma = -\vartheta\left(\frac{x - x_{start}}{x_{end} - x_{start}}\right)(u(x) - u_{bulk}) \qquad 45$$

This region is applied between $x = 6c$ and $x = \ c$ as indicated by the contour gradient in figure 9. $\vartheta = 6.3$ is a user defined weight that scales the influence of this source term. u_{bulk} is utilized as the target velocity for this forcing function and updates in time based on the computed mass outflux.

3.5 Convergence and Validation Study

To assess the validity of this computational setup, a mesh independence study was first conducted. Five candidate grids ranging from 'coarse' to 'very fine' were assessed on their predictive capabilities of mean aerodynamic loads, C_L and C_D. All tests were conducted at a static angle of attack, α = 20°, and chord-based Reynolds number of $Re_c = 100{,}000$. The turbulence resolution factor is set at $C_k = 0.02$ for all work.

Grid	**M1**	**M2**	**M3**	**M4**	**M5**
Type	Coarse	Semi-coarse	Moderate	Fine	Very Fine
Total Cells (N)	9e+6	15e+6	30e+6	42e+6	80e+6
Spacing (x, y, z)	441, 284, 81	661, 284, 81	1,321, 284, 81	1,761, 300, 81	2,001, 500, 81
β_{max}	0.28	0.30	0.28	0.40	0.32
$\overline{x^+}$	45.39	35.00	15.71	14.22	13.55
$\overline{y^+}$	1.01	0.80	0.94	0.938	0.919

Table 2. *Grid independence study mesh characteristics ranging from coarse to very fine cell spacing. β_{max} refers to the maximum equiangular skewness angle.*

Simulations were conducted for a minimum of $t\frac{U_\infty}{c} = 20$ time units in order to sufficiently purge initial transients that might pollute mean statistics. This corresponds to approximately 6.7 flow times over the aerofoil. In some cases, the simulation time was extended as needed to meet a sufficient level of statistical convergence. Details pertaining to the mesh characteristics associated with this convergence study are presented in table 2. The time averaged aerodynamic lift and drag coefficients are presented in figure 10 for varying grid cell count where M5 is considered a baseline and is used to normalize cases M1-M4. It can be observed that the M2, M3, and M4 grids are largely converged for lift while only M3 and M4 are of sufficient quality to accurately predict drag. The M4 predicted lift and drag are within 1.1% and 3.4% of the M5 respective values. M1 was discarded from further analysis due to its massive deviation from M5 in both lift and drag predictions. The boundary layer development was also evaluated for mesh convergence using grids M2 through M5.

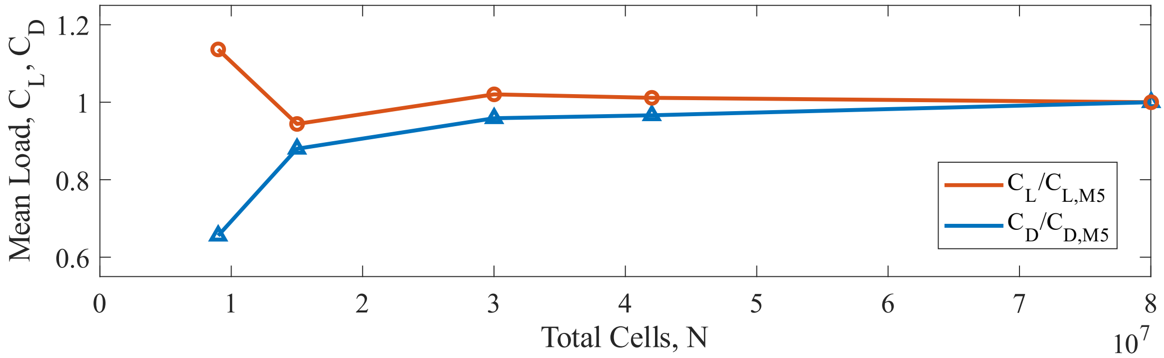

Figure 10. *Mesh convergence study of time-averaged aerodynamic loads C_L and C_D for static aerofoil section at $\alpha = 20^{\circ}$ and $Re_c = 100{,}000$. C_L and C_D are normalised by the respective M5 value.*

Discrete probes along the aerofoil surface were used to compare the u-component velocity profiles during highly stalled conditions. u is averaged in time and over the homogeneous spanwise direction, z, with values extracted along a linear path extending from the aerofoil suction side to $\frac{y}{c} = 1$. For each grid candidate, $\frac{u}{U_\infty}$ is plotted against the respective probe arclength and shifted horizontally for visual clarity (fig. 11). It can be seen that the grid cases M2-M5 are generally well aligned and exhibit canonical features such as boundary layer growth downstream, flow reversal, and a large separation zone due to a chordwise adverse pressure gradient. Though, the M2 predictions are degraded upstream as indicated by non-physical oscillations attributed to leading-edge grid coarsening. For all cases, errors amplify towards the trailing-edge but are maintained within 4% of the M5 predicted values at $\frac{s}{c} = 1$. Overall, M4 tends to be largely converged at these highly stalled conditions and was deemed as an acceptable balance between computational cost and accuracy for this work.

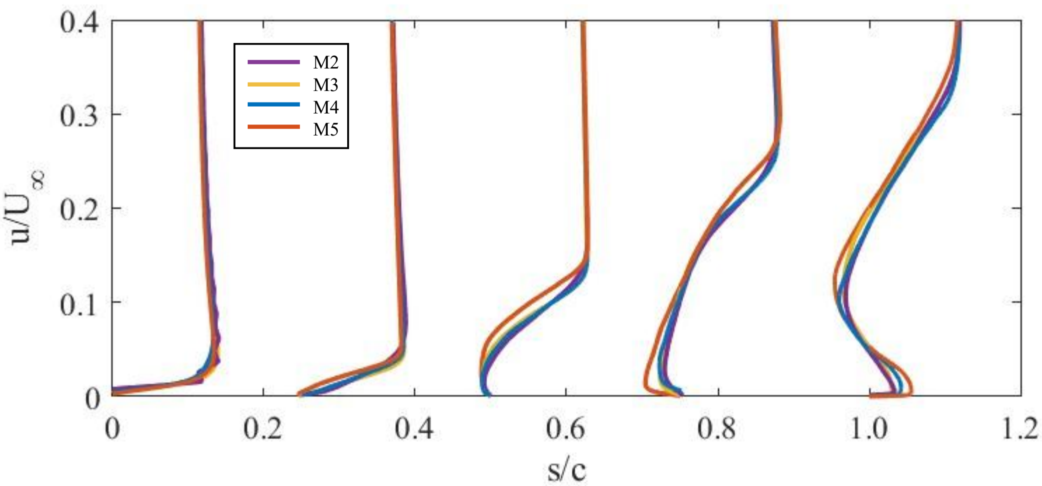

Figure 11. *Grid comparison of the time averaged u-component velocity profiles along the aerofoil chord. $\frac{s}{c}$ refers to the chord normalized arclength that is shifted along the x-axis for clarity.*

Next, an experimental campaign was conducted using the T2 subsonic wind tunnel facility at City St. George's, University of London to assess the predictive accuracy of our solver over a range of incidence angles. The T2 facility is a closed loop recirculating wind tunnel with a nominal operating range of $U_{\infty} = \quad -45\frac{m}{s}$. The wind tunnel has a dual window optical test section and is equipped with an Aerotech force balance for static load measurements.

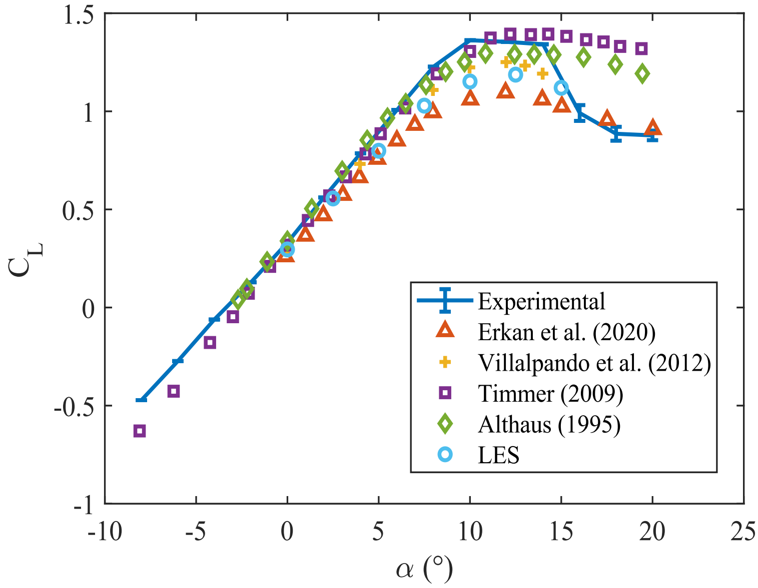

a)

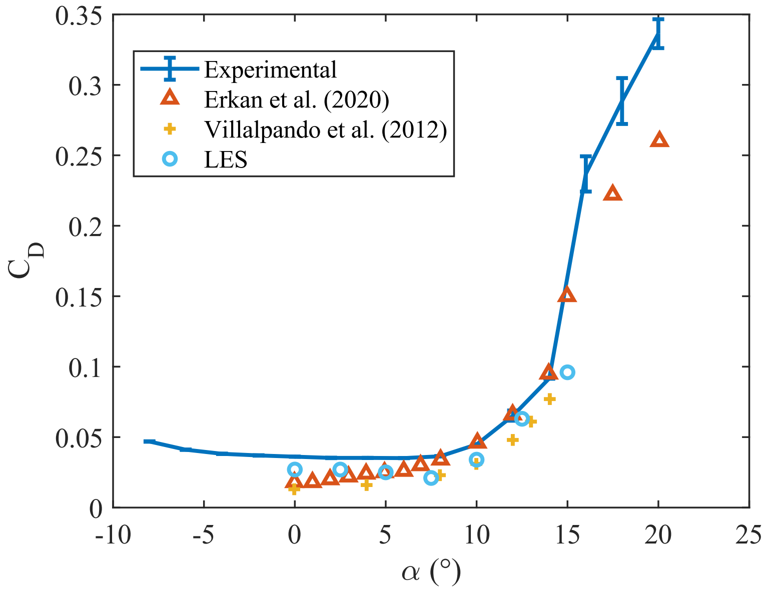

b)

Figure 12. *Static load comparison between experimental and LES measurements for a NACA 63(3)418 aerofoil. Externally sourced data: Orange triangle, NACA 63415,* $Re_c = 1e5$ *(Erkan et al., 2020). Yellow plus, NACA 63415,* $Re_c = 3e5$ *(Villalpando, Reggio and Ilinca, 2012). Purple square, NACA 63418,* $Re_c = 3e6$ *(Timmer, 2009). Green diamond, NACA 63418,* $Re_c = 3e6$ *(Althaus, 1995).*

The measurement section dimensions are $L_x = 1.78\ m, L_y = 0.81\ m,$ and $L_z = 1.12\ m$ which correspond to the streamwise, spanwise, and vertical directions, respectively. To emulate the 2D dominated flow conditions of our computational fluid dynamics (CFD) studies, a NACA 63(3)418 wing was fabricated to span approximately wall-to-wall in the T2 test section with small gaps ($\sim 1\ mm$) at the wing tips to allow for unobstructed pitch rotations. This wing was printed on a Bambu Lab X1 printer using a matte PLA filament in 7 distinct sections due to the printer size. These sections were aligned using male-female inserts (fig. 13) and mated with an epoxy filler to smooth the gaps at each of the sectional interfaces. The wingspan and chord length for the completed assembly are $c = 0.22\ m$ and $b = 1.118\ m$, respectively.

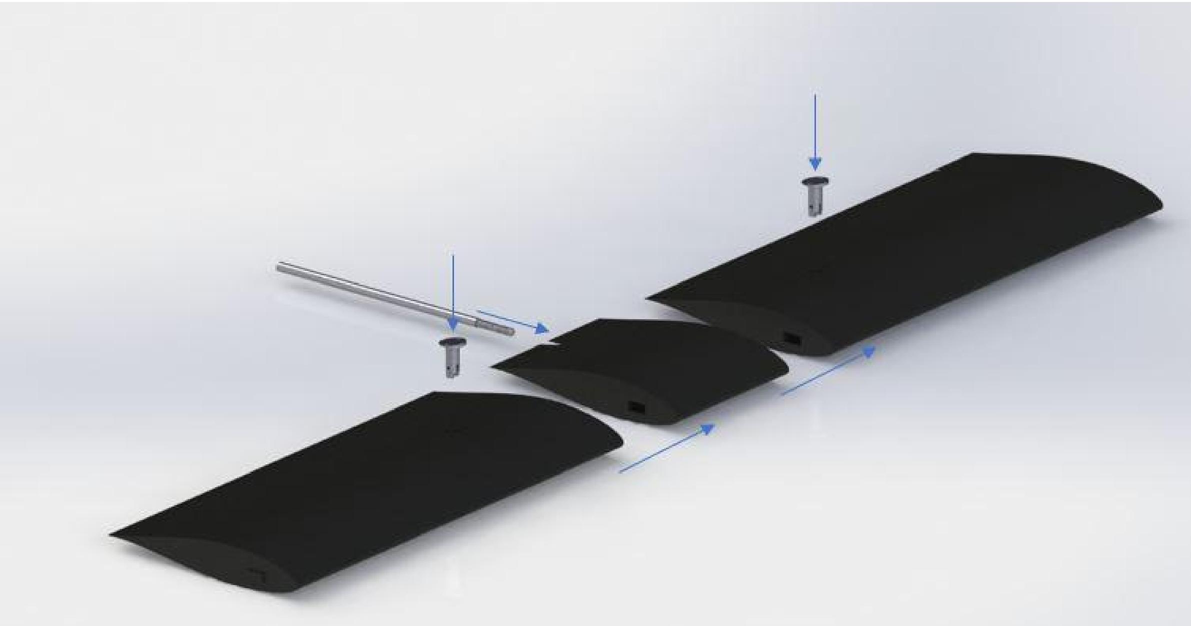

Figure 13. *3D CAD render of NACA 63(3)418 wing with horizontal and vertical sting mounts. Wing section spans wall-to-wall and rotates about the* $0.5c$ *location.*

Horizontal and vertical mounts were fabricated using aluminium and are used to transfer aerodynamic loads between the rigid wing, sting mounts, and T2 force balance. The vertical mounts were filed to sit flush with the suction surface of the wing and allow for a large pitch degree of freedom, $\alpha = \pm 35^{\circ}$. The horizontal sting fits directly into the wing chord line from the trailing-edge to help minimize bluff body interference and vibrations. This horizontal mount is attached to a lever arm that is used to rotate the wing about the $0.5c$ location.

Experimental measurements were conducted at an average wind tunnel speed of $\overline{U_\infty} = \ .9\frac{m}{s}$ which corresponds to a chord-based Reynolds number of $Re_c = 100{,}000$. Force balance measurements were taken at discrete angles of attack ranging from $\alpha = -8^{\circ} - 20^{\circ}$ at an increment of 2° and corrected for wall, blockage, and sting drag effects as per Allen and Vincenti (1944). The ensemble averaged results for C_L and C_D are shown in figure 12 with error bars to illustrate the measurement load variations sampled over a period of ten seconds each. Our LES based predictions tend to align quite well with the experimental measurements and external data sources at low to moderate angles of attack. Beyond $\alpha \geq 10^{\circ}$, disagreement between the various data sets tend to amplify indicating a familiar sensitivity to the aerofoil stall behaviour (Bak et al., 2022). Overall though, our LES setup is able to capture the general static load characteristics of the NACA 63(3)418 aerofoil.

3.6 Aeroelastic Modelling

The aeroelastic behaviour of a pitching aerofoil was modelled by a forced spring mass damper system where the aerodynamic pitching moment coefficient, C_M, is computed by integrating over pressure and viscous surface forces and summing their respective moment contributions about the $\frac{x}{c} = 0.5$ location. The non-dimensional form of this governing equation is given by equation 46 where $J = \frac{2I}{\rho c^4 b}, \mu = \frac{2m}{\rho U_\infty c^3 b}, k = \frac{2\kappa}{\rho U_\infty^2 c^2 b}$. $I, m,$ and κ are the dimensional moment of inertia, damping coefficient, and spring constant respectively. ρ, U_∞ and b are the fluid density, free stream speed, and aerofoil span. Equation 46 is integrated in time utilising an explicit Runge-Kutta scheme and with an adaptive Δt that is specified by the Courant–Friedrichs–Lewy condition (CFL) in our Navier-Stokes solver (eqn. 47). S represents the viscous CFL condition.

$$J\ddot{\theta}^* \quad \mu\dot{\theta}^* \quad k\theta^* = C_M(t) \tag{46}$$

$$\Delta t_{new} = \Delta t_{old}\left[\min\left(\frac{0.3}{CFL_{max}}, \frac{2}{S_{max}}\right)\right] \tag{47}$$

All simulations are conducted at a $Re_c = 100{,}000$ and varying mean incidence angles ranging from mild to deep stall conditions. In general, the effects of a moderate Reynolds number on dynamically stalled flows are less severe compared to other parameters such as the reduced frequency or aerofoil leading edge (Ohmi et al., 1991). Prior work has demonstrated that lift augmentation is postponed with increasing Reynolds number due to delayed LEV formation and detachment (Zhu et al., 2023). Though, varying the reduced frequency has a much more pronounced consequence in terms of energy extraction. Specifically, the Reynolds number and reduced frequency scaling of the coefficient of power, C_P, were shown to be logarithmic and exponential, respectively. As such, low to moderate Reynolds number effects may become attenuated when operating at sufficiently high reduced frequencies. The nondimensional model coefficients J , μ, and k, are varied within this work to adjust the reduced frequency parameter given by equation 48.

$$K = \sqrt{\frac{\kappa}{I}}\frac{c}{2U_\infty} \tag{48}$$

All case studies reported in this thesis start from initially static conditions where simulations are computed for a minimum of $t\frac{U_\infty}{c} = 20$ time units to ensure that initial transients are purged from the domain. After statistical stationarity is observed in the monitored aerodynamic loads, C_L and C_D, a small perturbation in angular velocity, $\dot{\theta}^* = 0.035$, is imposed to help trigger the stall flutter instability. The subsequent results corresponding to this numerical setup address a wide range of parametric conditions that are shown greatly influence the transient stall flutter dynamics. As such, our analyses of these results will be restricted to the first starting cycle in each parametric case study.

Chapter 4

4.1 Reduced Frequency Effects

One of the most common parameters to vary in the context of stall flutter or dynamic stall related research is the reduced frequency (eqn. 48). At high angles of attack, varying the reduced frequency can lead to non-monotonic behaviour in energy extraction as per a negative aerodynamic damping coefficient. The mechanisms responsible for this energy extraction are attributed to a complex dynamic stalling process that is still not wholly understood. Specifically, understanding how the LEV detachment mechanism is affected by K could yield potentially relevant insight into this knowledge gap.

In this section, one-shot pitching cycles are simulating starting from an initially static state at $\alpha = 10^{\circ}$ and $Re_c = 100{,}000$. The reduced frequency is also varied parametrically between $K = 0.15 - 0.21$ in increments of 0.01. These reduced frequency conditions exceed the 'quasi-steady' aeroelastic regime and are sufficient to observe complex transient dynamic stalling processes. An example of this for $K = 0.18$ is given by the velocity magnitude contours in figure 14 extending from 1a to 4c. Several canonical characteristics such as an initial shear layer growth, LEV roll up, chordwise advection, and detachment can be clearly observed within these intra-cycle snapshots.

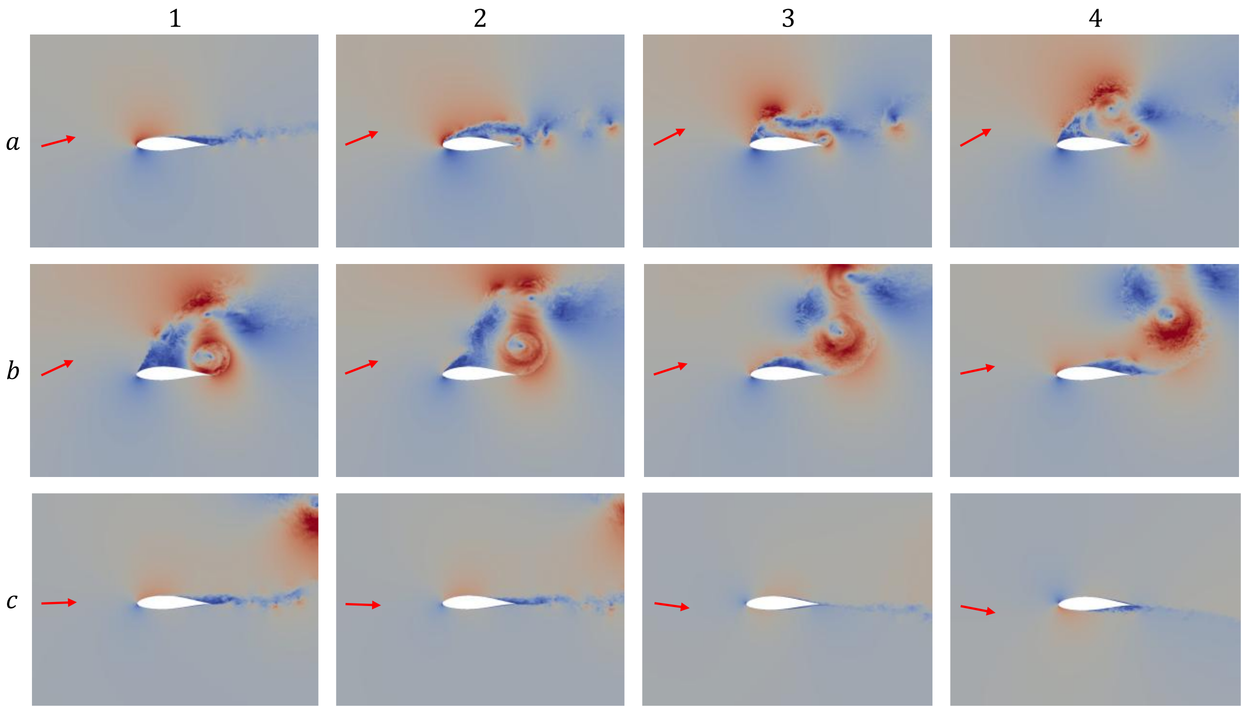

Figure 14. *Generalised dynamic stalling processes triggered by an initial angular velocity perturbation. Dynamics evolve from 1a to 4c. Contour is coloured by velocity magnitude which is scaled between* $\frac{||U||}{U_\infty} = 0 - 2$.

Aerodynamic loads, C_M and C_L were monitored throughout the one-shot pitching cycles for $K = 0.15 - 0.21$, respectively (fig. 15). Profiles are normalised between $\varphi = 0 - 2\pi$ radians for clarity and intra-cycle comparison. Time stamps for the case of $K = 0.18$ are placed in correspondence with labelled events in figure 14.

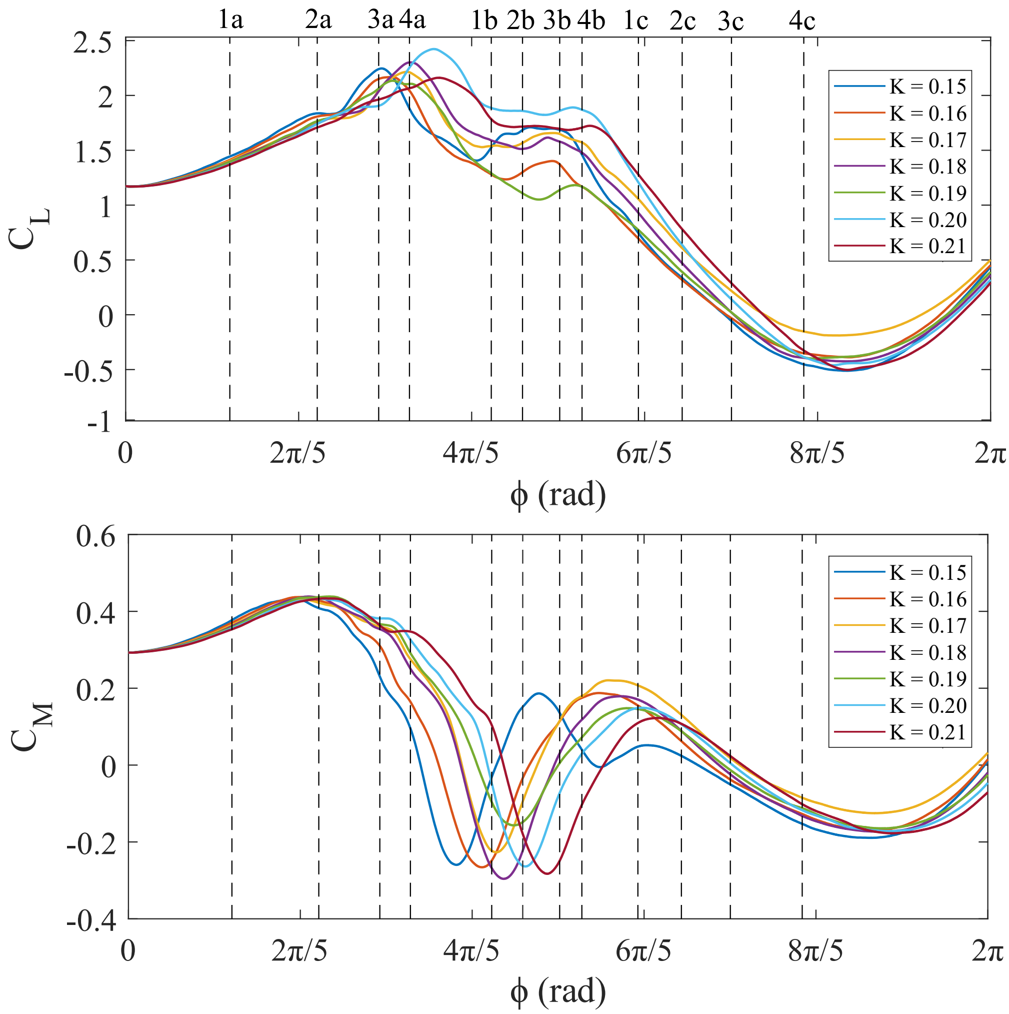

Figure 15. *Unsteady aerodynamic load profiles for* $K = 0.15 - 0.21$. *Black dashed lines correspond to the timestamps in figure 14.*

It is observed that the leading-edge shear layer rollup is first coincident with lift augmentation beyond static conditions. Moment stall is triggered early due to a chordwise shift in the surface pressure distribution that acts to restore a favourable pitch down moment. For all cases, this tends to occur at approximately 2a as per similarities in the LEV initial development. Beyond this timestamp, the variations in both C_M and C_L traces amplify indicating a strong parametric sensitivity within the LEV maturation stage (3a). At 4a, the LEV corresponding to $K = 0.18$ reaches its maximum size/strength granting a peak lift coefficient of $C_{L_{max}} = 2.3$. Further LEV drifting is accompanied by a dramatic loss of lift conventionally termed as 'deep dynamic stall' or 'dynamic lift stall'. Post LEV severance, flow reattachment begins along the suction side starting from the leading-edge to establish a pitch-up moment. Between these fluid dynamic processes though, qualitative dissimilarities in how the LEV detachment actuates and sheds from the pitching aerofoil are present. In particular, a topological bifurcation in the LEV detachment process occurs between $K = 0.19$ and $K = 0.20$ that could explain, in part, the variations in unsteady aerodynamic loading between starting cycles. Figure 16 illustrates two observed detachment mechanisms where line integral convolution (LIC) is utilised to highlight the interactions between the LEV and trailing edge. We expect that this topological change in the LEV lifecycle plays an incomplete but critical role in explaining the highly nonlinear dependency of K on stall flutter starting cycles.

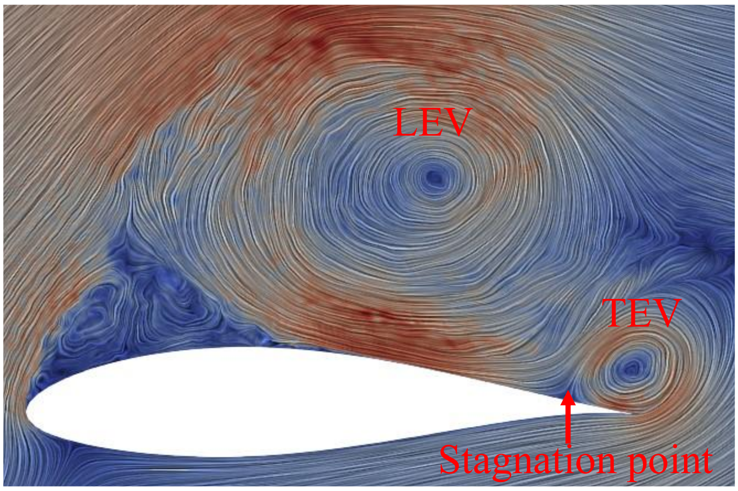

a)

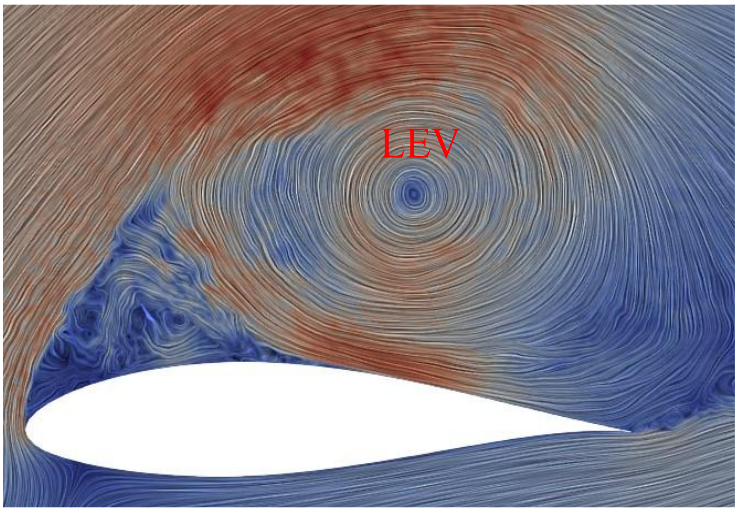

b)

Figure 16. *Velocity magnitude contour of a) invasive LEV-TEV interaction and b) uninhibited LEV growth. LIC is overlayed for qualitative identification of vortex structures.*

At reduced frequencies, $K \leq 0.19$, the LEV grows and moves downstream until an impingement interaction occurs with a TEV. The migration of a strong TEV onto the aerofoil suction side acts to deflect the LEV away from the lifting body as demonstrated experimentally by Feszty, Gillies and Vezza (2004). This interaction occurs at a chordwise location, $\frac{x}{c} < 1$. Conversely, for cases $K = 0.20$ and $K = 0.21$, early LEV drifting is not observed. Instead, the LEV detachment process appears to be similar to a 'bluff body' mechanism as described earlier in this thesis. In this case, detachment initiates when the LEV rear stagnation point reaches $\frac{x}{c} = 1$.

In both flow scenarios, the LEV deflection point remains to be relatively consistent despite variations in the detachment mechanism. This is shown by monitoring the vortex core trajectories throughout the growth and shedding stages. Vortex cores were determined by spatial averaging over point clouds identified through localised Q-criterion thresholding. These positions were then confirmed qualitatively by LIC. Note that for timesteps where a vortex core is not readily identifiable, its position is assumed to originate from the leading-edge, $\frac{x}{c}, \frac{y}{c} = (0,0)$.

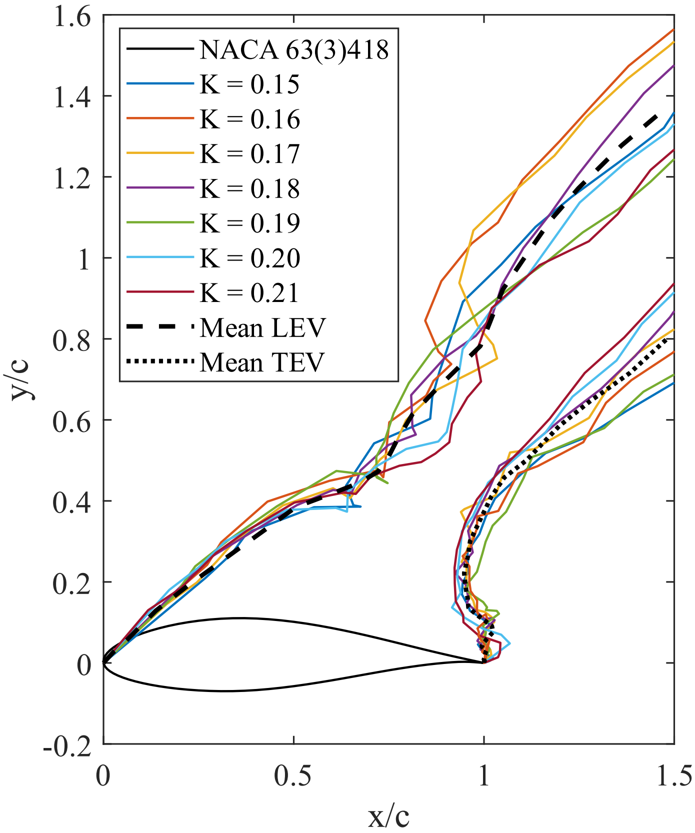

Figure 17. *LEV and TEV core trajectories computed for each parametric case,* $K = 0.15 - 0.21$. *Cores were identified through Q-criterion thresholding and confirmed via LIC.*

For each one-shot cycle, the LEV path tends to experience an approximately linear trajectory up until a deflection point that is consistent with behavioural tendencies observed in previous work (Lee et al., 2022). Beyond this, there are large variations in the path lines confirming a strong sensitivity to the LEV detachment process. An approximate detachment location was identified by monitoring inflection points along an ensemble averaged trace of the LEV trajectories. Two distinct points were then isolated corresponding to the LEV attachment and detachment regimes, respectively (fig. 18). Between these two points, a brief transient period is observed which coincides with both LEV drifting and a sign change in the slope of the time-resolved lift coefficient (see figure 15 at 4a). Here, the forward changepoint identified at $\frac{x}{c} = 0.63$, is of particular importance as this is considered to be when the LEV detachment mechanism first actuates.

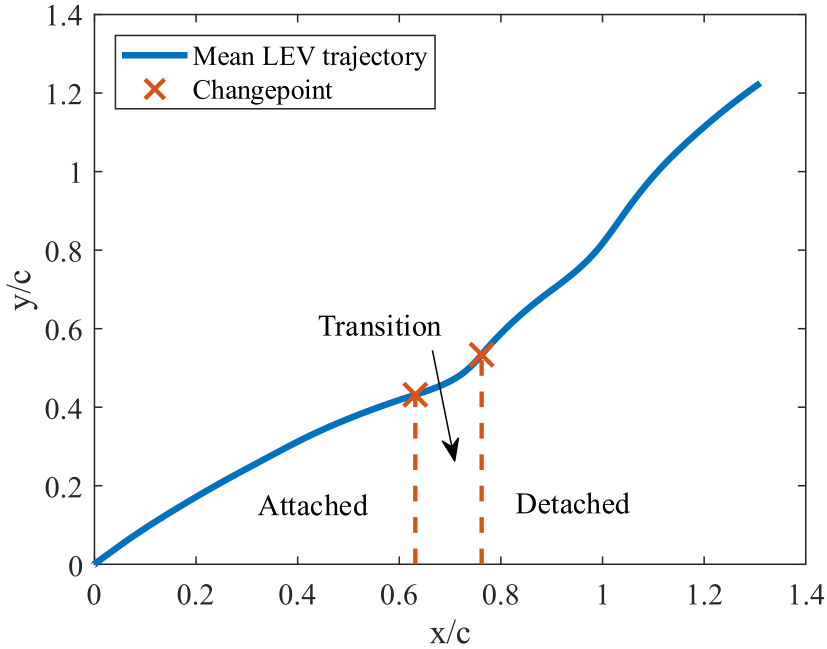

Figure 18. *Ensemble averaged LEV core trajectory. Changepoints were identified by computing localised inflection points.*

4.2 Flow Field Topology

Two LEV detachment mechanisms are observed within the current work. For now we will refer to the bluff body type mechanism as ‘scenario a)’ and the TEV interaction as ‘scenario b)’. According to Foss (2004), these topological scenarios are classified by the Euler characteristic, where the value of x_{surf} is constant for a given number of holes and handles within a domain. Handles are regarded as obstacles that are surrounded by a continuous fluid and the inlet-outlet nodes are holes. x_{surf} is defined by equation 49, where the constant, 2, represents the Poincare index of a collapsed sphere. In this work, $handles = 1$ and $holes = 2$ to represent the aerofoil body and inlet/outlet pathways, respectively. We refer the readers to Perry and Fairlie (1975) for a more explanatory source on the application of critical points classification to flow field patterns.

$$x_{surf} = 2 - 2\sum handles - \sum holes \qquad 49$$

According to Hunt et al. (1978), $x_{surf} = -2$ for the case of a 2D lifting surface with two inlet and outlet holes. As such, equation 50 must be satisfied in our topological descriptions to be physically realisable. Here, N and N' refer to full nodes and half nodes. S and S' refer to saddles and half saddles. Note that full nodes are labelled by $\pm\Gamma_i$ to illustrate clockwise or anticlockwise circulatory contributions.

$$x_{surf} = -2 = 2\sum N \quad \sum N' - 2\sum S - \sum S' = -2 \qquad 50$$

Scenario a) is similar to the benign detachment route introduced previously as it requires the merging of two downstream half-saddle nodes. For reduced frequencies, $K = 0.20$ and $K =$

0.21, a TEV is initially forced off the aerofoil trailing due to the LEV. A topological representation of this process is given in figure 19 where $S_5{}'$ merges with $S_6{}'$ to become a full saddle node, S_3. At this point, the TEV is separated from the aerofoil surface and counter rotating fluid becomes entrained between the suction side and LEV. Eventually, the counter rotating fluid rolls up into a secondary TEV as to conserve net circulation.

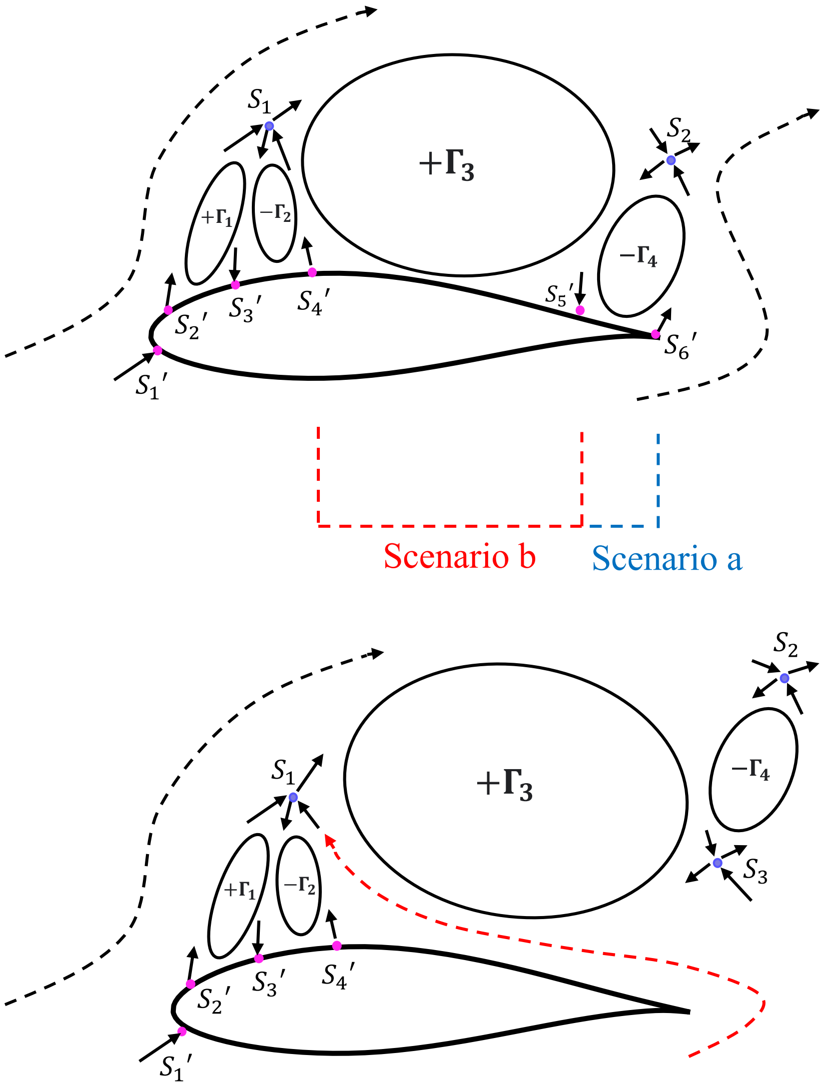

Figure 19. *a) Initial topological state prior to LEV detachment. b) 'bluff body' detachment mechanism initiating as $S_5{}'$ merges with $S_6{}'$.*

Indeed, this secondary structure contributes to LEV drifting, dynamic lift stall, and complete severance but is an inherent consequence of $S_5{}'$ and $S_6{}'$ first merging. Note that both pre and post detachment stages represented in figure 19 have an Euler characteristic, $x_{surf} = -2$. For the remaining parametric cases, Scenario b) is observed (fig. 20). We regard this scenario as an invasive detachment mechanism because the TEV first acts to inhibit the downstream advection of the LEV. Complete LEV severance then occurs due to the path merging of half saddle nodes, $S_4{}'$ and $S_5{}'$, to become a full saddle, S_3. Prior to this separation though, an intermittent 'squeezing' process between the TEV and upstream secondary structures acts to push the LEV away from the aerofoil. Again, the Euler characteristic for this scenario equates to, $x_{surf} = -2$.

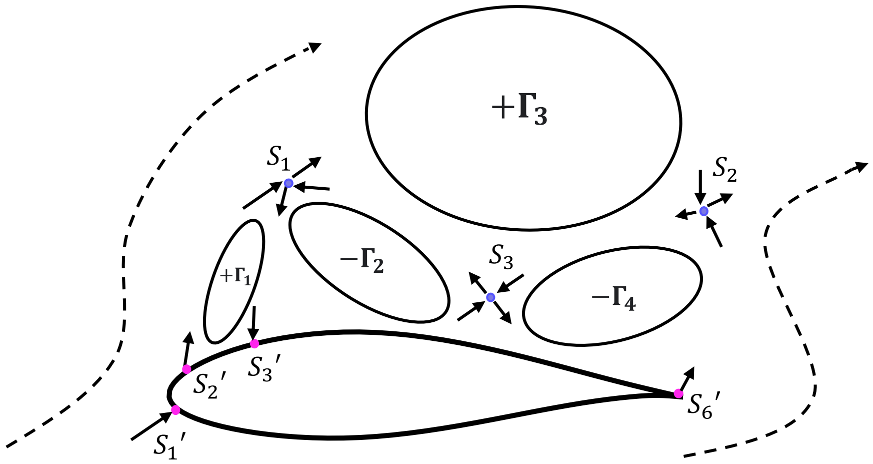

Figure 20. *Invasive LEV detachment mechanism due to a TEV. $S_4{}'$ merges with $S_5{}'$ upstream to create a full saddle node.*

In both topological scenarios, dynamic lift stall occurs when the proposed detachment mechanism is first actuated. That is, either when the LEV passes over the trailing edge (scenario a) or when the 'squeezing' interaction occurs between the LEV and upstream secondary structures (scenario b).

The proposed LEV-TEV interactions represented by these two detachment mechanisms can be verified by monitoring surface fluctuations throughout the dynamic stalling process. First, a heat map of the near-wall ($\frac{y}{c} = 0.01$) surface velocity fluctuations is shown over a subset of the pitching cycle in $K = 0.21$ (fig. 21). $S_4{}'$ and $S_5{}'$ half saddle nodes are also monitored along the aerofoil surface represented by the red and white dashed lines, respectively. As the aerofoil is pitching upward, a patch of induced surface velocity can be observed. This is representative of the LEV formation/growth and is confirmed by the $S_4{}'$ trace bounding the high velocity contour patch. Unique to scenario a) though, the $S_5{}'$ trajectory annihilates at its intersection with the LEV changepoint (black line) or drifting point. This behaviour suggests that the LEV growth rate monotonically increases until $S_5{}'$ reaches the aerofoil trailing edge and the 'bluff body' detachment mechanism is actuated. In other words, the characteristic length scale associated with this particular detachment mechanism is the aerofoil chord. Finally, a secondary TEV structure forms after this changepoint whose forward stagnation point is plotted in pink to distinguish from $S_5{}'$. Again, this secondary structure aids in both deep dynamic stall and complete LEV severance but is a direct consequence of topological scenario a) necessarily being fulfilled. In scenario b), the changepoint in figure 21 is coincident with induced surface velocity about the trailing edge. This represents a TEV and acts to squeeze $S_4{}'$ and $S_5{}'$ half saddle nodes. A pink dashed path line is also plotted here to differentiate between secondary structures and $S_5{}'$. In both topological scenarios, two trajectory paths eventually merge for complete fluid severance from the lifting body.

A distinction between these proposed detachment scenarios is the trailing edge interaction that occurs when LEV drifting and dynamic lift stall are first encountered. In particular, the spatio-temporal location of $S_5{}'$ at the changepoint. For scenario b) the $S_5{}'$ half-saddle node sits between two contour peaks which implicates an invasive interaction between the TEV and LEV. In contrast, scenario a) shows that $S_5{}'$ is unbounded and allowed to push beyond the trailing edge. It is clear from these contour maps that an LEV trajectory shift is possible through two distinct scenarios. The variation in $S_5{}'$ trajectory paths grant an understanding of how the LEV detachment is first triggered when juxtaposed with the changepoint timestamp. While subtle differences exist between each parametric case, a clear flow topology bifurcation is observed when varying the reduced frequency.

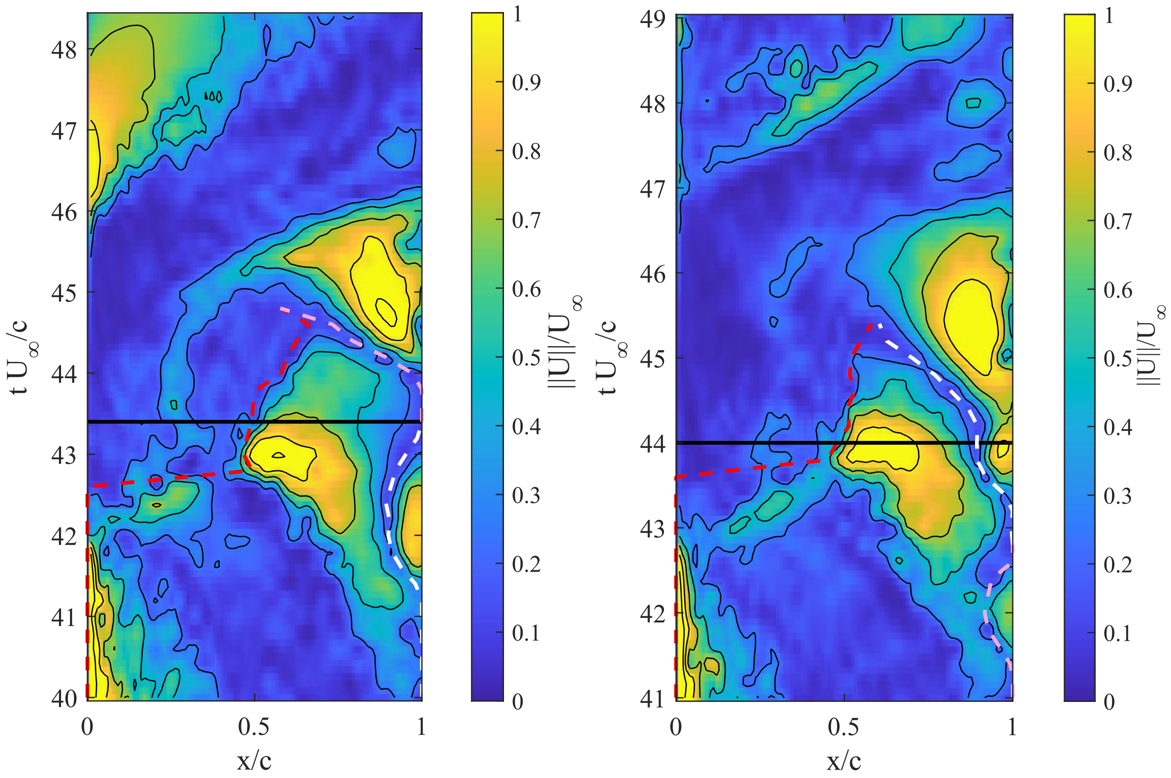

a) b)

Figure 21. *Suction side space-time velocity magnitude contours for comparing two LEV detachment mechanisms. Scenario a) (left) corresponds to* $K = 0.21$. *Scenario b) (right) corresponds to* $K = 0.15$. *Red and white dashed lines represent* $S_4{}'$ *and* $S_5{}'$ *Pink dashed line indicates a secondary structure.*

The surface pressure distributions for each one-shot cycle are computed at the LEV changepoint time to further understand this proposed bifurcation. Figure 22 illustrates the pressure coefficient distribution, C_p, over the aerofoil suction side. Parametric cases, $K = 0.15 - 0.21$ are shifted vertically for clarity. In all cases, a suction peak is observed at approximately $\frac{x}{c} \approx 0.6$. This is representative of a strong LEV that is still attached to the lifting body. A second pressure peak can be observed between $K = 0.15$ and $K = 0.19$ near the trailing edge which is caused by the TEV. Between $K = 0.19$ and $K = 0.20$ though, a significant change occurs about the trailing edge that we attribute to the proposed topological bifurcation between scenarios a) and b). At $K = 0.21$ a small relative suction peak is observed about the trailing edge. Though, this TEV is not strong enough to impede the LEV motion and scenario b) is still the dominant detachment mechanism. In general, scenario a) is observed when the suction peak ratio induced by a vortex is close to or greater than a given threshold.

That is, when $\frac{C_{p_{LEV}}}{C_{p_{TEV}}}$ is approximately 1, the TEV can be considered invasive. If $\frac{C_{p_{LEV}}}{C_{p_{TEV}}}$ is much greater than 1, scenario b) tends to actuate as the LEV is strong enough to push beyond the aerofoil trailing edge.

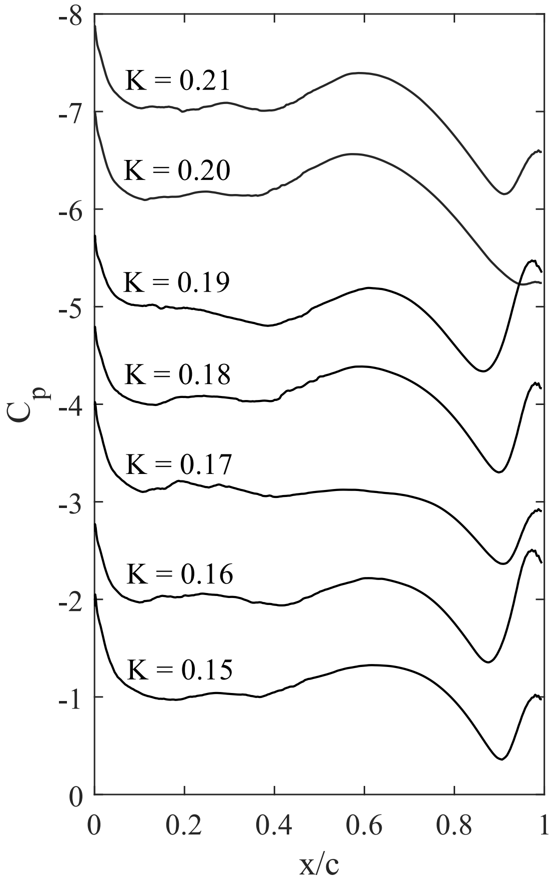

Figure 22. *Pressure coefficient distribution along aerofoil suction side for cases* $K = 0.15 - 0.21$. *Profiles are shifted vertically in increments of* $C_p = -1$ *starting from* $K = 0.15$.

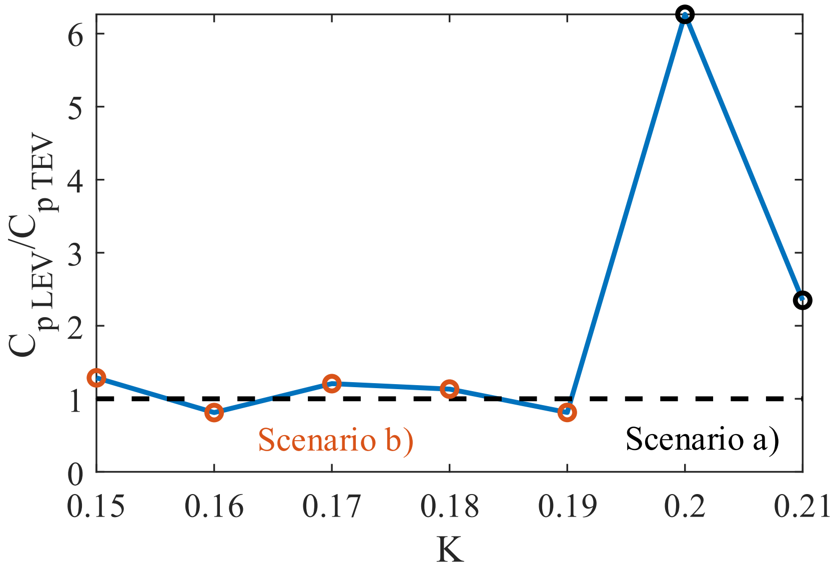

Figure 23. *Pressure coefficient peak ratios corresponding to figure 22. Localised segmentation of C_p occurs at approximately $\frac{x}{c} \approx 0.9$ for all parametric cases.*

This is shown in figure 23 where the induced suction peak ratios were computed based on a localised segmentation of the previously shown C_p data. This segmentation occurs at approximately $\frac{x}{c} \approx 0.9$ for all cases. For parametric cases $K \leq 0.19$, the pressure coefficient ratio tends to be approximately one indicating the LEV and TEV are of a comparable strength/size. Again, this tendency inhibits the LEV motion and triggers scenario b). For $K \geq 0.20$, this ratio is much greater than one due to the disparity in LEV and TEV strength/size. Thus, the LEV can push beyond the aerofoil trailing edge as per scenario a).

Chapter 5

5.1 Interference at High Incidence Angles

When operating at high incidence angles, periodically shed vortices can strongly interact with the dynamic stall process during aeroelastic pitching or plunging motions. It has been shown that this interaction can exhibit a wide range of constructive or destructive interference based on the vortex shedding phase angle. During aeroelastic transients like stall flutter starting cycles, this interference may play an important role in triggering subcriticality when the LEV-vortex shedding interaction is sufficiently constructive. Conversely, if this interference is overly destructive then aerodynamic damping may be dissipative as per a reduction in the net pitching moment hysteresis. Though, details pertaining to how this interaction explicitly affects the LEV development are currently lacking within the literature. Only the indirect consequences of this interaction have been reported by measuring the time resolved aerodynamic loads. Indeed, this quantification provides a measure of how the dynamic stall processes can change due to vortex shedding interactions but does not elucidate the fluid mechanisms responsible for this variability. To bridge this gap, we explore how periodic vortex shedding can affect the LEV developmental progression and its relationship to unsteady aerodynamic loading in transient starting cycles. We will explore how the status of the LEV structure correlates to unsteady aerodynamic loading using a combination of indirect and direct measurements.

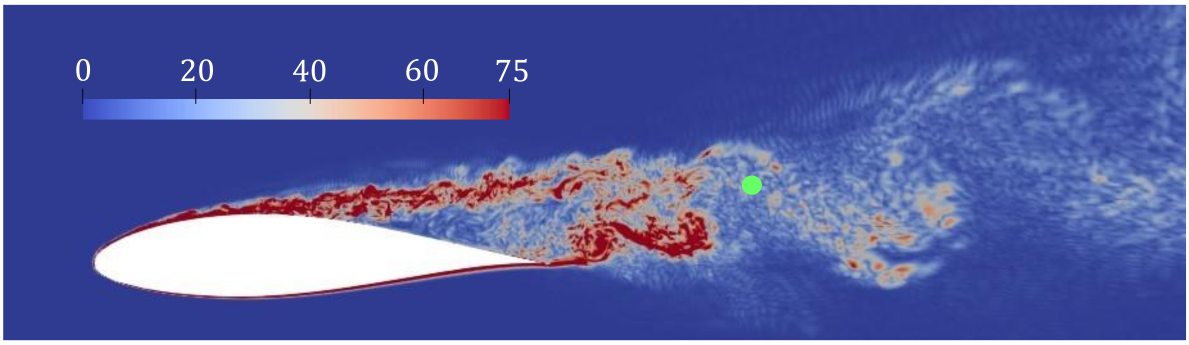

***Figure 24**. Kármán vortex shedding for NACA 63(3)418 aerofoil at $\alpha = 15^{\circ}$. Contour is coloured by vorticity magnitude, $\frac{||\omega||c}{U_\infty}$. Green dot represents a field probe for time-resolved measurements of $p, u, v, w,$ and ω_z.*

For this investigation, all simulations are conducted at Rec = 100,000 and a mean angle of attack of α = 15°. The nondimensional model coefficients are set as J = 0.0765, μ = 0.01, and $k = 0.0490$, which corresponds to a semi-chord based reduced frequency of K = 0.4. Starting from an initially static state, a small perturbation in angular velocity, θ^* = 0.035, is imposed to help excite the stall flutter instability. The timing of this perturbation varies between eight different cases based on the Kármán vortex shedding phase angle, φ. To determine these trigger times, time-resolved data was first obtained by setting a point probe within the shedding wake at a downstream location (fig. 24). Time-resolved field measurements were taken for a minimum of $t\frac{U_\infty}{c} = 20$ time units beyond statistical stationarity to ensure that multiple shedding events were captured. These field variables were then spatially averaged over the homogeneous spanwise direction.

The dominant shedding frequency was obtained by utilizing the discrete Fourier transform to compute the power spectral density (PSD) of two signals, p' and v', as shown in figure 25. Prime here denotes the fluctuating component of the respective signal. Both signals show strong peaks at a Strouhal frequency of St = 1.44 indicating a dominant mode of the vortex shedding instability. The Strouhal number was computed using equation 51 where f is the peak shedding frequency in Hertz. See section B.2 for a supplementary discussion of how this shedding frequency definition compares with literature sources.

$$St = \frac{fc}{U_\infty} \quad (51)$$

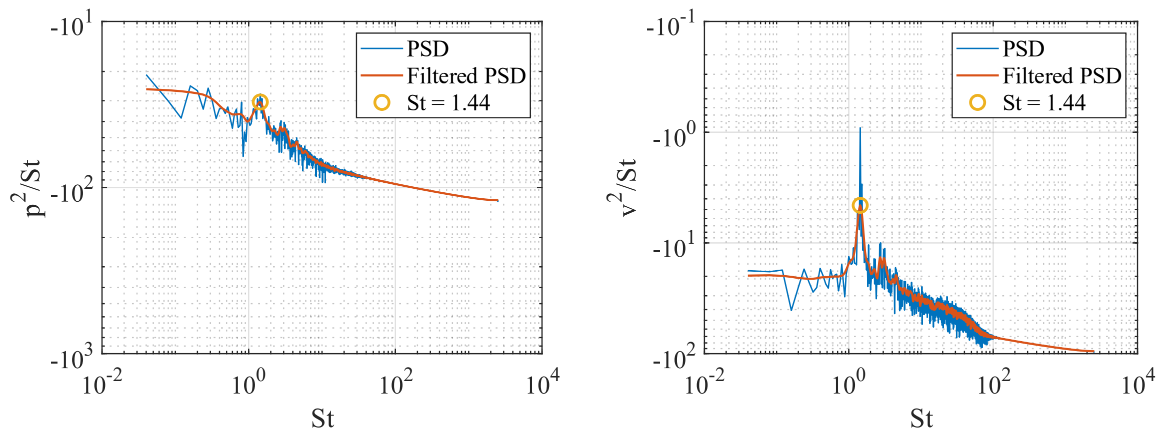

a) b)

Figure 25. *a) Pressure PSD with smoothing. b) v-component velocity PSD with smoothing. Yellow circle indicates dominant vortex shedding frequency. Probe measurements were taken within the wake shedding region of the flow field.*

The shedding cycle, modelled as a pure harmonic wave, was then utilized to determine eight different starting times that vary between φ = 0 ° and φ = 315° in increments of 45°. These conditions allow for approximately T = 2.5 shedding periods to pass over during the initial ramp-up portion of the stall flutter instability. While higher order harmonics are evidently present, these conditions are sufficient to observe strong transient interactions over the first starting cycle.

The integral effects of these initial conditions are demonstrated by the unsteady aerodynamic pitching moment, C_M, and lift coefficient, C_L, shown in figure 26. Note that each pitching angle trace and corresponding unsteady load traces are shifted along the time axis relative to φ = 0 ° for alignment purposes. It can be plainly observed that the time-resolved aerodynamic loads experience similar augmentation throughout the pitch-up portion of these starting cycles. In contrast, the pitch-down portion exhibits large aerodynamic load variations that greatly alter the pitching dynamics.

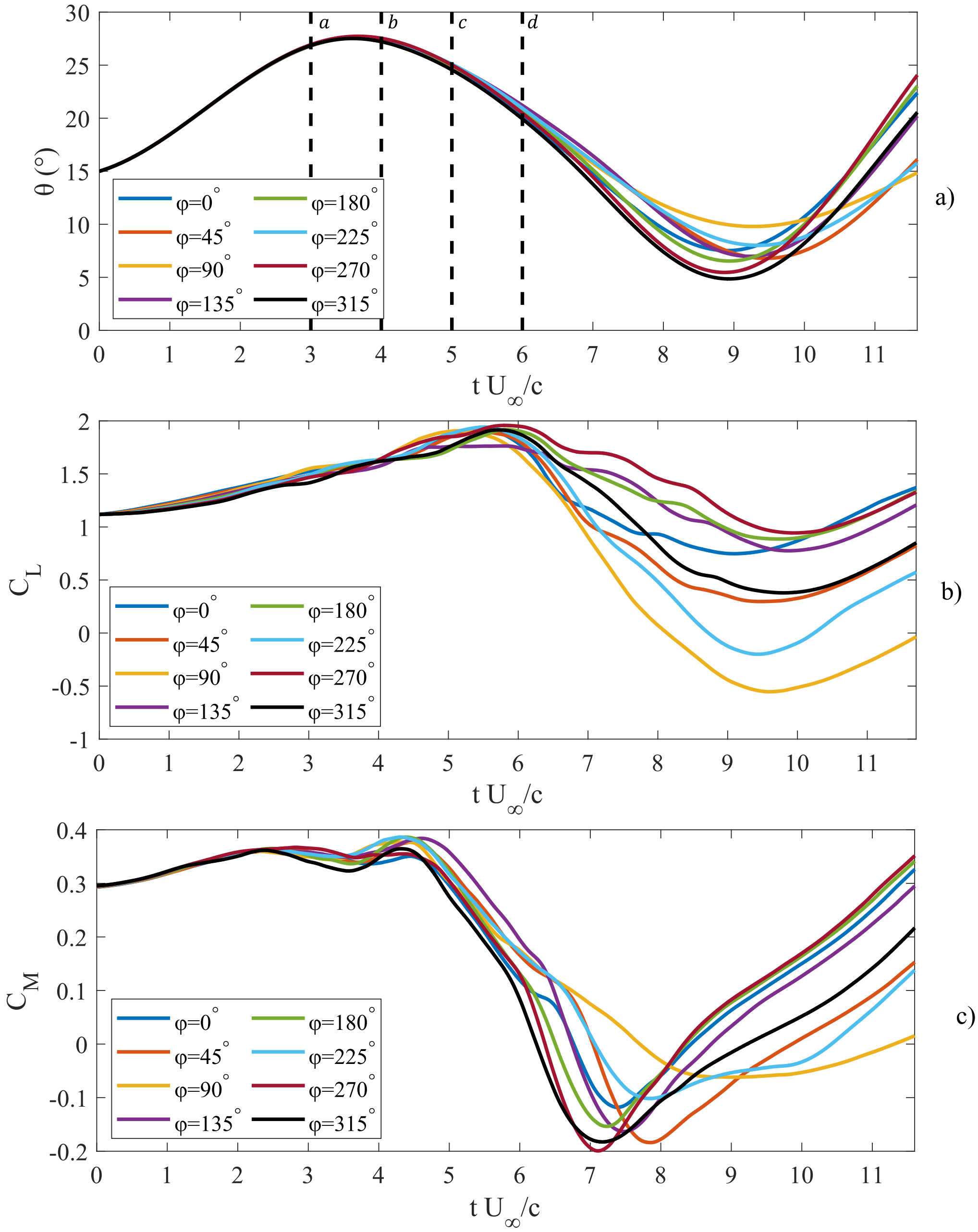

Figure 26. *a) Time-resolved pitching angle. b) Time-resolved aerodynamic lift coefficient. c) Time-resolved pitching moment coefficient. All plots are shifted horizontally with respect to* $\varphi = 0^{\circ}$.

This variability is quantified by computing the time-resolved standard deviation of both C_L and C_M, respectively (fig. 27). Note that this data was post-processed using a moving window average filter for better clarity. The C_L and C_M windows are approximately 1.3 and 0.8 time units respectively as our solver utilizes an adaptive time marching scheme. Both traces, scaled between zero and one, are maintained close to $\sigma = 0$ up until $t\frac{U_\infty}{c} = 3$ suggesting that the leading-edge shear layer formation and initial roll-up are comparable phenomenon. Between $t\frac{U_\infty}{c} = 5 - 6$, there is a sharp increase in σ_{C_L} that occurs near the time of dynamic lift stall, $t\frac{U_\infty}{c} = 5.65$. This potentially indicates that the LEV detachment and shedding mechanism(s) are largely responsible for transient lift variations across these parametric cases. This assessment is akin to a reduced frequency-based effect reported by Martinez et al. (2025) where varying K introduces a topological bifurcation in the LEV detachment mechanism. The behaviour of σ_{C_M} is much more complicated to diagnose as per the non-monotonic growth between $t\frac{U_\infty}{c} = 3 - 8$. Furthermore, moment stall is not necessarily coincident with LEV shedding but with a chordwise pressure shift corresponding to the LEV migration beyond the flexural axis. Interestingly though, a local minimum in σ_{C_M} also appears to be nearly coincident with the dynamic lift stall. We propose that the respective increases in σ_{C_L} and σ_{C_M} near dynamic lift stall are likely attributed to trailing-edge effects that alter how the LEV detachment process is actuated.

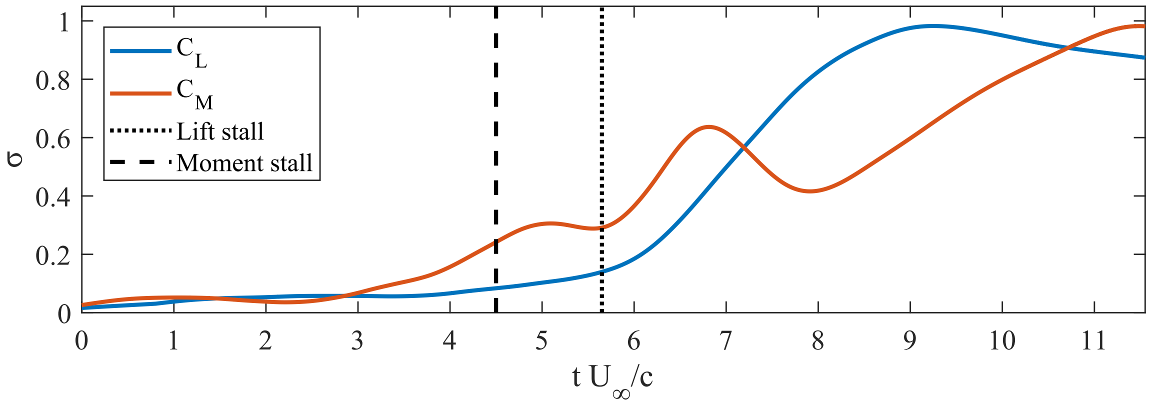

Figure 27. *Time-resolved aerodynamic lift and pitching moment standard deviations corresponding to data in figure 26. Dashed lines indicate timestamps associated with lift and moment stall, respectively.*

5.2 Transient Vortex Dynamics

To understand the time-dependent growth in parametric load deviations, we will consider various direct and indirect quantifications of the LEV dynamics in the vicinity of lift and moment stall. As such, the following analyses are conducted within a truncated time frame that approximately spans timestamps a, b, c, and d in figure 26a. First, an Eulerian vortex core tracking method is utilized to compare how the LEV trajectory varies between each parametric case. An approximate vortex core location is determined via localized thresholding of the out-of-plane vorticity field, ω_z. Next, a smooth spatial distribution is computed using a spanwise vorticity (ω_z) weighted kernel density estimate (KDE) of grid points that approximately enclose the target fluid structure. The peak value of this distribution corresponds to a vortex core location. This vortex monitoring procedure is repeated for each parametric case, $\varphi = 0^\circ - 315^\circ$, within a timeframe that captures the LEV detachment.

The ensemble averaged LEV trajectory is presented in figure 28 with x-component (yellow) and y-component (orange) error bars indicating the relative degrees of spatial variation between each parametric case study. The blue error bars correspond to the standard deviations in circulation determined by equation 52 and using a circular boundary around the manually identified vortex core. The radius of this boundary is determined by incrementally growing until the maximum vortex strength is observed.

$$\Gamma_{LEV} = \int_A \omega_z(x,y)\, dA \qquad (52)$$

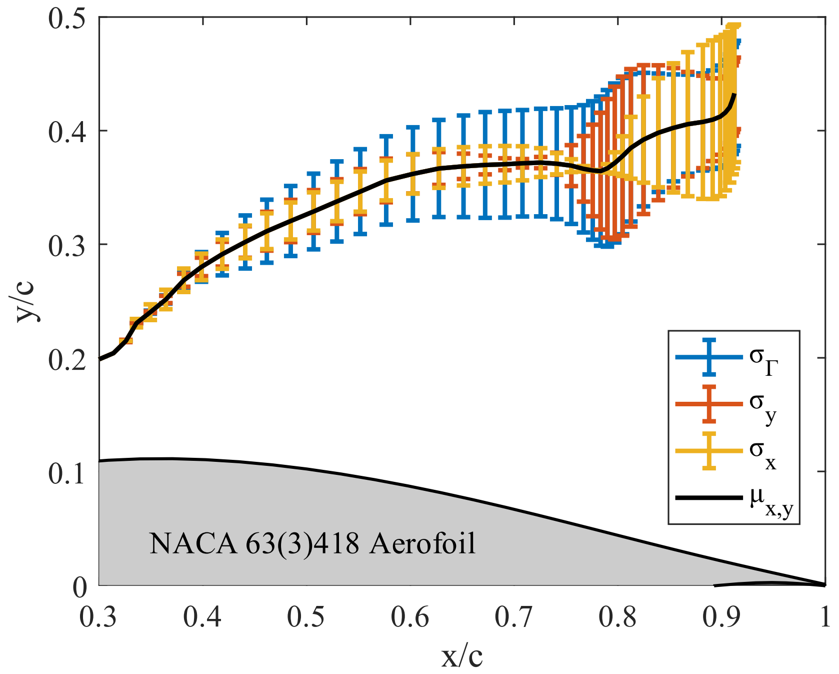

Figure 28. *Ensemble averaged trace of LEV core trajectory (black). Error bars correspond to the circulation (blue), $\frac{y}{c}$ (orange), and $\frac{x}{c}$ (yellow) standard deviations at each vortex core position.*

Similar to the aerodynamic load data, these error bars have been range normalized between $[0, 0.07]$ for comparing the relative variability of each respective metric, x, y, and Γ, along the trajectory path. The average LEV detachment location occurs at $\frac{x}{c} = 0.78$ as indicated by a core trajectory shift away from the aerofoil suction side. This changepoint coincides with both dynamic lift stall and a stark amplification in σ_{C_L} and σ_{C_M}. Furthermore, σ_x and σ_y experience similar relative growth between $\frac{x}{c} = 0.71 - 0.78$ suggesting that the LEV detachment mechanism is correlated to both unsteady lift and moment variations in the post-stall regime. The initial contraction before this LEV changepoint indicates a kind of concentrated focal point across all parametric cases that the LEV reaches prior to detachment. Though, σ_Γ does not contract in a similar fashion to σ_x and σ_y but instead increases monotonically up until the LEV detachment. Thus, the variations in the LEV induced circulation do not appear to be meaningful in specifying why σ_{C_L} surges after dynamic lift stall. This is not to say that that σ_{C_Γ} is non-contributory to σ_{C_L} or σ_{C_M} in the post dynamic stall regime but that a wide range of vortex strengths can exist regardless of LEV attachment or detachment.

A complimentary analysis of the LEV trajectory is also conducted using near surface measurements of the u and v velocity components. Time-resolved signals are sourced at six discrete probe locations along the aerofoil chord between $\frac{x}{c} = 0.025$ and $\frac{x}{c} = 0.95$ in equally spaced increments and at a distance $\frac{d}{c} = 0.01$ in the wall normal direction. These instantaneous probe measurements span the first starting cycle in our parametric range, $\varphi = 0^{\circ} - 315^{\circ}$, and serve as an indirect quantification of the time-resolved LEV progression along the aerofoil surface. At each probe, the velocity component signals are ensemble averaged with respect to φ. Also, the standard deviation is computed along each probe trace to indicate where the dynamic stall process is sensitive/insensitive to transient conditions. These results are shown in figure 29 where the time-resolved signals have been smoothed using a sliding window filter and plotted with a vertical offset ($\frac{u}{U_\infty} = 2$ and $\frac{v}{U_\infty} = 1.5$) for clarity. Finally, the dynamic lift and moment stall time-stamps are given as the coarse and fine dashed lines, respectively. As the LEV is formed and progresses over the aerofoil, flow reversal along the suction side wall is an indicator of both its position and strength. The troughs in figure 29a and the peaks in 29b are evidence of this LEV migration as it passes over the various (near) surface probes. Between $\frac{x}{c} = 0.58$ and $\frac{x}{c} = 0.95$, a peak in the u-component ensemble traces grows just aft of the LEV trajectory (red arrows). This growth is a signature of counter-clockwise fluid motion near the aerofoil trailing-edge that occurs as a consequence of the LEV detachment.

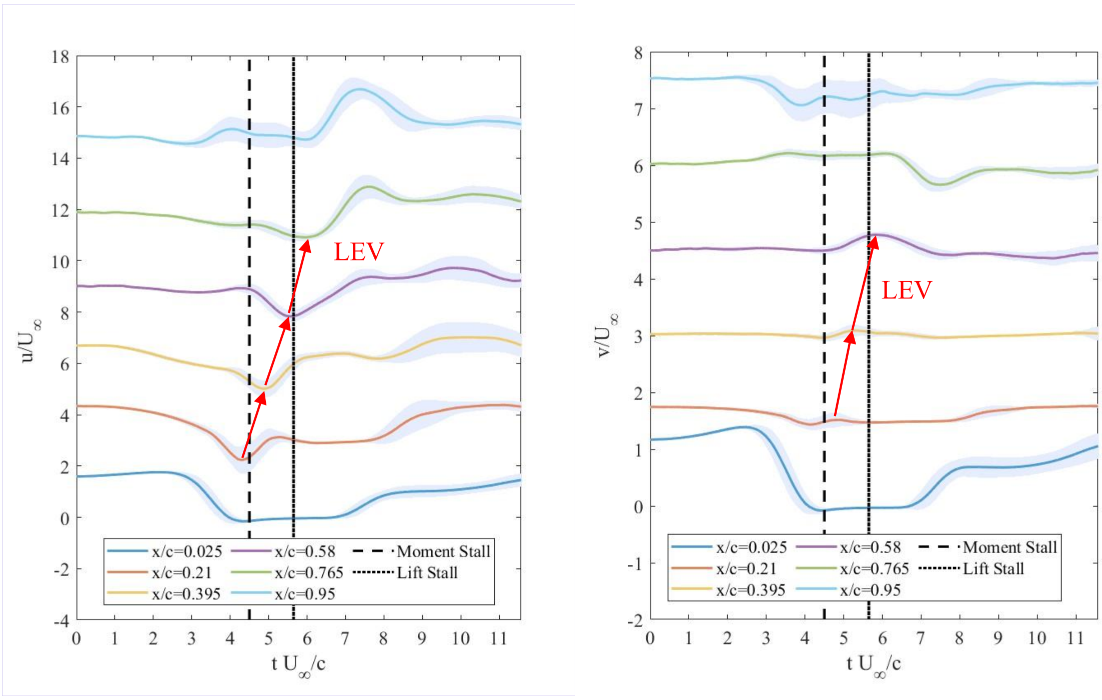

Figure 29. *a) Ensemble averaged u-component signals with standard deviation shade at various chordwise probe locations. b) Ensemble averaged v-component signals with standard deviation shade at various chordwise probe locations.*

At all probe locations, the u-component signal variations between $t\frac{U_\infty}{c} \approx 0 - 2.5$ are near zero indicating that the pre-stall regime is quite comparable regardless of φ. This behaviour is akin to our observations regarding σ_{C_L} and σ_{C_M} , where the load variations are small during the initial ramp-up portion of the cycle. Between moment and lift stall, these variations are largest at the $\frac{x}{c} = 0.95$ chord location indicating a wide range of trailing-edge dynamics just ahead of the LEV detachment timestamp.

5.3 Vortex Morphology

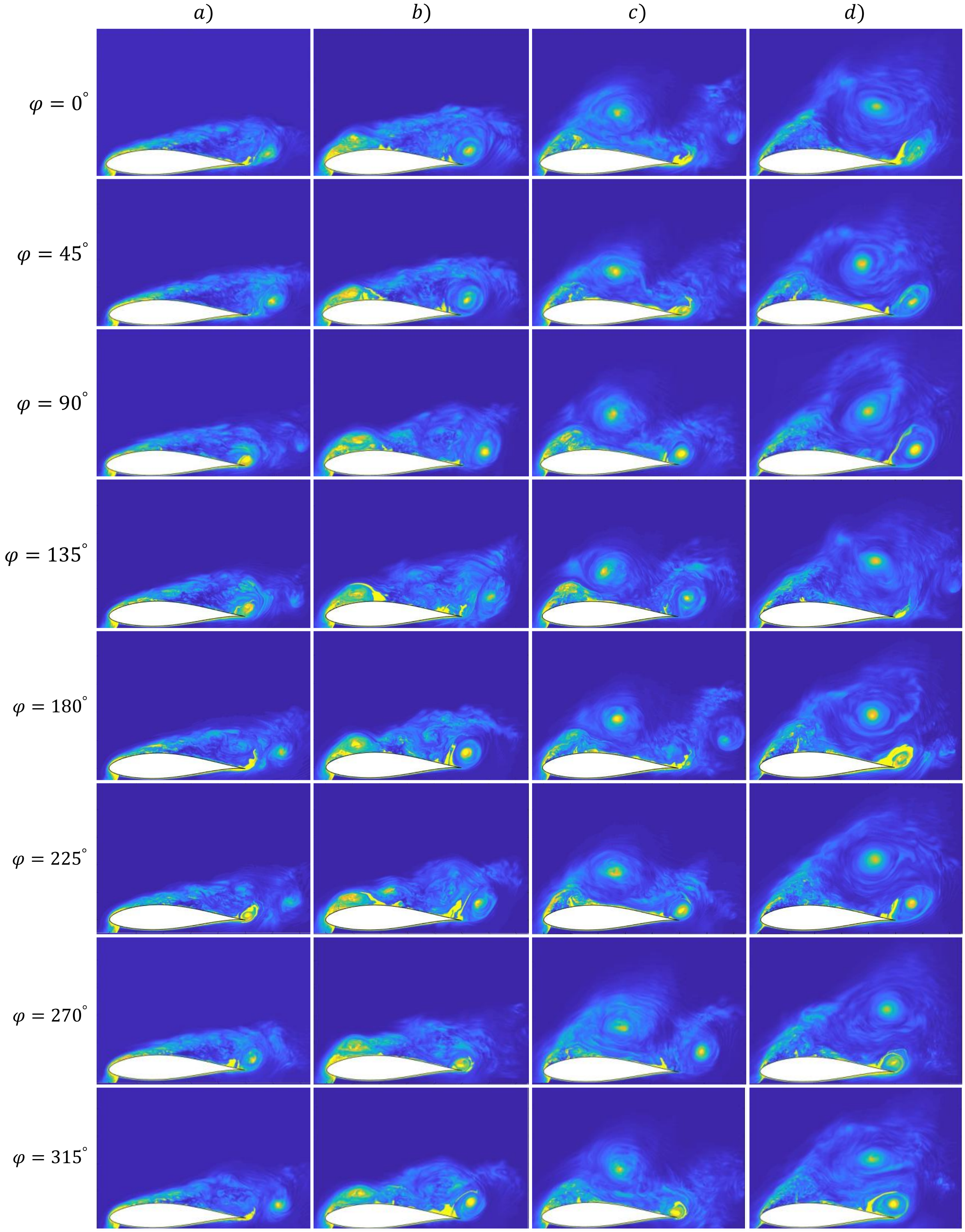

Figure 30. *LAVD contours scaled between 0 and 30 are computed at 4 timestamps within the pitching cycle (see figure 26a). Each row reflects the parametric variation in Kármán vortex phase angle evolving in time for column-wise alignment of dynamic stall events.*

While tracking the LEV structure grants critical insight into where/when detachment occurs, it does not necessarily reflect how this coherent structure is being altered on a case-by-case basis. We can only surmise that the LEV position and strength tend to vary as a consequence of strong trailing-edge interactions. To further diagnosis this behaviour, instantaneous field snapshots of the LEV are used to assess how this structure is altered by φ.

An analysis of the LEV structure is conducted to identify how the vortex morphology differs between the parametric cases due to detachment. More specifically, variations in the LEV boundary are examined via morphometric quantifiers like area, aspect ratio, and eccentricity. To conduct this analysis, Lagrangian averaged vorticity deviation (LAVD) field contours are computed near the dynamic lift stall event. To generate these LAVD fields, neutrally buoyant particle trajectories are computed by integrating equation 53 from t_0 to t using a 4$^{\text{th}}$ order Runge-Kutta method. Discrete field snapshots spanning this temporal evolution are interpolated linearly in both space and time to form a continuous trajectory. Seed particles are initialized at every grid centroid in a sub-domain region enclosing $-0.1 \leq \frac{x}{c} \leq 1.5$ and $-0.1 \leq \frac{y}{c} \leq 1$.

$$\dot{\boldsymbol{x}} = \boldsymbol{u}(\boldsymbol{x}, t) \qquad 53$$

Within this sub-domain, the instantaneous spatial mean of the out of plane vorticity component, $\overline{\omega_z(S)}$), is computed. The LAVD at each grid point is then formulated as the integral of the difference between the point vorticity along a trajectory path, $\omega_z(\boldsymbol{x}(S; \boldsymbol{x}_o), S)$, and $\overline{\omega_z(S)}$) given by equation 54.

$$LAVD(\boldsymbol{x}) = \int_{t_0}^{t} \left| \omega_z(\boldsymbol{x}(S; \boldsymbol{x}_o), S) - \overline{\omega_z(S)} \right| dS \qquad 54$$

A rotationally coherent Lagrangian vortex is defined as a nested set of material tubes that each exhibit uniform rotation relative to the mean vorticity. The singular center of this nesting, with radially increasing (inward) LAVD values defines the Lagrangian vortex core as per Haller et al. (2016). Figure 30 illustrates the intra-cycle LAVD contours computed at the timestamps in figure 26a. This timeline coarsely captures the leading-edge shear layer development (30a), its roll-up (30b), LEV saturation (30c), and vortex core trajectory shift associated with detachment (30d). As a visual diagnostic tool, the LAVD contours in figure 30 tend to demonstrate similar leading-edge shear layer development and incipient LEV formation. This is likely because the static separation point is too far aft to interact with the LEV genesis. Topological differences become pronounced at timestamp c) where the LEV feeding shear layer appears weak or severed for the cases $\varphi = 90^{\circ}, 135^{\circ}, 180^{\circ}, 315^{\circ}$. At timestamp d) there are obvious differences in the TEV development across all dynamic lift stall events. For phase angles, $\varphi = 90^{\circ}$ and $\varphi = 225^{\circ}$, a strongly coherent TEV forms just aft of the aerofoil trailing-edge as indicated by the nested LAVD peak. For the remaining scenarios, a TEV is either too weak to observe or has migrated onto the aerofoil surface. Indeed, the strength, size, and positioning of these observed trailing-edge structures plays a fundamental role in how the LEV is detached. Prior work on the detachment mechanism for varying reduced frequencies showed that it is possible for the TEV to act as a boundary that first impedes the LEV motion then directs it away from the aerofoil (Martinez et al., 2025). Alternatively, the TEV can become entrained between the LEV and suction side surface which severs the supplying shear layer and then pushes the LEV away. As such, it can be concluded that the unsteady load variations beyond dynamic lift stall are largely conditioned by how the TEV is formed. Temporal shifts within the Kármán vortex shedding phase angle can lead to either a constructive ($\varphi = 90^{\circ}$) or destructive ($\varphi = 135^{\circ}$) TEV formation that greatly impacts transient starting cycles.

A key benefit of utilizing LAVD versus other Lagrangian based vortex identification tools is that an explicit vortex boundary is defined as the largest convex member of a nested tubular family associated with a vortex core. This simple definition allows for analysing the LEV morphology throughout its lifecycle which can reveal fluid dynamic tendencies that are not easily identifiable through indirect metrics like the surface pressure and time-resolved aerodynamics loads. Here, a convexity ratio-based filtration scheme is utilized to identify the LEV boundary. Closed loop polygons around an LAVD peak are first granted candidacy as a potential vortex boundary. Next, a convexity ratio, $CR = 0.95$, is set as a lower limit to filter out boundaries that exhibit sufficient concavity.

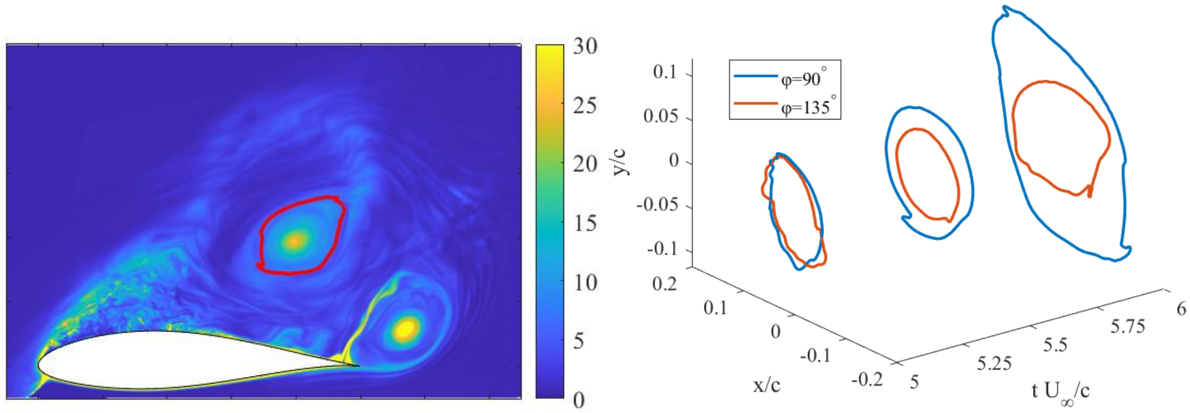

Figure 31. *a) LAVD contour for $\varphi = 90^{\circ}$ with identified vortex boundary around the LEV. b) Comparison of LEV boundaries between $\varphi = 90^{\circ}$ and $\varphi = 135^{\circ}$ near dynamic lift stall.*

CR is computed as the ratio of the enclosed area to the hull area as per (Bozeman and Pilling, 2013). Figure 31 exemplifies the results of this boundary detection procedure for the cases of $\varphi = 90^{\circ}$ and $\varphi = 135^{\circ}$ at three temporal snapshots, $t\frac{U_\infty}{c} = [5, 5.5, 6]$. All boundaries are centred by subtracting out their respective centroids. At several snapshots, the LEV boundary area (A), aspect ratio (AR), and eccentricity (e) are computed over the full parametric range, $\varphi = 0^{\circ} - 315^{\circ}$, to evaluate morphological variations around dynamic lift stall. These metrics are averaged with respect to φ and plotted at $t\frac{U_\infty}{c} = [5, 5.25, 5.5, 5.75, 6]$ in figure 32. Error bars quantify the φ dependent standard deviations in the LEV morphology due to the previously described trailing-edge interactions. The mean LEV area experiences approximately linear growth between this timeframe with very small deviations at $t\frac{U_\infty}{c} = 5$. As it progresses through dynamic lift stall ($t\frac{U_\infty}{c} = 5.65$), these variations amplify indicating that detachment greatly affects the LEV size. Most notably though, the LEV aspect ratio deviation shrinks dramatically at $t\frac{U_\infty}{c} = 5.5$ in a similar manner to σ_x, and σ_y when approaching detachment. Eccentricity follows a similar mean trend and error contraction to the aspect ratio indicating that the LEV morphology is approximately circular as the pitching aerofoil nears dynamic lift stall.

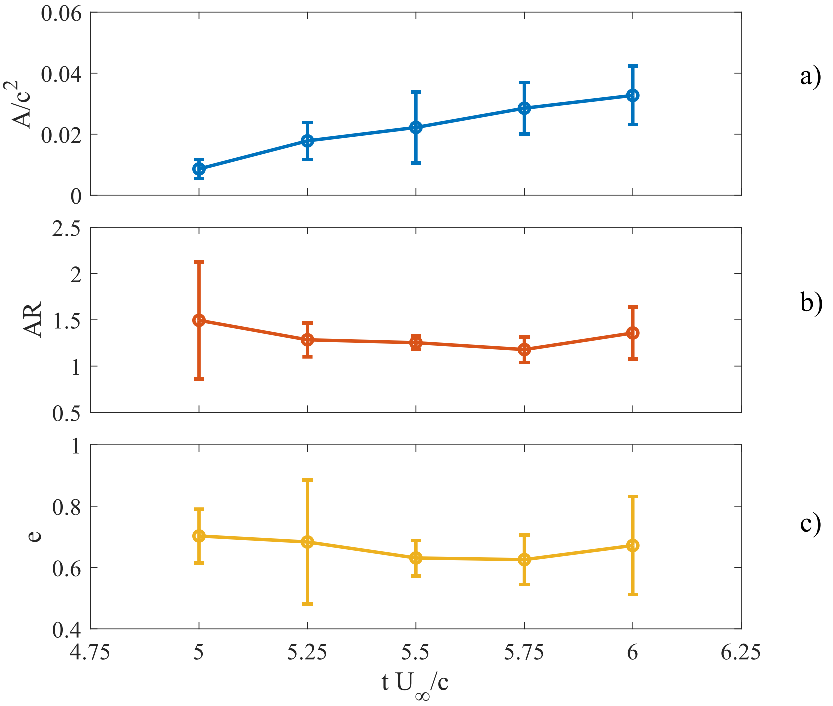

Figure 32. *a) LEV boundary area. b) LEV boundary aspect ratio. c) LEV boundary eccentricity. All metrics are averaged in φ and plotted at discrete timestamps around dynamic lift stall. Error bars express morphometric variations across φ.*

Chapter 6

6.1 Flow Control by Jet Blowing

The LEV structure can either be disrupted or entirely suppressed by application of surface jet blowing on the suction side of a lifting body. The capabilities of this flow control authority are dictated by several key parameters such as the jet location, strength, size, and orientation. Though, real-world constraints like the compressor, fluid storage unit, or delivery system size limit the practicality of flow control via constant blowing. Modern efforts have focused on scheduled or pulsed blowing as a means to achieve stall flutter suppression but through reduced fluid consumption rates. To build upon these efforts, we will consider the effects of the jet orientation angle on actuated blowing for alleviating unsteady aerodynamic loads in transient starting cycles. Note that our objective is not to optimise this control authority but to provide insight into how the dynamic stall process is affected by β.

We have demonstrated that operating very close to the static stall angle tends to influence the repeatability of the dynamic stall process owing to initial Kármán vortex shedding. As such, the mean incidence angle is set to $\alpha = 8^{\circ}$ to help attenuate this transient dependency while still being high enough to trigger a dynamic stall process. It has also been shown that reduced frequencies below $K = 0.2$ can lead to an invasive LEV-TEV interaction that further complicates the dynamic stall process. For this reason, the reduced frequency is fixed at $K = 0.4$ with nondimensional spring coefficient, mass moment of inertia, and damping coefficients set to $k = 0.029$, $J = 0.04531$, and $\mu = 0.01$. A steadily blowing jet patch is centred at $\frac{x}{c} = 0.2$ along the aerofoil suction side with width, $\frac{\Delta x}{c} = 0.05$, by means of a Dirichlet boundary condition. To ensure a smooth velocity gradient along the aerofoil surface, we assigned a Gaussian profile to the jet with a peak velocity centred at $\frac{x}{c} = 0.2$. This velocity magnitude profile is given in figure 33 along with the discrete values along the jet patch for a jet intensity

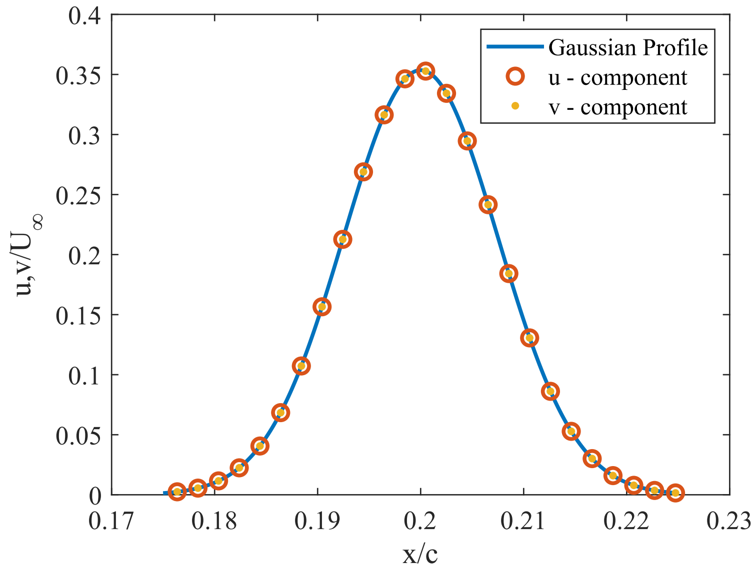

Figure 33. *u and v jet velocity distribution at an orientation angle of $\beta = 35.2^{\circ}$. β is measured relative to the aerofoil surface tangent between $\frac{x}{c} = 0.175$ and $\frac{x}{c} = 0.225$.*

value of $C_I = 0.5$. Note that for this work, the jet intensity metric, $C_I = \frac{U_{jet}}{U_\infty}$, is utilised rather than the momentum coefficient. This is because matching the momentum coefficient with experimental values in an incompressible flow requires either a very large jet patch or high jet speed. At high jet speeds, the simulation time step, Δt, becomes prohibitively small to satisfy the CFL condition near the aerofoil boundary. β is computed relative to a tangent line that intersects the end grid nodes enclosing our jet patch region. For jet-on conditions, the orientation angle is varied parametrically between $\beta = [2.2^\circ, 5.2^\circ, 12.\ ^\circ, 20.2^\circ, 27.\ ^\circ, 35.2^\circ]$. A single jet-off condition is also utilised for comparison. To ensure mass conservation, a correction factor is computed based on the jet influx, inlet influx, and domain outflux. The advection speed at our domain outlet boundary is then updated in time to correct for global mass conservation. Finally, as the jet patch is typically designed as a plenum slot or a distribution of holes along the wing surface in experimental studies, we have decided to neglect this surface patch when computing our time resolved aerodynamic loads to maintain consistency.

A demonstration of our boundary condition implementation during constant blowing conditions is presented in figure 34 where the time-averaged surface pressure coefficient distributions along the suction side are compared for all jet orientation angles and at $C_I = 0.5$. For orientation angles $\beta \geq 12.\ ^\circ$, it can be observed that the constant jet induces massive flow separation along the suction with very little variation between $\frac{x}{c} = 0.2$ and $\frac{x}{c} = 0.6$. Ahead of the jet patch, the leading-edge suction and adverse pressure gradient tend to degrade when increasing β. At these high β conditions, the jet behaves more like a physical obstruction that acts to deflect the boundary layer

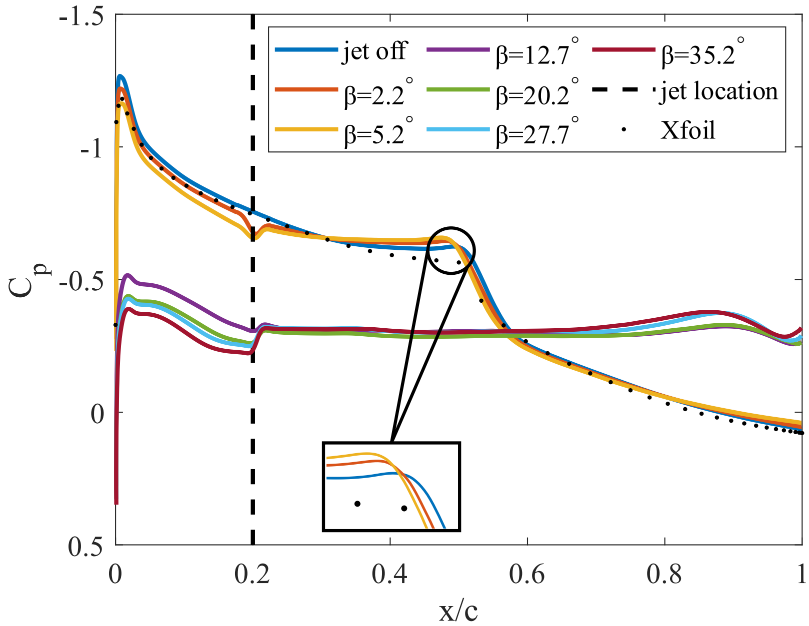

Figure 34. *Pressure distribution comparison over aerofoil suction side for* $\beta = [2.2^\circ, 5.2^\circ, 12.\ ^\circ, 20.2^\circ, 27.\ ^\circ, 35.2^\circ]$. *All jets are set at* $C_I = 0.5$. *Xfoil comparison at jet-off condition with* $N_{crit} = \ .$

At lower orientation angles, $\beta = [2.2^{\circ}, 5.2^{\circ}]$, the constant jet is less intrusive to the boundary layer attachment and shifts the laminar-turbulent transition point slightly forward of the baseline study. Next, the mean aerodynamic loads, C_L and C_D are plotted with respect to β to demonstrate how increasing the orientation angle influences static aerodynamic loading (fig. 35). It can be plainly observed that for all cases, constant jet blowing is actually detrimental to the static lift and drag coefficients. A clear distinction can be made between the aerodynamic load characteristics at $\beta = 5.2^{\circ}$ and $\beta = 12.\ ^{\circ}$ that is attributed to the jet induced boundary layer separation. Even at low values of β though, the surface jet is still mildly intrusive and leads to a slight reduction in the static lift and an increase in drag. Though, this aerodynamic deficit is not necessarily representative of its capability to moderate the dynamic stall process as weak or low-momentum jets can still significantly disrupt the formation of an LEV.

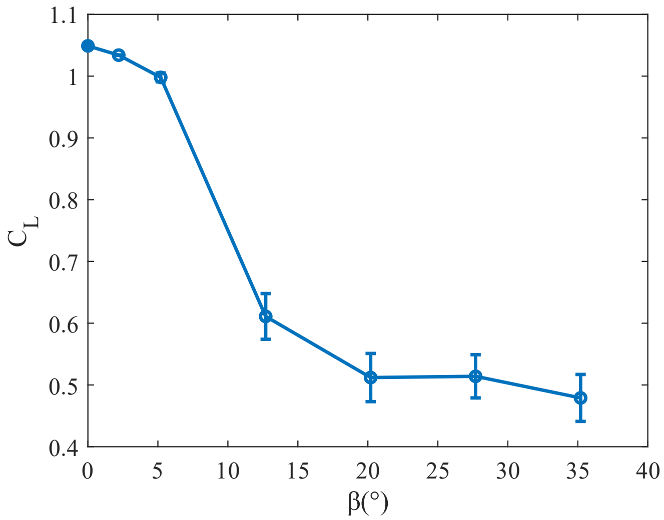

a)

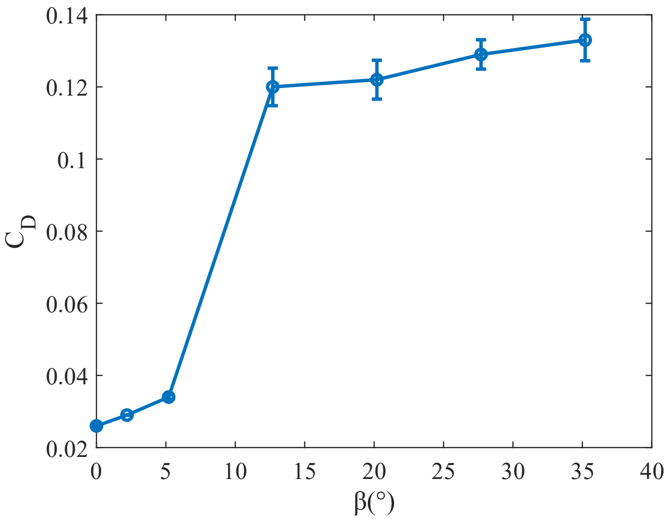

b)

Figure 35. *Static aerodynamic lift (a) and drag (b) coefficient values versus jet orientation angle for constant blowing conditions. Measurements were taken at an aerofoil incidence angle of* $\alpha = 8^{\circ}$. $\beta = 0^{\circ}$ *is representative of jet-off conditions.*

Müller-Vahl et al. (2015) demonstrated that low momentum jets can induce boundary layer separation which massively promotes LEV shedding during prescribed pitching motions. This disruption mechanism facilitates a decrease in the unsteady lift and moment hysteresis which is ultimately still favourable for fatigue mitigation. The objective of this investigation is not to optimise the jet control parameters but to assess how the LEV attenuation is affected by β in a scheduled jet actuation scenario.

For actuated jet conditions, our jet intensity profile takes the form of a sigmoid function to ensure a smooth actuation ramping within the aeroelastic pitching cycle. This function is given by equation 55 where u_{peak}, T_s, and T_r represent the peak jet velocity magnitude, the actuation start time, and the actuation delay time to reach its peak value. B controls the steepness of this jet actuation function and is fixed at 2 for all cases.

$$u_{jet}(t) = \frac{u_{peak}}{2}\left[1 \quad tanh\left(B\frac{t-\left(T_s \quad \frac{T_r}{2}\right)}{T_r}\right)\right] \qquad 55$$

6.2 Transient Load Response

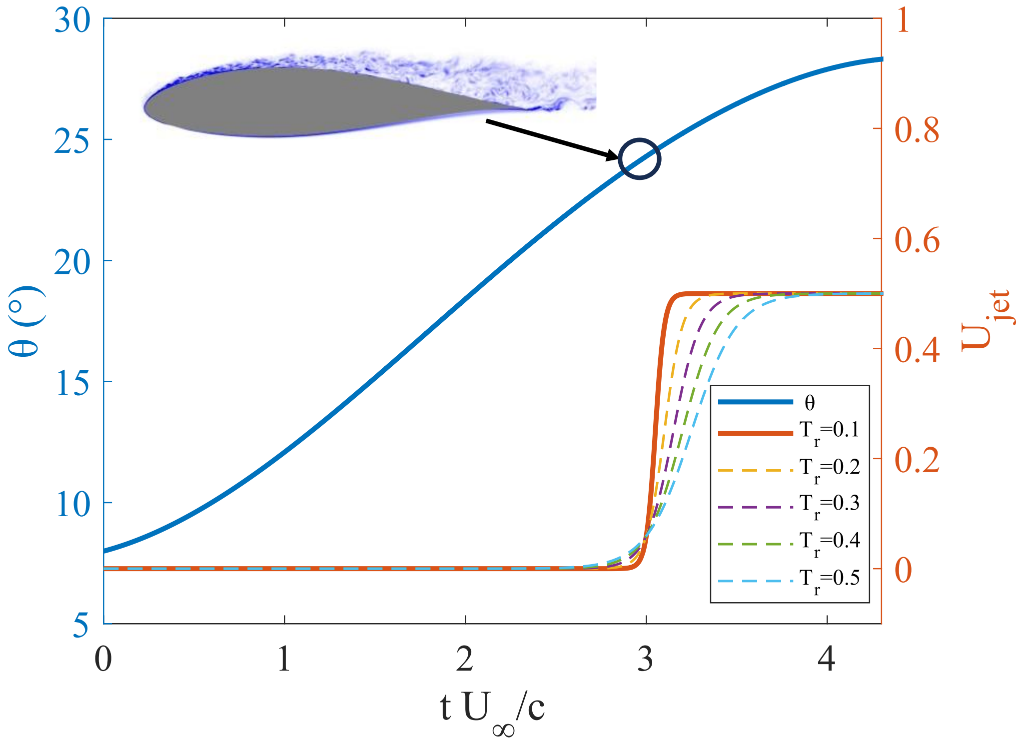

Figure 36. *Scheduled jet actuation profile during ramp-up portion of the transient pitching cycle for case $C_I = 0.5$. T_r is varied to demonstrate the smoothness of our actuation function.*

In this section, the effects of β on the unsteady aerodynamic loads are examined for actuated jet scenarios over a single pitching cycle. All simulations are first initialised using the baseline study with jet-off conditions. The jet actuation profile is provided in figure 36 where T_s and

T_r are set to $t\frac{U_\infty}{c} = 3$ and $t\frac{U_\infty}{c} = 0.1$, respectively. T_s was chosen based on the formation time of the LEV, i.e. just ahead of the maximum pitching angle in our baseline study. At this point along the pitching trace, flow reversal is present along the aerofoil surface but has not yet rolled up into the LEV. By actuating the jet ahead of the LEV roll-up regime, we expect to disrupt its formation and growth. T_r was chosen to ensure a smooth continuous ramping of the jet actuation profile and because real-world actuators are not instantaneous. These conditions are repeated for the entire parametric range of β and at $C_I = 0.8$.

To assess the impact of β on scheduled jet actuation during transient pitching cycles, the instantaneous aerodynamic load deviations, ΔC_L and ΔC_D are plotted with respect to the baseline jet-off case. See figure 60 in the appendix (A.3) for the baseline aerodynamic load traces. Starting with the cases for $C_I = 0.5$ in figure 37, it can be immediately observed that β dramatically influences the load augmentation behaviour throughout the dynamic stall process. Post-actuation, the orientation angles, $\beta = 5.2^{\circ}, 12.\ ^{\circ}, 20.2^{\circ}$, tend to promote temporary lift augmentation relative to the jet-off conditions. While potentially beneficial for systems exploiting vortex induced lift, this attribute is unfavourable from the purview of stall flutter and fatigue mitigation.

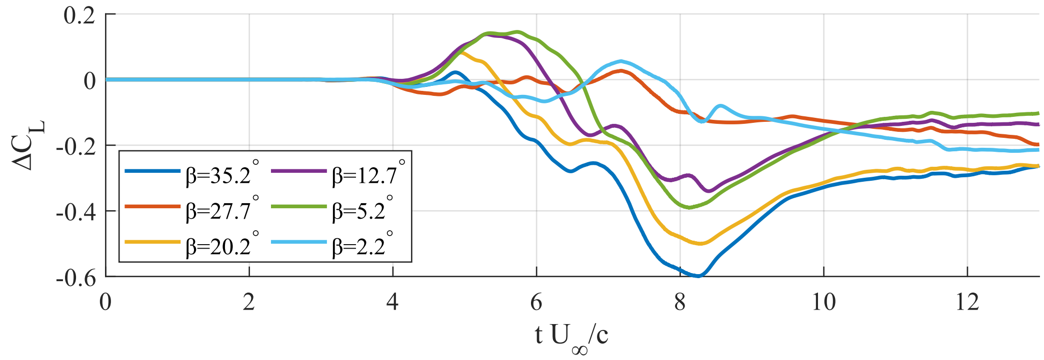

a)

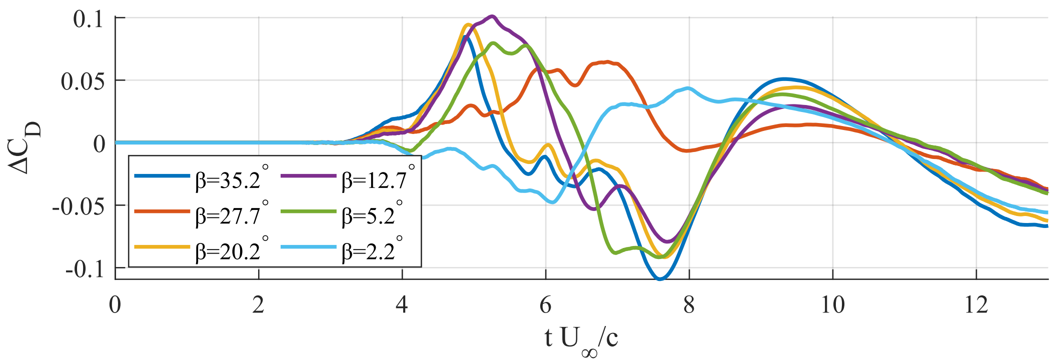

b)

Figure 37. *a) ΔC_L traces for all jet orientation angles and at $C_I = 0.5$. a) ΔC_D traces for all jet orientation angles and at $C_I = 0.5$. Differencing is computed with respect to the jet off C_L and C_D traces, respectively.*

The remaining cases appear to be lift attenuating throughout the majority of the pitching cycle indicating a favourable dampening of the dynamic stall process. An incurred penalty of this flow control authority is the intra-cycle rise in aerodynamic drag across all cases. Though, this increase is staggered within the dynamic stall process owing to when and how the LEV is shed from the aerofoil. For example, in cases $\beta = 35.2^{\circ}$ and $\beta = 20.2^{\circ}$ we can observe a sharp peak in ΔC_D prior to other cases which grants the impression of an accelerated dynamic stall process. This is different from the case of $\beta = 2.2^{\circ}$ where the temporary decrease in ΔC_D is associated with maintaining the boundary layer attachment at higher pitching angles. Overall, the case of $\beta = 37.5^{\circ}$ represents the most load attenuating condition with a mean aerodynamic lift and drag decrement of, $\overline{\Delta C_L} = -0.17$ and $\overline{\Delta C_D} = -0.004$ relative to the jet-off case study.

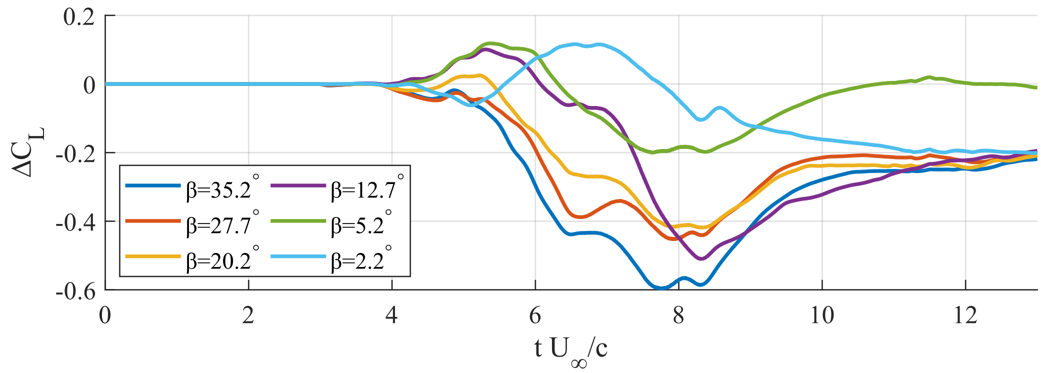

a)

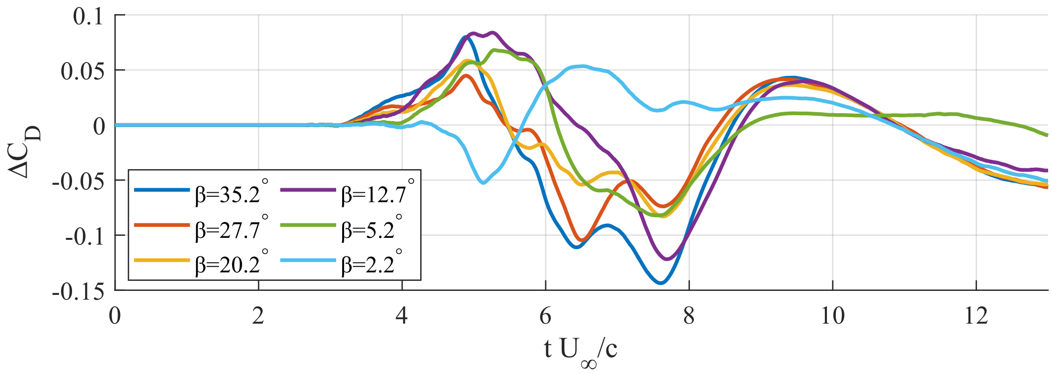

b)

Figure 38. *a) ΔC_L traces for all jet orientation angles and at $C_I = 0.8$. a) ΔC_D traces for all jet orientation angles and at $C_I = 0.8$. Differencing is computed with respect to the jet off C_L and C_D traces, respectively.*

At a higher jet intensity value, $C_I = 0.8$, the instantaneous load deviations are also plotted for comparison in figure 38. Some similar tendencies can be observed to the lower jet intensity profiles as the $\beta = 37.5^{\circ}$ case provides the overall best load alleviation potential with a mean decrement of $\overline{\Delta C_L} = -0.18$ and $\overline{\Delta C_D} = -0.015$ A significant change in ΔC_L occurs for the case of $\beta = 27.$ $^{\circ}$ when increasing the jet intensity. At $C_I = 0.8$ this orientation angle provides favourable lift attenuation and reduces the associated drag penalty with high angled jets. These results indicate that high jet orientation angles may be suitable for alleviating fatigue in susceptible aeroelastic structure. Though, it should be made clear that the mechanism associated with this type of flow control authority is attributed to disrupting the dynamic stall process rather than suppressing it.

Upon further inspection of the ΔC_L traces, it can be seen that several of the profiles exhibit a degree of shape similarity. In particular, the cases corresponding to $\beta = 35.2^{\circ}$ and $\beta = 20.2^{\circ}$ at $C_I = 0.5$ are approximately shifted copies of one another indicating comparable dynamic stall tendencies. A similar observation can be made for $\beta = 35.2^{\circ}$ and $\beta = 20.2^{\circ}$ at $C_I = 0.8$. In this particular instance, the likeness of the unsteady lift deviations is a signature of disruptive dynamic stall attributes that promote load attenuation such as early LEV detachment, drifting, interference, etc. As such, it is useful to quantify the similarity between these parametric cases to determine which jet actuation scenarios alter the dynamic stall process in a comparable manner. For this analysis dynamic time warping (DTW) (Sakoe and Chiba, 1978) with Euclidian distance is used to compute a distance matrix for the ΔC_L traces (fig. 39). DTW is preferable compared to a naive Euclidian distance in this work as it is suitable for time-series that exhibit similar shape but with local misalignments or stretching.

The shortest warping distance between two unique load deviation profiles is $d_{DTW} = 0.03$ and is between $\beta = 20.2^{\circ}$ at $C_I = 0.8$ and $\beta = 35.2^{\circ}$ at $C_I = 0.5$. Though, the lift deviation profile for $\beta = 35.2^{\circ}$ at $C_I = 0.5$ also shares shape similarity with several other cases indicating that these integral effects are not unique to one set of parametric conditions. Instead, a specific flow mechanism is likely responsible for minimising lift overshoot which can be achieved through comparable flow pathways. Cases demonstrating both high shape similarity, $d_{DTW} \leq 0.1$, and significant lift alleviation potential, $\overline{\Delta C_L} \leq -0.1$, are highlighted with red borders to classify parametric cases that exhibit similar load alleviation capabilities and through *potentially* consistent mechanisms. To determine if these mechanisms are consistent though, a more in-depth analysis of the dynamic stall process is required. Specifically, information regarding how the actuated jet affects the LEV formation, its downstream advection, and detachment process are necessary to link these favourable jet parameters (red boxes) to unsteady lift alleviation.

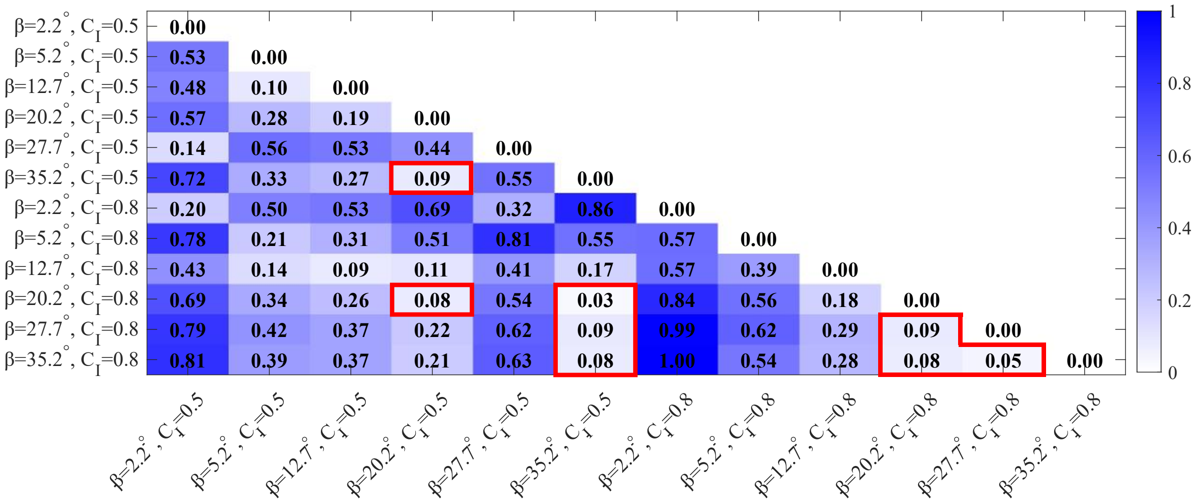

Figure 39. *Distance matrix between all ΔC_L traces utilising the Euclidian distance between warped signals. Distance values (d_{DTW}) are scaled between 0 and 1. Red boxes indicate clusters traces that satisfy both* $\overline{\Delta C_L} \leq -0.1$ and $d_{DTW} \leq 0.1$.

6.3 Global Proper Orthogonal Decomposition

The lifecycle of the dynamic stall process can be expressed through surface pressure measurements along the aerofoil suction side to indicate the chordwise position and strength of an LEV. How β alters this process is particularly important to provide a link to the fluid dynamic mechanisms responsible for load attenuation/augmentation. To dissect these mechanisms, we utilise global proper orthogonal decomposition (POD) of the time-varying pressure distribution for all parametric cases which closely resembles the setup of (Nikoueeyan and Naughton, 2023). Surface pressure measurements were taken along the aerofoil suction side and averaged along the homogenous spanwise direction throughout the entire pitching cycle. These measurements were taken every ten timesteps which corresponds to a resolution of approximately $\Delta t \frac{U_\infty}{c} \approx 0.0015$ due to adaptive time marching. Surface pressure fluctuations, p', were organised into a global data set given by equation 56 where N represents the total number of case studies. Here, we utilise the entire range of β for both $C_I = 0.5$ and $C_I = 0.8$ and a jet-off case such that $N = 13$.

$$X = [X_1, X_2, \dots, X_N] \tag{56}$$

The contents of matrix X are the pressure fluctuation snapshots for each case study given by equation 57, where each column represents its distribution along the aerofoil chord at a given timestamp. The rows express how the probe-wise pressure fluctuations evolve over time. To ensure a consistent number of columns, we interpolated between pressure measurements such that each time vector is uniform. T is the total number of temporal snapshots to build the POD.

$$X_n = \frac{1}{\sqrt{T}} \begin{bmatrix} p'(x_1, t_1) & \cdots & p'(x_1, t_T) \\ \vdots & \ddots & \vdots \\ p'(x_i, t_1) & \cdots & p'(x_i, t_T) \end{bmatrix} \tag{57}$$

Next, we utilise the singular value decomposition (SVD) of X to find the globally dominant spatial modes, φ_i, and compute the projection of p' onto φ_i.

$$a_i(t) = \langle p'(x,t), \varphi_i(x) \rangle \tag{58}$$

This allows us to meaningfully compare the time-varying coefficients, a_i, across the parametric space as computing the individual POD does not guarantee modal alignment between different cases of β even when similar dynamics are present. A subset of the source pressure distribution data is presented in figure 40 for the case of $C_I = 0.5$ where the jet orientation angle varies between a) and f) as $\beta = [2.2^\circ, 5.2^\circ, 12.\ ^\circ, 20.2^\circ, 27.\ ^\circ, 35.2^\circ]$. See figure 49 in section A.3 for the spatial-temporal pressure contours corresponding to cases at $C_I = 0.8$.

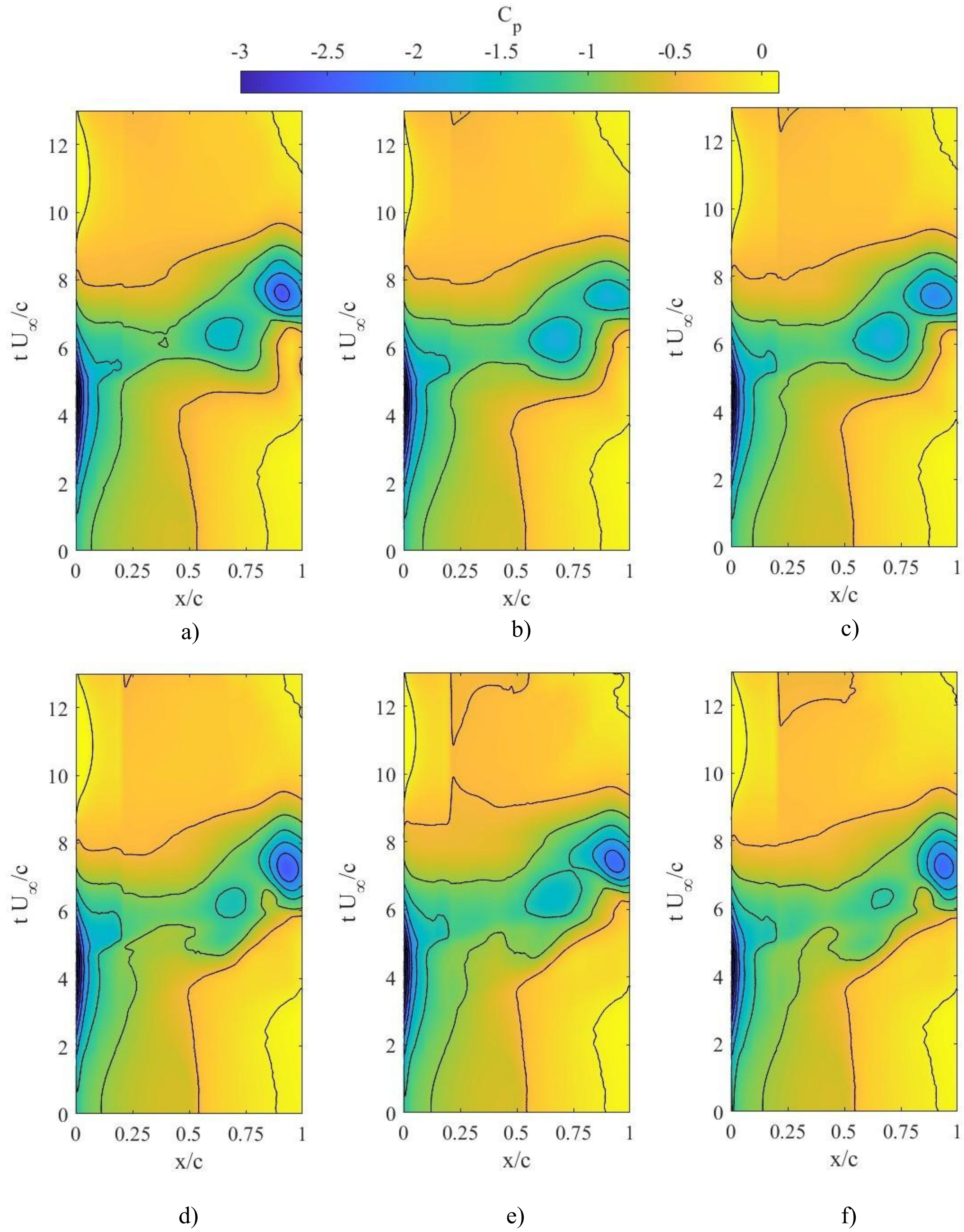

Figure 40. *Space-time pressure coefficient distribution contours along the aerofoil suction side for jet cases at* $C_I = 0.5$*.* β *varies in ascending order from a) to f).*

By computing the cumulative energy fraction of the computed POD modes (fig. 41), it can be observed that the first four modes represent a significant energy fraction of the entire spectrum (99.17%). For this reason, our analysis of the flow field dynamics will be contained to modes one through four. These first four global POD modes are presented in figure 42 where some observations can be made about the dynamic stall process captured by each spatial mode. First,

Φ_1 appears to represent the pressure distribution contribution during attached flow scenarios as its shape is quite similar to the static distribution presented in figure 34. Next, while Φ_2 is not purely monotonic, the adverse pressure gradient encompassing a majority of the aerofoil chord can be linked to a separated flow state. Φ_3 has a strong peak near the at $\frac{x}{c} = 0.93$ and represents the trailing-edge vortex (TEV) roll-up that can aid in obstructing the LEV growth. Alternatively, the TEV can form as a consequence of the LEV rear stagnation point moving beyond the aerofoil trailing-edge which enables the supply of counterrotating fluid (Kissing et al, 2020). Finally, the plateaued region observed in Φ_4 can be attributed to an induced suction peak by the LEV prior to detachment. Within this regime, it has been shown that the LEV structure can loiter prior to its detachment as per a contraction in chordwise LEV trajectory standard deviation (Martinez et al., 2026). This halting period that precedes the LEV trajectory shift depends on the type of detachment mechanism that is actuated. For example, an invasive LEV-TEV interaction has been identified where the TEV can migrate onto the aerofoil surface prior to the LEV reaching saturation (Martinez et al., 2025). This introduces a 'squeezing' type phenomenon between upstream and downstream secondary structures that tends to accelerate LEV detachment.

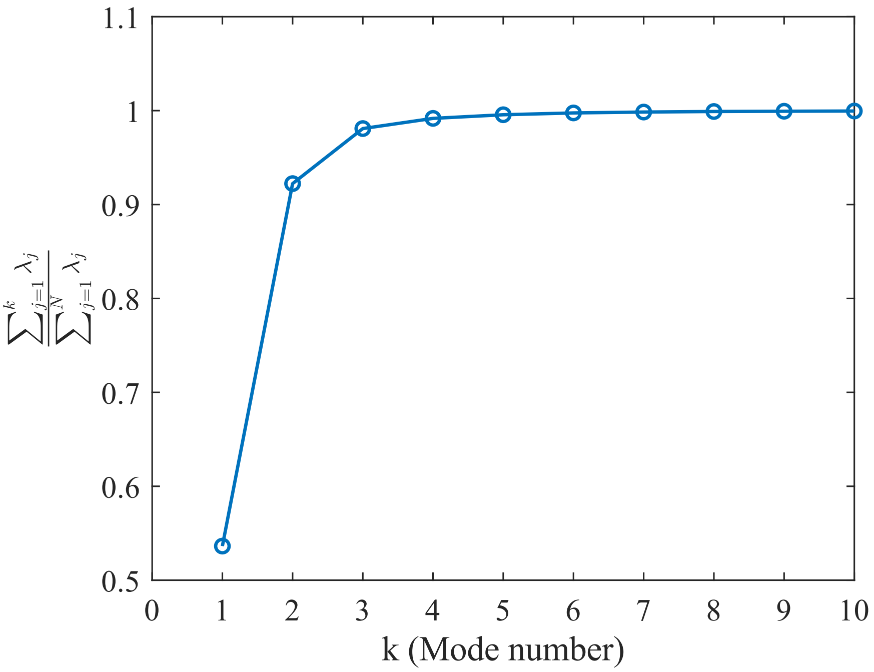

Figure 41. *Cumulative energy fraction versus mode number up to $k = 10$ modes. First four modes represent 99.17% of the total energy contribution.*

The time-varying coefficients, a_i, corresponding to each spatial mode are plotted in figure 43 where bold and dashed indicate $C_I = 0.5$ and $C_I = 0.8$, respectively. It can be immediately observed that a_1 is nearly identical across all parametric cases indicating that the attached flow behaviour during these transient pitching cycles are quite comparable. a_2 also reflects similar tendencies associated with the purely stalled conditions and is out of phase with a_1. Together, the first two spatial-temporal modes reflect the periodic switching behaviour between attached and stalled flow conditions throughout the respective pitching cycles. Case-dependant variations become pronounced in a_3 between $t\frac{U_\infty}{c} = 4$ and $t\frac{U_\infty}{c} = 9$ where the dynamic stall process takes place. For cases $\beta = 35.2^{\circ}$and $\beta = 20.2^{\circ}$ at $C_I = 0.5, 0.8$, the TEV signature appears much earlier in the cycle than the remaining cases as indicated by the respective peaks in a_3. This implies that the TEV rollup does not occur as a consequence of the LEV rear stagnation point passing over the trailing edge. Rather, it forms during the LEV growth stage and can be considered invasive. The effects of this invasive detachment process can be more clearly identified in the a_4 traces.

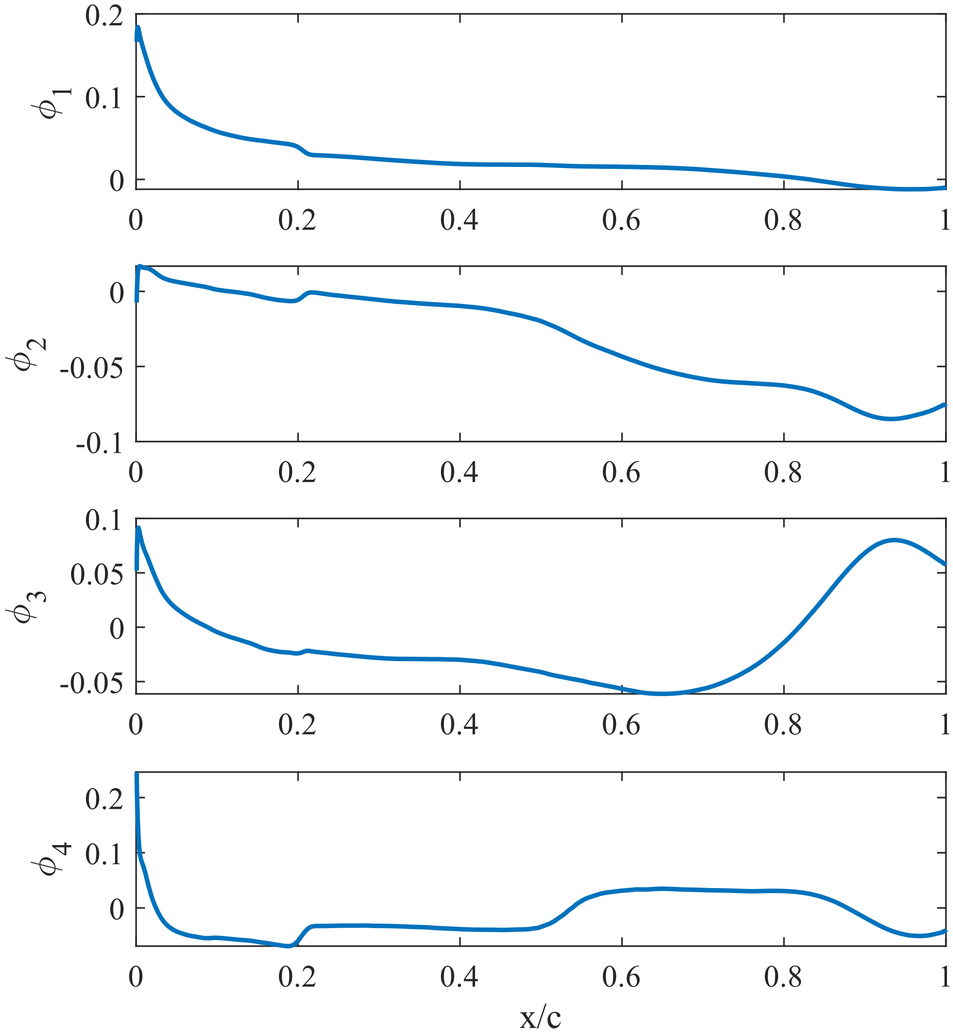

Figure 42. *Top four global pressure POD modes organised based on the cumulative energy fraction (fig. 41). Modes are shown in descending order.*

For $\beta = 35.2^{\circ}$and $\beta = 20.2^{\circ}$ at both jet intensities, a_4 demonstrates nearly monotonic growth between $t\frac{U_\infty}{c} = 5.5$ and $t\frac{U_\infty}{c} =$ while the remaining cases show signs of temporary periodicity. If the LEV detachment is independent of the aerofoil chord, then its pressure signature is difficult to distinguish from the TEV as they are both present on the suction side simultaneously. In cases where the LEV is allowed to move beyond the aerofoil trailing-edge though, a_4 follows a sequential evolution that reflects the LEV rear stagnation point passing over the trailing-edge, the introduction of counter rotating fluid, and formation of a TEV (Cases other than $\beta = 35.2^{\circ}$ and $\beta = 20.2^{\circ}$ at $C_I = 0.5, 0.8$).

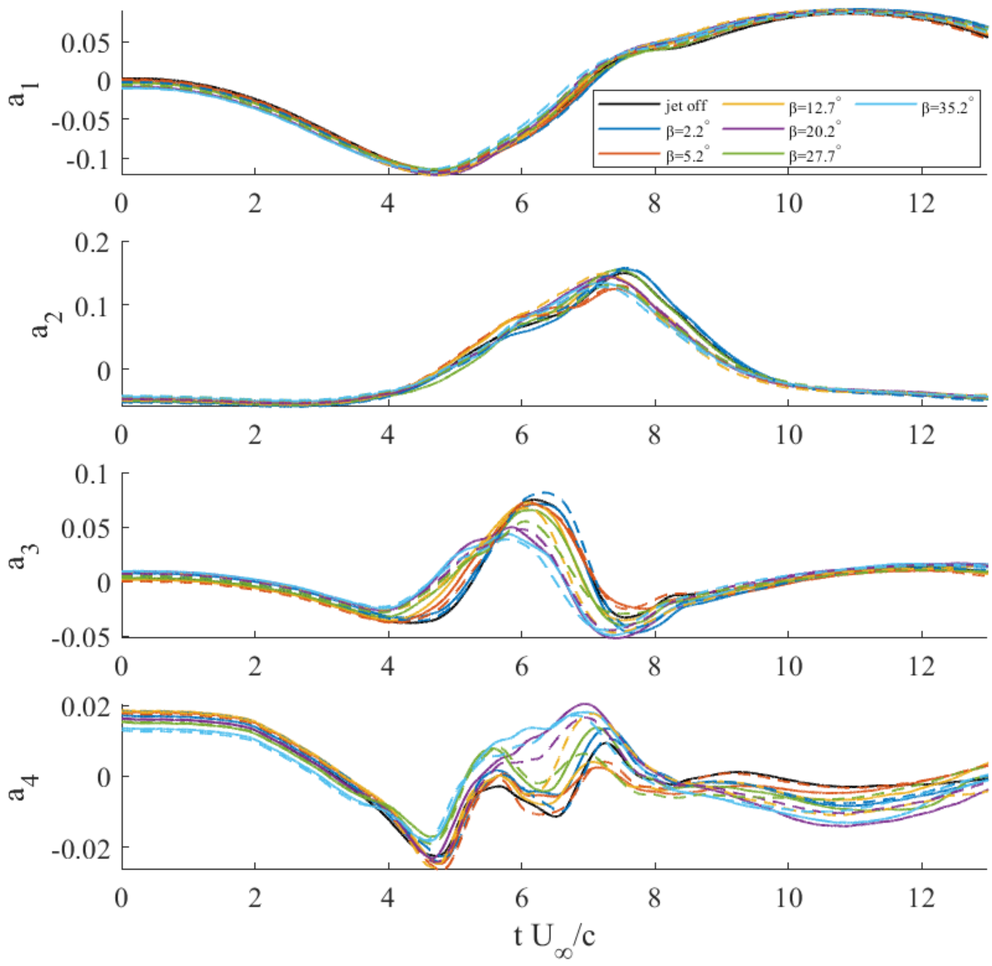

Figure 43. *Global POD mode coefficients for all values of β plotted versus time. Bold and dashed lines indicate cases for $C_I = 0.5$ and $C_I = 0.8$, respectively.*

To link these observations to the flow field topology, velocity magnitude snapshots are taken starting at $t\frac{U_\infty}{c} = 5.5$ for the cases $\beta = 2.2^{\circ}, C_I = 0.8$ (fig. 44a) and $\beta = 35.2^{\circ}, C_I = 0.8$ (fig. 44b). Timestamps are presented in each snapshot to demonstrate the evolution of the dynamic stall process within truncated window of the pitching cycle For brevity, these cases will be referred to as case a) (benign) and case b) (invasive) to distinguish between the respective detachment mechanisms. In case a), the relative LEV roll-up and subsequent detachment are delayed. This permits the LEV to grow in both size and strength because there are no mechanisms available to impede its development. This ultimately leads to a temporary increase in ΔC_L which demonstrates that jet actuation could potentially exacerbate the stall flutter instability. Comparatively, the vortex development in case b) is substantially altered by the high jet orientation angle. These specific control parameters promote an earlier LEV rollup but also introduce the formation of a TEV. This TEV structure obstructs the LEV chordwise migration and changes the detachment length scale. Additionally, introducing recirculation between the LEV and suction side helps to sever the supply of leading-edge vorticity. These conditions are reminiscent of a reduced frequency-based effect where pitching between $K = 0.15 - 0.19$ introduces a similar invasive detachment behaviour (Martinez et al., 2025).

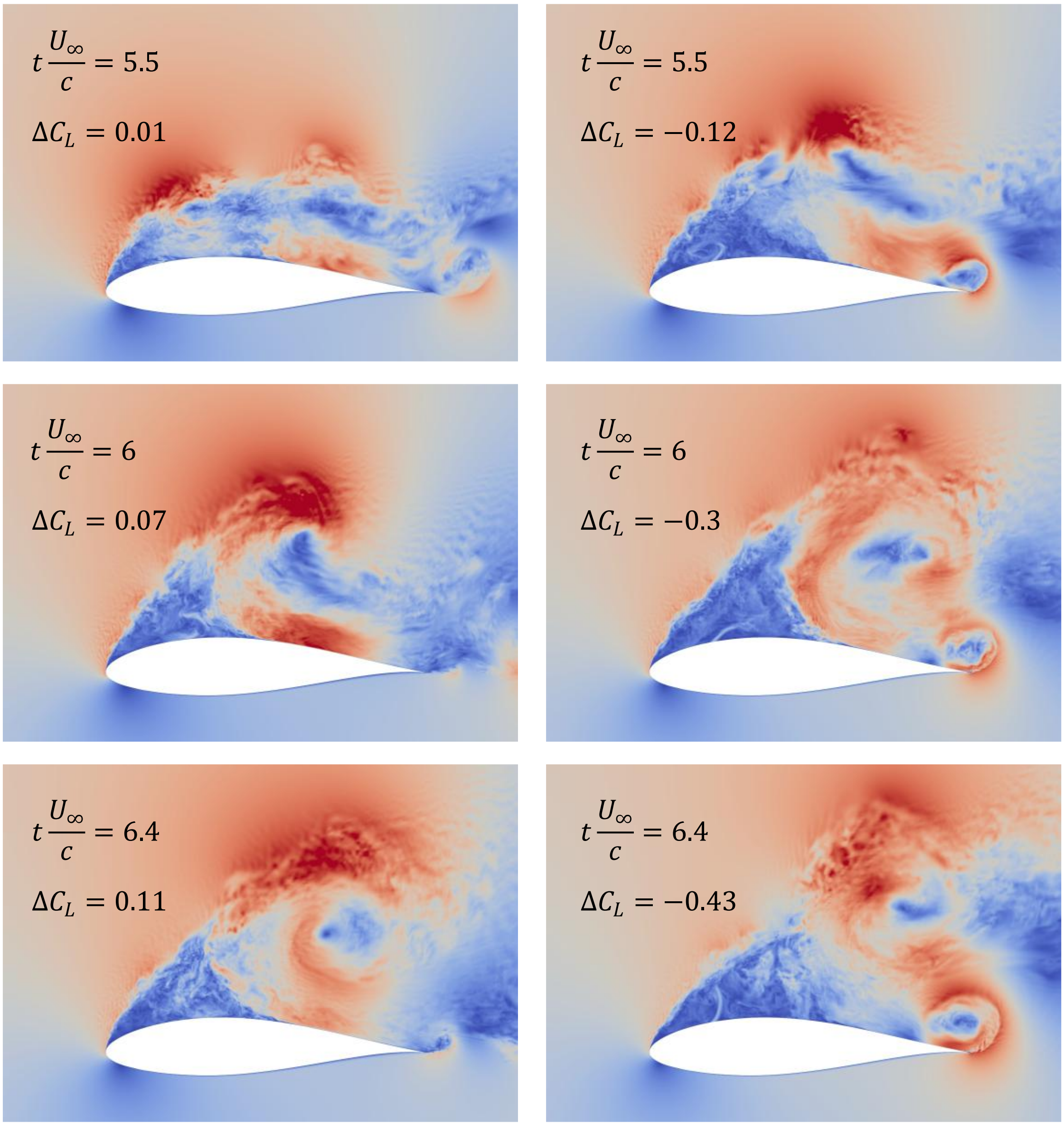

a) b)

Figure 44. *Snapshots of the dynamic stall process for a)* $\beta = 2.2^\circ$ *b)* $\beta = 35.2^\circ$. *Both cases have* $C_I = 0.8$. *Field contour is coloured by the velocity magnitude,* $0 \leq \|\boldsymbol{v}\| \leq 2.3$.

Jain and Saha (2020) and Valls Badia et al. (2025) both reproduced an invasive detachment phenomenology owing to an increase in the aerofoil thickness to chord ratio and by adding tubercles to the leading-edge, respectively. The jet actuation cases for $\beta = 35.2^\circ$at $C_I = 0.5$, for $\beta = 20.2^\circ$ at $C_I = 0.5$ and $\beta = 20.2^\circ$ at $C_I = 0.8$ yield similar flow field topologies that account for their favourable load alleviation potential.

We have demonstrated that the fourth global POD mode contains the energy fraction responsible for either type of detachment process. By altering this mode through a combination of the jet orientation angle and jet intensity, it is possible to generate circumstances that promote early LEV detachment. As a final comment, cases $\beta = 35.2^{\circ}$ at $C_I = 0.5$, $\beta = 35.2^{\circ}$ at $C_I = 0.8$, $\beta = 20.2^{\circ}$ at $C_I = 0.5$, $\beta = 20.2^{\circ}$ at $C_I = 0.8$, are all highlighted within the previously computed distance matrix by red boxes (fig. 39). With the exception of $\beta = 27.\ ^{\circ}$ at $C_I = 0.8$, all of these highlighted parametric conditions trigger an invasive LEV detachment mechanism that permits substantial lift alleviation. This provides a potential route for jet-based control authorities to exploit for mitigating stall flutter but at a lower injection cost relative to constant blowing strategies that aim to completely suppress the dynamic stall process.

Chapter

7.1 Vortex Core Identification and Tracking

Tracking and monitoring of large-scale coherent structures in fluid flows is an important task across various engineering and scientific disciplines. This has been clearly evidenced within the current thesis as the LEV trajectory path grants an indication as to which spatial-temporal regime of the dynamic stall process is present. To conduct vortex tracking measurements, it is common to evaluate the LEV core trajectory using metrics such as the Q-criterion, swirl criterion, and vorticity, to name a few (Martinez et al., 2025), (Lee et al., 2022), (Rosti, 2016), (Soto-Valle et al., 2022). Though, many Eulerian based definitions often suffer from spurious vortex identification in high Reynolds number flows that can make vortex monitoring highly challenging and case specific. Often, time-resolved monitoring of a particular vortex of interest requires an extended pipeline including methods such as thresholding, filtering, or clustering.

Some recent advances in the field of vortex core identification/monitoring have implemented tools like DBSCAN clustering (Ibáñez et al., 2025) supervised machine learning (Lee et al., 2022), and computer vision-based techniques (Xu et al., 2023) to successfully identify and monitor vortices. A relatively niche solution space to this objective is by using template or pattern matching. In this case, a template is either identified or generated by the user that encompasses the approximate composition of a target. This type of pattern recognition task has roots in image-based segmentation/classification and is often quantified through a distance or similarity field metric. A similar objective can be applied to fluid flows where a template is provided to identify certain fluid dynamic events. To assist in automating the LEV tracking workload of this research project, we leverage topological data analysis (TDA) as a tool for simplified template matching in dynamically stalled flows. Specifically, we utilise persistent homology to quantify the feature space similarity between a template-target pair via construction of a simplicial complex. The logic behind this strategy is that the LEV can have a wide range of strengths, sizes, and shapes owing to various dynamic stall related events. This makes direct 'image-like' pairing operations like convolution or RMSE potentially sensitive to template noise, orientation, and its absolute distance. Conversely, persistent homology provides a mechanism for mapping high-dimensional flow field data to a common low dimensional feature space that is both resilient to noise and invariant to template/target rotations. This abstraction also does not require dimensionality matching or grid uniformity for a direct template-target comparison making it natural for applications in unstructured and non-uniform CFD domains. We refer the readers to section A.1 for further background on persistent homology along with a canonical example of its application to a 2D point cloud with noise. Here, persistent homology is applied to a higher order data set, but the data construction and underlying methodologies remain consistent with this example case.

7.2 Vortex Template Matching

In this section, we outline a novel post-processing pipeline for tracking the LEV core in our stall flutter simulations. This methodology is applied to field snapshots spanning a temporal window that encloses various dynamic stall related events such as the chordwise LEV migration, its detachment, and shedding behaviour at an approximate temporal resolution of

$\Delta t \approx 0.05 \frac{t\,U_\infty}{c}$ due to adaptive time marching. This segmented window is illustrated by the black dashed lines in figure 45 that isolate a portion of the pitching trace for our pitching aerofoil at a reduced frequency of $K = 0.4$.

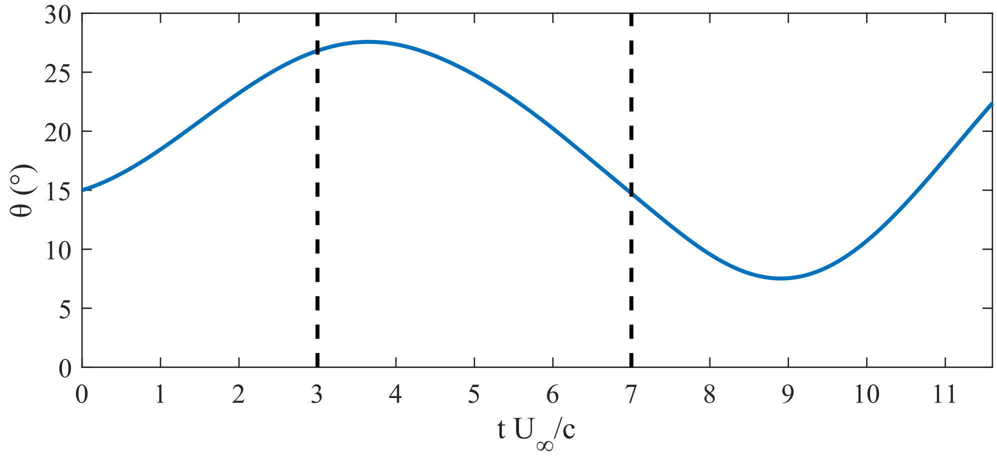

Figure. 45. *Aeroelastic starting cycle in pitch degree of freedom. Black dashed lines indicate temporal limits where field data is sourced from. Field snapshots are taken at a temporal resolution of* $\Delta t \approx 0.05 \frac{t\,U_\infty}{c}$.

Starting from a developed LEV status, computed velocity components, pressure and spanwise vorticity field data u, v, p and ω_z are manually sourced within a circular region of interest (ROI) with radius r that approximately encloses the vortical structure core.

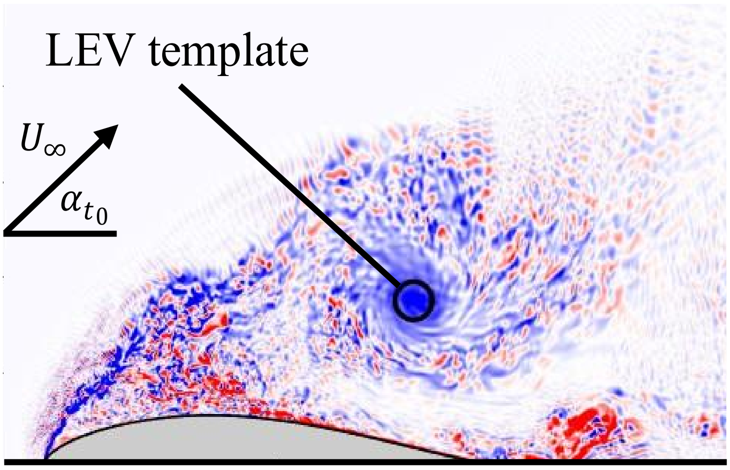

Figure 46. *ω_z field with manually defined LEV template source. ω_z range set between* $-50 \leq \omega_z \leq 50$.

In this case, the template is defined at the location, $x, y = (0.8024c, 0.3509c)$, with a radius, $r = 0.04c$. These sourced field variables are used to describe the LEV in R^4. Next, we compute the persistence diagram for this high-dimensional point cloud up to and including the homology dimension, $k = 1$. Figure 47 demonstrates the results of this computation given by the blue and orange dots ($H0 - t_0$, $H1 - t_0$), indicating a variety of topological features ranging between persistent holes and short-lived artefacts. An example of the manually identified LEV persistence diagram at a latter timestep, t_1, is also overlayed as the yellow and purple dots ($H0 - t_1$, $H1 - t_1$) in figure 47 and exhibits similar topological features.

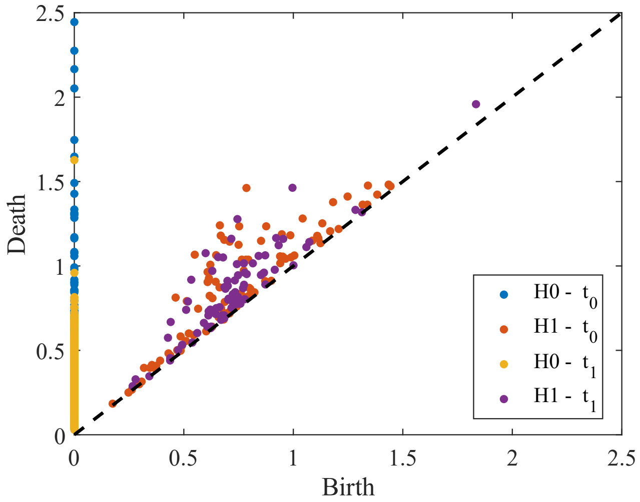

Figure 47. *Persistent diagram comparison between template sourced data and candidate core location at* t_1.

This abstraction serves as a single possible LEV template-target pairing between t_0 and t_1. The intuition is that this feature space pairing can be utilised to quantify the similarity between the LEV at two different instances. To do this, a second ROI of radius r scans over sampling points within the computational domain and computes the persistence diagram. In practice, it is not necessary to scan over every point as this is computationally expensive, and the attached LEV typically remains within one chord length of the aerofoil suction surface. In this work, our interrogation region (IR) is defined with radius, R, and has the same centroid as the template location.

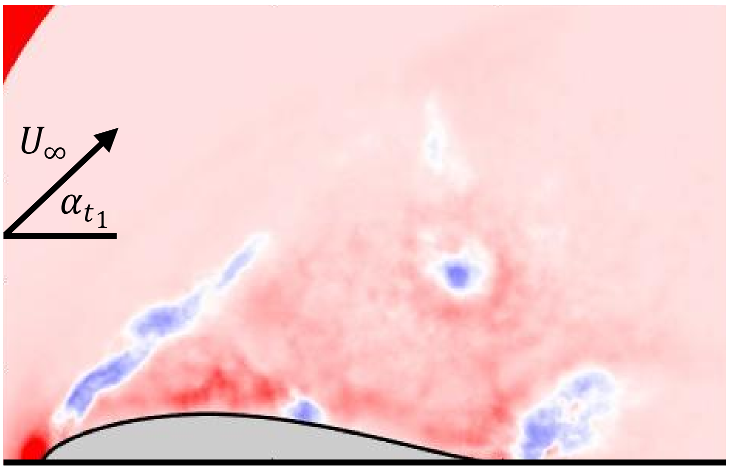

Figure 48. *Template similarity field with set between* $0 \leq W_p \leq 15$.

Grid points outside of R are automatically assigned a maximum distance value to enforce incompatibility. The distance between these two persistence diagrams can be quantified by the Wasserstein distance (Vaserstein, 1969) which is also known as the Earth mover's distance (Agami, 2023). Utilising the persim python library which is based on work by Adams et al.

(2015*)* the Wasserstein distance between two persistence diagrams is computed up to and including a homology dimension, $k = 1$. Mathematically, the p-Wasserstein distance between two persistence diagrams, D_1 and D_2, is given by equation 58 where p is the order of the Wasserstein distance. Here, the default value of $p = 2$ is utilised and φ is a bijection from D_1 to D_2. This operation attempts to find the best possible matching between the birth-death multisets by minimising the L_∞ norm of x and $\varphi(x)$ over all possible bijections.

$$W_p(D_1, D_2) = \left(\inf_{\varphi: D_1 \rightarrow D_2} \sum_{x \epsilon D_1} \left|\left| x - \varphi(x) \right|\right|^p \right)^{1/p} \qquad 58$$

This operation, applied individually to the n^{th} grid point within an IR of N possible candidate locations, generates a template similarity field (TSF) indicating where the template-target distance is lowest at t_1. An example of this is shown in figure 48 where the ROI radius between two arbitrary but successive time steps is set to $r = 0.04c$. The effects of r will be discussed in the following sections. The template-target similarity at t_1 tends to be the highest in regions of high shear or vortex formation as indicated by the blue regions.

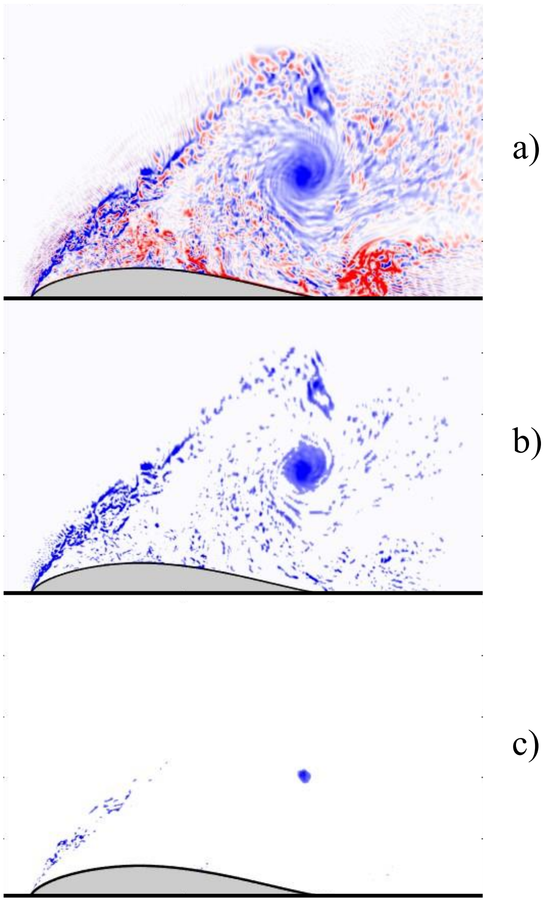

Figure 49. *a) Raw ω_z field with strong LEV present during high amplitude starting cycle. b) ω_z field with threshold applied between $-100 \geq \omega_z \geq -20$. c) TSF weighted ω_z field with threshold applied between $-100 \geq \omega_z \geq -20$.*

Conversely, the red coloured regions indicate template-target dissimilarity which appears to be present in the regions immediately bounding strong fluid shearing or coherence. The highest values of W_p are situated about the leading-edge where vortex elements have not yet wholly formed. Finally, this heatmap is then used to weight the out-of-plane vorticity field, ω_z, at each sampled grid point by equation 59. Here, τ is a small positive number to avoid division by zero.

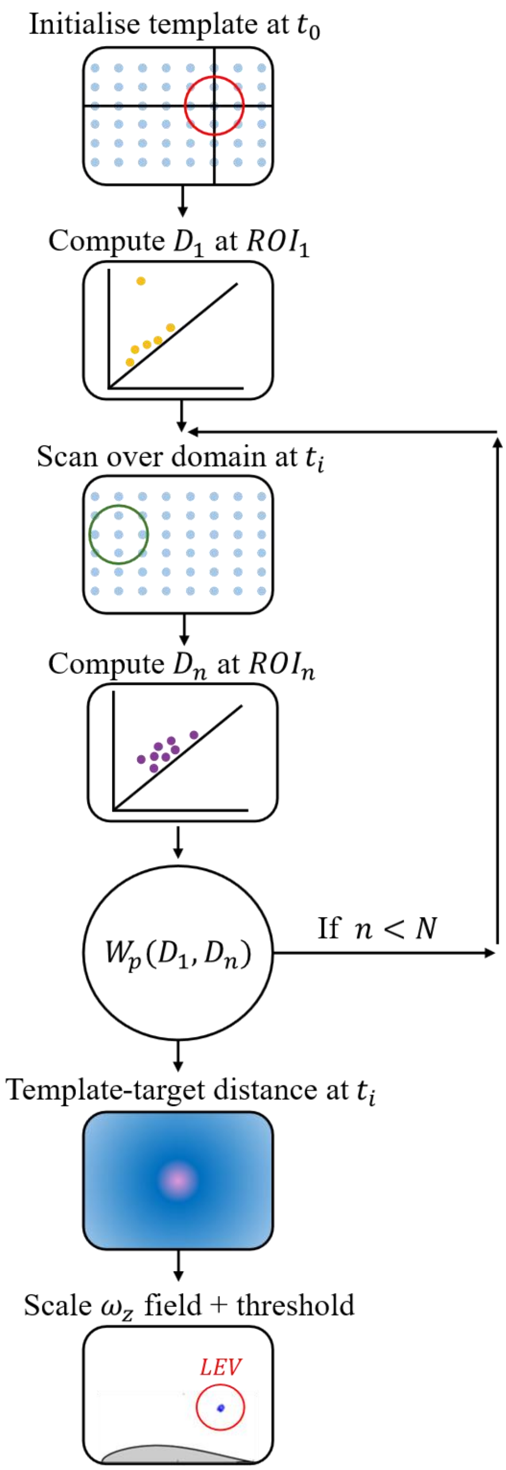

Figure 50. *Persistent homology-based template matching pipeline for LEV core identification.*

This operation acts as both a form of error correction and filtration for regions of template dissimilarity. The LEV core location can be recovered as the local vorticity minimum in the TSF weighted vorticity field via thresholding.

$$\omega_{z,scaled} = \frac{1}{(W \quad \tau)^2} * \omega_z \qquad 59$$

An example of this operation is presented in figure 49, where the TSF is utilised to weight the raw spanwise vorticity field at t_1 (fig. 49a). Figures 49b and 49c represent a visual comparison of the vortex core when the TSF weighting is withheld and applied, respectively. For both figures, a threshold is applied between $-100 \geq \omega_z \geq -20$ to highlight candidate core locations. It can be seen that the vortex core is more clearly depicted in figure 49c as most of the background vorticity is suppressed in regions where the template similarity field has a high Wasserstein distance. A schematic overview of this pipeline is given in figure 50 where additional smoothing, filtering, or thresholding methods can be added as auxiliary support for more precise LEV core identification and tracking.

7.3 Effects of Template Radius

To optimise the application of this methodology within practical workflows, the effects of the template radius are explored. More specifically, r is varied parametrically between $0.02c$ and $0.06c$ to quantify how accurately the TSF is able to discriminate between the LEV core and background noise. For this analysis, the immediate LEV vicinity is only considered such that $R = 0.4c$. Additionally, three successive but non-consecutive timestamps are used to assess the generality of this parametric study for identifying the LEV core. The template vortex used in this study is the same region that was sourced in figure 46 and is referenced as t_0. The manually identified vortex core is set as $x, y = (0.8024c, 0.3509c)$. The IR also has a fixed centroid at this same location. As a preliminary assessment, figure 51 demonstrates the effect of varying the template size between $r = 0.02c$ and $r = 0.06c$ at t_1. For a small template radius, the TSF weighted vorticity field permits a wide distribution of vorticity. This implicates that the manually defined template is insufficient for differentiating between a vortex core and the smaller eddy structures.

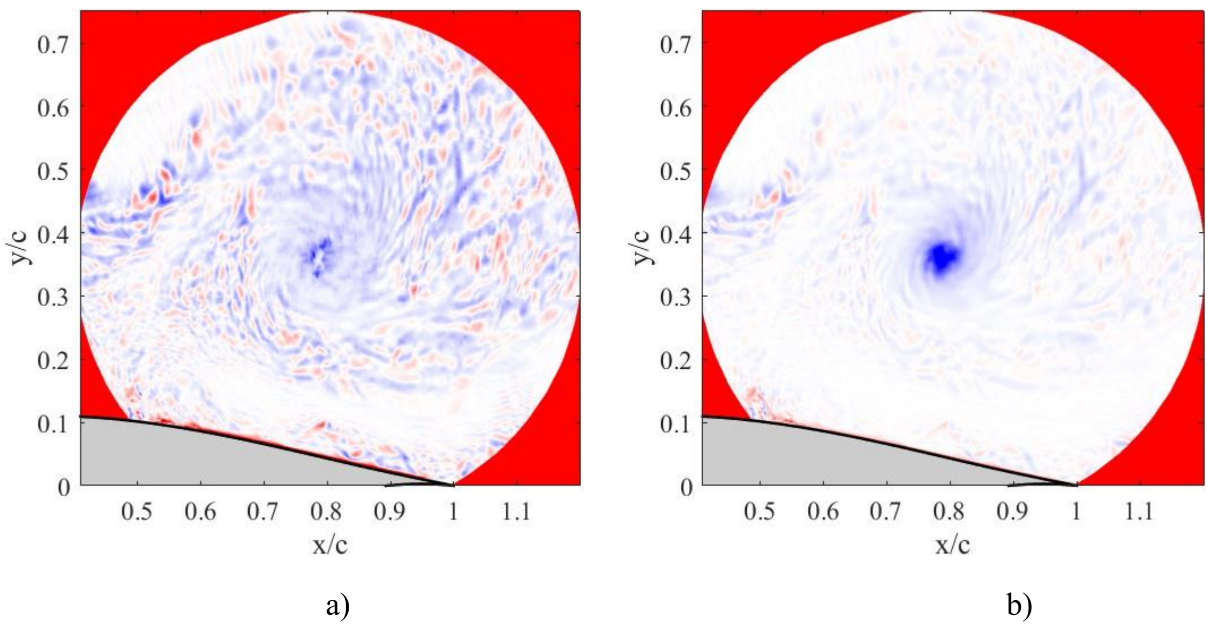

Figure 51. *TSF weighted ω_z field comparison for a) $r = 0.02c$ and b) $r = 0.06c$. Both cases utilise an IR of $R = 0.4c$ and have the range set between $-50 \leq \omega_z \leq 50$.*

As such, the TSF exhibits a large degree of similarity (low Wasserstein distance) that acts to apply an approximately uniform weighting. In contrast, by using a template with $r = 0.06c$, the background vorticity tends to be suppressed. This is due to a high localised dissimilarity in the TSF that accentuates the vortex core. Thus, it can be expected that the scaled vorticity distribution at low radii has a high variance. Conversely, as the ideal template size is approached, the distribution should narrow about zero. To test this supposition, we compute the probability distribution of the TSF weighted vorticity field at three successive timestamps using a logistic distribution fit. The spatial distribution mean, μ, and variance, σ^2, are monitored over the parametric range, $r = [0.02: 0.01: 0.06]$, and utilising the same previously defined template and IR. The results of this study are presented in figure 52 where t_i indicates the successive field snapshots.

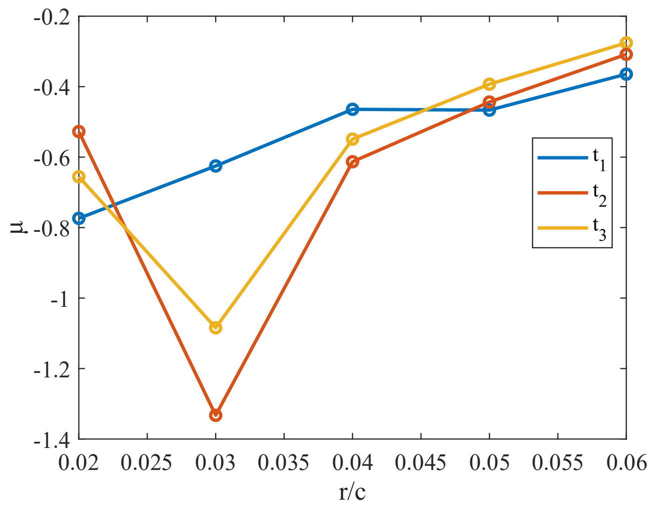

a)

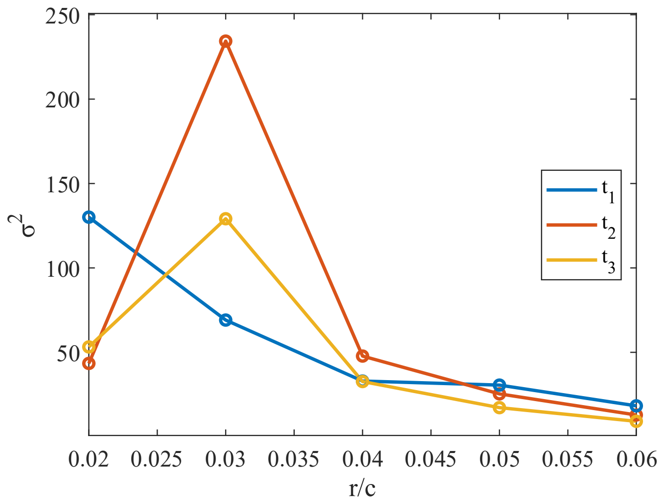

b)

Figure 52. *Template size sensitivity analysis based on the TSF weighted ω_z distribution. a) distribution mean as a function of r. b) distribution variance as a function of r. Different colour plots correspond to the respective distribution at successive timestamps within the pitching cycle.*

As expected, the weighted vorticity distribution tends to approach a mean value, $\mu_{\omega_z} = 0$ when r is varied between $0.02c$ and $0.06c$ across all cases. This is because more of the background eddy structures and noise are being suppressed due to a favourable template-target pairing. The variance also appears to shrink with r as per a larger disparity in vortex core candidate locations and noise. For both metrics, the change in distribution sensitivity appears to decrease dramatically at $r = 0.04c$. Beyond this template radius, the respective distributions between t_1, t_2, and t_3 are closely aligned. An important consideration here, is that the construction of a Vietoris-Rips complex has a complexity of $O(2^n)$ where n is the number of data points sourced within r. Thus, the computational time and memory scaling for an ideal template is exponential in n and constant with the data dimension, R^d (Somasundaram et al., 2021). This potentially incurs significant computational challenges when automating the vortex core tracking in high fidelity simulations or particle image velocimetry (PIV) data. In some cases, the marginal increase in identification accuracy from utilising a larger template radius may not warrant the computational overhead.

7.4 Effects of Down Sampling

To address the computational challenges associated with persistent homology, it is common to apply down sampling to the sourced point-cloud data. While an intuitive strategy to simplify the complex generation and filtration process, this ultimately changes the point-cloud topology and further complicates the feature space template/target 'definition' of a vortex core at each timestamp. A potentially important consideration is how the template/target data is down sampled (uniform, random, directional bias) to account for the vortex shape and spatial distribution. An alternative method is to simply apply down sampling to the prospective template/target ROI centroids as this does not alter its respective point cloud topologies, only the TSF spatial resolution which can be managed easily through spatial interpolation. As such, we consider the effects of a uniform down sampling factor, M, within a fixed IR of $R = 0.3c$ on the vortex core identification.

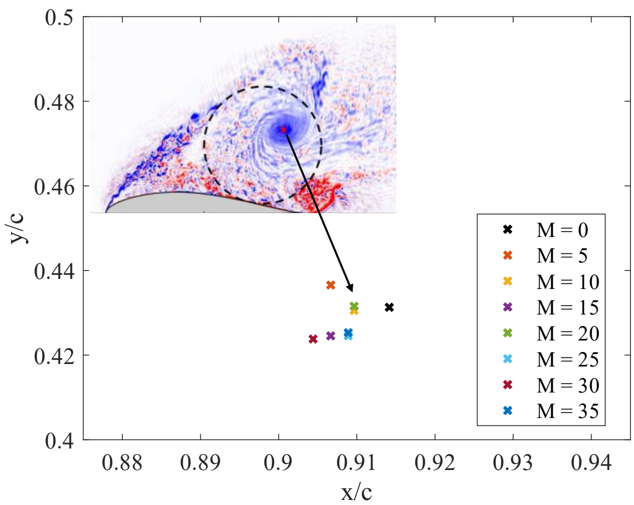

Figure 53. *Vortex core identification varied parametrically by a uniform down sampling factor, M. In all cases, the vortex core is quantified by the global minimum TSF weighted spanwise vorticity within the IR (black dashed boundary).*

For this test, down sampling is applied to the target snapshot by uniformly skipping over candidate centroid locations within the IR. All computations were conducted utilising an Intel i5 processor with 2.40 Ghz and multithreading over four physical cores. The Wasserstein distance at skipped locations is assigned by using a linear interpolation scheme on the unstructured grid. This ensures that the dimension of the TSF and vorticity field are the same. Finally, the vortex core is recovered here as the local minimum weighted vorticity within an IR that is centred by the template centroid location. Figure 53 demonstrates the identified vortex core locations by varying the down sampling factor within the range, $M = [0{:}5{:}35]$. The template used here is defined at $x, y = (0.8024c, 0.3509c)$, with $r = 0.04c$.

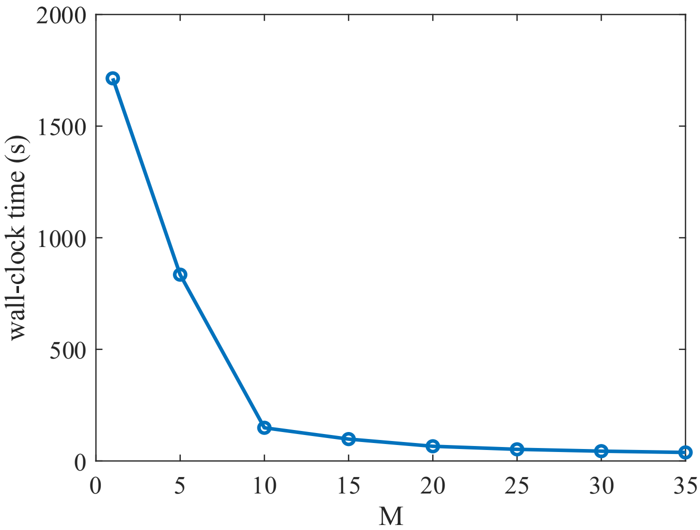

Figure 54. *Wall-clock time as a function of down sampling factor, M. All tests were conducted on a computer utilising an Intel i5 processor with 2.40 Ghz. Grid scanning is parallelised over 4 physical cores.*

It can be seen that the vortex core location is largely insensitive to the effects of down sampling as these predictions are contained within a range of $\pm 0.02c$ from the baseline case, $M = 0$. Though, these predictions tend to exhibit nonlinear behaviour as $M = 10$ and $M = 20$ yield the closest matches to our baseline definition. In general, down sampling appears to offer a significant advantage as the computational cost decreases dramatically when $M \geq 10$ (see figure 54). Furthermore, this advantage incurs a nominal decrease in prediction accuracy making it a suitable practice to implement in this vortex tracking pipeline.

7.5 Leading-Edge Vortex Tracking

Utilising the developed vortex identification pipeline and a template definition with $x, y = (0.8024c, 0.3509c)$, $r = 0.04c$, and $M = 10$, the LEV trajectory is monitored during an aeroelastic starting cycle for a NACA 63(3)418 aerofoil. As a preliminary demonstration, an IR with $R = 1c$ is used to provide a global comparison of the vortex core identification with and without the TSF weighting scheme. For this assessment, four successive but non-consecutive timestamps are considered. Both the TSF weighted and unweighted vorticity fields are computed and limited between $-100 \leq \omega_z \leq -20$. Spatial regions that satisfy this threshold criteria are then clustered together to highlight potential vortex core candidate locations. For figure 55a, conventional thresholding of the raw spanwise vorticity field still yields significant noise at four distinct stages within the LEV lifecycle. This complicates the goal of vortex identification and tracking as there are many possible candidate core locations owing primarily to fluid shear interactions. When the TSF weighting scheme is applied though (fig. 55b), we observe a significant filtration of these spurious vortex core locations.

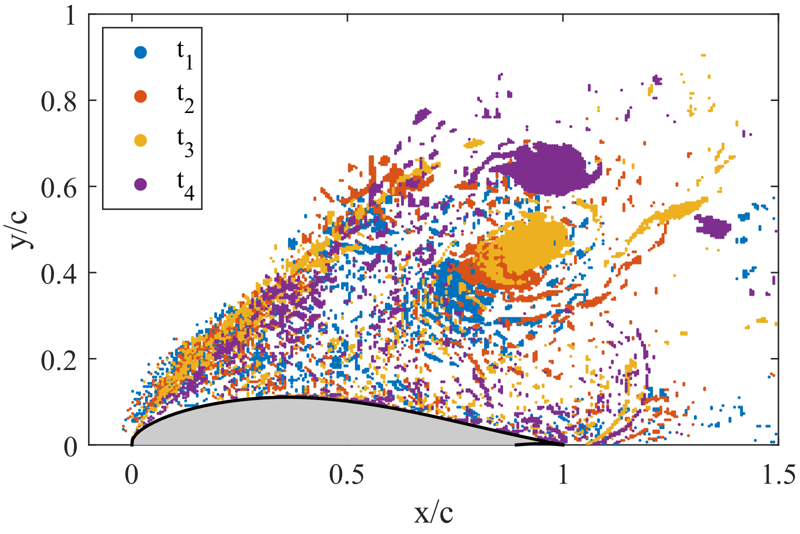

a)

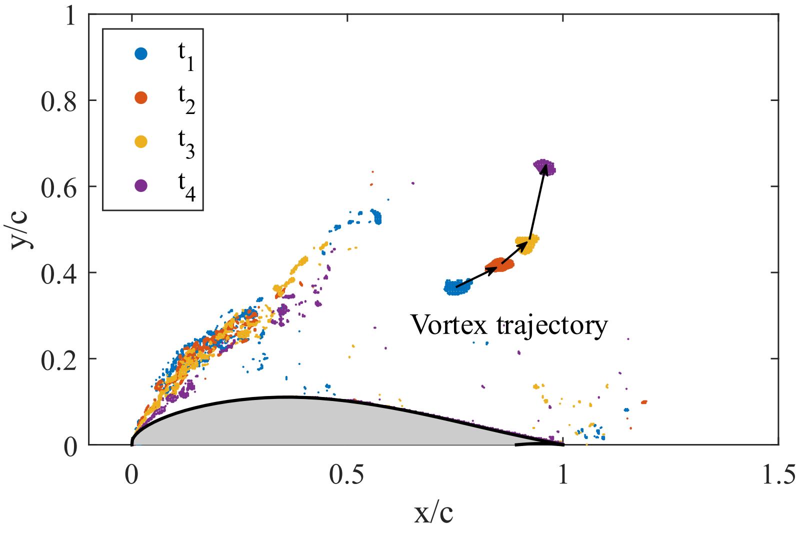

b)

Figure 55. *a) Potential vortex core candidate locations clustered based on an applied threshold,* $-100 \leq \omega_z \leq -20$*, to the raw* ω_z *field. b) Potential vortex core candidate locations clustered based on an applied threshold,* $-100 \leq \omega_z \leq -20$*, to the TSF weighted* ω_z *field. Four successive temporal snapshots are utilised within the first starting cycle.*

The leading-edge shear layer is still present at these timestamps but appears to be largely diminished compared to the conventional thresholding method. Finally, four vortex clusters are easily identifiable when the TSF weighting is applied. It is clear that this method provides an advantage in vortex core identification as it acts to filter out most of the turbulent background noise. This allows for a better qualitative and quantitative interpretation of the LEV dynamics during stall flutter.

To perform automated vortex tracking, an adaptive IR with $R = 0.2c$ is constructed based on the identified vortex core location. More specifically, the IR centroid at t_{i+1} is updated as the vortex core location, (x_c, y_c), at t_i. Figure 56 presents the results of this LEV tracking study where the different trajectory traces correspond to the TSF weighting, local Q-criterion maximum, local spanwise vorticity minimum, local swirling strength maximum, and manual core definition methods respectively. The latter four methods all require user input whereas the blue trace (TSF) is completely automated aside from the template initialisation and first IR assignment. Note that all trajectories were smoothed using a sliding window filter of three timestamps. It can be seen that the TSF based tracking method is quite satisfactory in monitoring the core trajectory during its suction side migration and eventual severance when compared to the local $\omega_{z,min}$, local swirl strength maximum, manual core identification traces. The local Q-criterion maximum trace appears to exhibit stronger variations in the LEV core trajectory, especially in the vicinity leading up to LEV detachment. This suggests that TSF monitoring scheme is less sensitive to localised truncations of the flow field than the Q-criterion for the case study presented here.

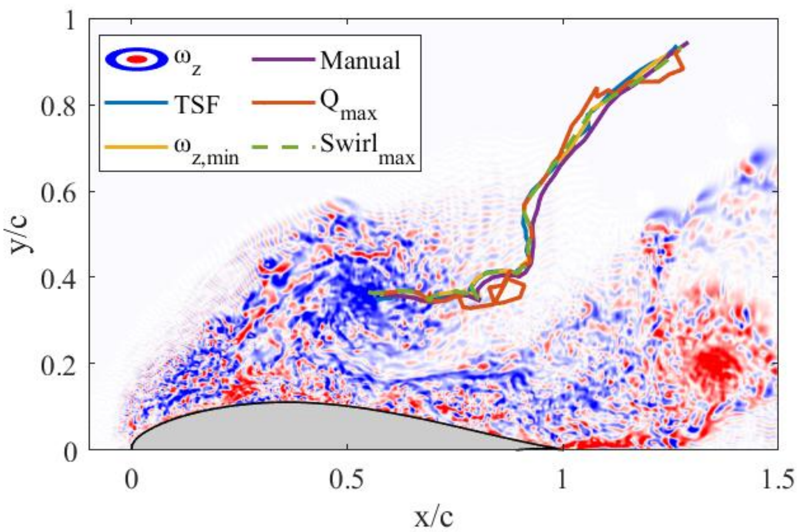

Figure 56. *TSF automated vortex core trajectory (blue) compared with several user-in-the-loop monitoring strategies. Trajectories are computed starting from the vortex state illustrated by the ω_z contour. Contour range is set between $-50 \leq \omega_z \leq 50$.*

Overall, the dynamic stall regime captured by these respective traces generally corresponds to a mature LEV status where the vortex structure is coherent and easily compatible with our chosen template. A distinct changepoint near $\frac{x}{c} = 0.9$ is captured in all trajectories. This trajectory shift away from the aerofoil has been linked to a trailing edge interaction with the LEV that is responsible for the LEV detachment and subsequent dynamic lift stall (Martinez et al., 2025), (Kissing et al., 2020). Thus, accurately identifying this tendency further demonstrates the capability of our method for monitoring the LEV as it progresses through various critical stages of its lifecycle. Overall, the TSF proves to be an effective tool for vortex core identification and monitoring in dynamically stalled flows.

Conclusion

Offshore mega-watt range wind turbines are susceptible to aeroelastic fatigue which can lead to maintenance related downtime and early decommissioning. This outcome can be exaggerated by transient environmental conditions such as gusts, wind shearing, wake, etc. that can potentially excite the aeroelastic response known as stall flutter. This limited amplitude instability is enabled by a complex dynamic stall process that has proven difficult to consolidate into reduced order models. This is particularly true for intra-cycle phenomenon such as the LEV detachment and shedding processes which are significant sources of nonlinearity. A fundamental step change in our understanding how this dynamic stall process evolves in transient pitching cycles is therefore crucial to inform prediction, design, and control efforts that all endeavour to maximise the mechanical lifespan of offshore wind turbines.

In this thesis, we utilised LES to investigate the high amplitude aeroelastic pitching cycles of a NACA 6(3)3418 aerofoil prior to sustained limit cycle oscillations. In this regime, the governing fluid dynamic mechanisms enabling stall flutter are both highly transitory and critically important from the purview of bypass transition, energy growth, and early flutter suppression. We analysed these transient pitching cycles over a wide range of parametric conditions including the reduced frequency, mean incidence angle, and perturbation starting time. We also explored the application of actuated jet blowing for actively attenuating the unsteady load overshoot in these aeroelastic pitching cycles. Overall, several significant contributions were made towards a step-change in our understanding of transient stall flutter dynamics:

The LEV detachment mechanism can transition from invasive to benign when varying the reduced frequency parameter. At low reduced frequencies, a ‘squeezing’ type detachment phenomenon is observed between upstream and downstream secondary structures that limits the LEV development and its motion. We termed this as an invasive detachment mechanism and can occur independently of the aerofoil chord length. Conversely, as the reduced frequency parameter is increased above $K = 0.2$, we observed a more benign LEV detachment mechanism that requires the LEV rear stagnation point to pass over the aerofoil trailing edge. This mechanism is chord dependent and has been previously identified within the fluid dynamic community.

At high mean incidence angles, Kármán vortex shedding has the potential to strongly interact with the transient dynamic stall process. By adjusting the perturbation starting time within the vortex shedding phase, the unsteady aerodynamic loads tend to vary dramatically beyond dynamic lift stall. The mechanism enabling this variability was linked to the status of a TEV that can impede the LEV development and cause early drifting. This impediment was quantified through various measures of the LEV such as its trajectory, induced surface velocity, and shape. By leveraging LAVD, we demonstrated how vortex morphology can be utilised to characterise the status of coherent structures. It was shown that both the LEV eccentricity and aspect ratio variability tends to contract near the point of dynamic lift stall.

Scheduled jet actuation during transient aerofoil pitching motions can significantly affect the dynamic stall process and influence load alleviation. We demonstrated that several high jet orientation angle conditions can fulfil this outcome despite promoting boundary layer separation at static and constant blowing conditions. The mechanism associated with this capability was linked to the formation of a TEV that restricts the LEV motion and causes early detachment. This is identical to the invasive detachment mechanism that was previously documented for low reduced frequency conditions. By means of POD, it was shown that the fourth most energetic mode was responsible for this invasive TEV phenomenon. By exploiting this detachment pathway, jet control authorities can mitigate unsteady lift overshoot through an alternative flow control mechanism. This may be achieved at an injection cost that is lower than what is required to maintain boundary layer attachment throughout the entire pitching cycle.

Owing to the relevance of vortex core tracking in stall flutter/dynamic stall related studies, we developed a robust method for vortex detection based on template matching. Specifically, we mapped high dimensional field data representative of the LEV core to a low dimensional feature space via persistent homology. It was shown that template matching could then be performed using this abstracted LEV definition to monitor the core in successive field snapshots. By incorporating an adaptive search region into this pipeline, we also demonstrated how this topology informed template matching procedure could be leveraged for autonomous LEV monitoring in dynamically stalled flow scenarios. An important benefit of this method compared to current template matching techniques is that persistent homology is both insensitive to noise and invariant to template-target rotations. The primary advantage of utilising this proposed method is that a singular vortex core template is sufficient to label and monitor the LEV core at future timesteps. No user-input is necessary aside from supplying the initial template definition and interrogation region which makes this method extremely user friendly. This also makes the pre-processing requisite quite cheap in comparison to other data driven methodologies exploiting machine vision or deep learning that require a substantial library of training material to generalise an adequate vortex core definition.

In general, these contributions have presented unique insight into how the LEV develops prior to an LCO. Current research paths have primarily focused on the dynamic stall process during either prescribed oscillatory motions or during a sustained instability. While this is informative to map the global stability boundaries of aeroelastic structures, it does not necessarily elucidate how stall flutter is first enabled or how it can be pre-emptively controlled. Our analysis has focused on the LEV structure during these transient pitching cycles to compare how different parametric conditions affect its development. We can conclude that the LEV detachment mechanism accounts for a substantial portion of nonlinearity in the dynamic stall process which translates into load augmentation variability and energy extraction/dissipation potential. As such, altering this phenomenology either through inherent structural characteristics (stiffness, moment of inertia, etc.) or control authorities (jet-blowing) can help mitigate unwanted aerodynamic loading during transient environmental conditions. We demonstrated that promoting the LEV detachment by severing its source vorticity or limiting its chordwise path are clear mechanisms to limit load augmentation. While this thesis does not introduce an optimal parametric arrangement for load alleviation, we have documented and described in detail several mechanisms that encourage LEV detachment. The most significant example being the application of actuated blowing for inducing an invasive TEV structure. While this structure has been identified in previous numerical and experimental campaigns, we have provided a unique phenomenological diagnosis of how this structure interferes with the LEV development and promotes early detachment. To the best of our knowledge, the utility of this invasive detachment pathway has not been thoroughly explored as a mechanism for unsteady aerodynamic load alleviation. Finally, our vortex tracking methodology can be useful to accurately to assess how these types of parametric influences alter the LEV dynamics in either favourable or unfavourable scenarios. While this method allows for simplified automation in general vortex tracking related studies, it showed a particular adequacy for dynamically stalled flow scenarios.

Beyond these immediate contributions, we expect this work to form a basis for future research regarding stall flutter in fatigue susceptible structures. One potential route is to further explore the non-repeatability of transient dynamic stall processes at high mean incidence angles which can give rise to a wide distribution of aerodynamic responses. As such, it may be expected that the necessary perturbation energy to achieve subcritical bypass transition follows an analogous distribution. While this consensus is purely speculative at this point, it provides a potential route for understanding the stability criteria associated with susceptible aeroelastic structures like wind turbine blades. A second possible extension of this work is to determine a set of optimal jet actuation parameters that lead to unsteady aerodynamic load alleviation whilst exploiting the invasive detachment mechanism. This would necessitate an investigation into the ideal TEV formation criteria. Finally, a natural extension of our vortex identification pipeline would be to incorporate it into a machine learning based framework for automating multi-vortex core tracking. One method for doing this would simply be to assign vortex labels via the produced TSF. Another could be to consolidate persistent homology into the loss function directly via the Wasserstein distance.

References

Adams, H., Chepushtanova, S., Emerson, T., Hanson, E., Kirby, M., Motta, F., Neville, R., Peterson, C., Shipman, P. & Ziegelmeier, L. (2015) ‘Persistence images: a stable vector representation of persistent homology’, arXiv:1507.06217 [Preprint]. doi:10.48550/arXiv.1507.06217. Available at: https://arxiv.org/abs/1507.06217.

Agami, S. (2023) ‘Comparison of persistence diagrams’, Communications in Statistics - Simulation and Computation, 52(5), pp.1948–1961. doi:10.1080/03610918.2021.1894335.

Althaus, D. (1995) ‘Aerofoils and Experimental Results from the Laminar Wind Tunnel of the Institut für Aerodynamik und Gasdynamik der Universität Stuttgart’, IAG Stuttgart.

Allen, H.J. and Vincenti, W.G. (1944) ‘Wall interference in a two dimensional flow wind tunnel, with consideration of the effect of compressibility’, NACA Technical Report 782. National Advisory Committee for Aeronautics. Available at: https://ntrs.nasa.gov/citations/19930091861

Bak, C., Olsen, A.S., Fischer, A., Lylloff, O., Mikkelsen, R., Gaunaa, M., Beckerlee, J., Ildvedsen, S., Vronsky, T., Grasso, F., Loeven, A., Broersma, L., Akay, B., Madsen, J., Hansen, R., and Kommer, R. (2022) ‘Wind tunnel benchmark tests of aerofoils’, Journal of Physics: Conference Series, 2265(2), Article 022097. doi:10.1088/1742 6596/2265/2/022097

Bauer, U. (2021) ‘Ripser: efficient computation of Vietoris–Rips persistence barcodes’, Journal of Applied and Computational Topology, 5(3), pp.391–423. doi:10.1007/s41468 021 00071 5.

Bollay, W. and Brown, C.D. (1941) ‘Some experimental results on wing flutter’, Journal of the Aeronautical Sciences’, 8(8), pp.313–318. https://doi.org/10.2514/8.10724

Bozeman, J.R. and Pilling, M. (2013) ‘The convexity ratio and applications’, Scientiae Mathematicae Japonicae, 76(1), pp. 47–53. https://doi.org/10.32219/isms.76.1_47

Carta, F.O. and Niebanck, C.F., (1969). ‘Prediction of rotor instability at high forward speeds’, Volume III: Stall flutter. Fort Eustis, VA: U.S. Army Aviation Materiel Laboratories (USAAVLABS Technical Report 68-18C)

Carr, L.W., McAlister, K.W. and McCroskey, W.J. (1977) ‘Analysis of the development of dynamic stall based on oscillating aerofoil experiments’, Washington, DC: National Aeronautics and Space Administration. (NASA Technical Note NASA-TN-D-8382)

Cevasco, D., Koukoura, S. and Kolios, A.G.A. (2021) ‘Reliability, availability, maintainability data review for the identification of trends in offshore wind energy applications’, Renewable and Sustainable Energy Reviews, 136, 110414. https://doi.org/10.1016/j.rser.2020.110414

Chang, J., Zhang, Q., He, L. and Zhou, Y. (2022) ‘Shedding vortex characteristics analysis of NACA 0012 airfoil at low Reynolds numbers’, Energy Reports, 8, pp. 156–174. https://doi.org/10.1016/j.egyr.2022.01.149

Chen, Z., Shi, Z., Chen, S. and Yao, Z. (2022) ‘Stall flutter suppression of NACA 0012 aerofoil based on steady blowing’, Journal of Fluids and Structures, 109, article 103472. https://doi.org/10.1016/j.jfluidstructs.2021.103472

Chorin, A.J. (1968) ‘Numerical solution of the Navier–Stokes equations’, Mathematics of Computation, 22(104), pp.745–762. https://doi.org/10.2307/2004575

Culler, E.C.E. and Farnsworth, J.A.N. (2019) ‘Higher frequencies in stall flutter moment development’, Journal of Fluids and Structures, 85, pp. 181–198. https://doi.org/10.1016/j.jfluidstructs.2019.01.007

Damiola, L., Runacres, M.C. and De Troyer, T., (2024) ‘The challenge of cycle-to-cycle variability in dynamic stall modelling’, Journal of Physics: Conference Series, 2767(5), 052007. https://doi.org/10.1088/1742-6596/2767/5/052007

Dimitriadis, G. and Li, J. (2009) ‘Bifurcation behavior of an aerofoil undergoing stall flutter oscillations in a low-speed wind tunnel’, AIAA Journal, 47(11), pp.2577–2596. https://doi.org/10.2514/1.39571

Doligalski, T.L., Smith, C.R. and Walker, J.D.A., (1994) ‘Vortex interactions with walls. Annual Review of Fluid Mechanics’, 26(1), pp.573–616. https://doi.org/10.1146/annurev.fl.26.010194.003041

Edelsbrunner, H., Letscher, D. & Zomorodian, A. (2002) ‘Topological persistence and simplification’, Discrete & Computational Geometry, 28(4), pp.511–533. doi:10.1007/s00454 002 2885 2

Erkan, O., Özkan, M., Karakoç, T.H., Garrett, S.J. and Thomas, P.J. (2020) ‘Investigation of aerodynamic performance characteristics of a wind turbine blade profile using the finite volume method’, Renewable Energy, 161, pp.1359–1367. https://doi.org/10.1016/j.renene.2020.07.138

Fernandez, F., Cleaver, D. and Gursul, I. (2021) ‘Unsteady aerodynamics of a wing in a novel small amplitude transverse gust generator’, Experiments in Fluids, 62(9). doi:10.1007/s00348 020 03100 8

Ferziger, J.H. and Perić, M. (2002) ‘Computational methods for fluid dynamics’, 3rd edn. Berlin: Springer. https://doi.org/10.1007/978-3-642-56026-2

Feszty, D., Gillies, E.A. and Vezza, M. (2004) ‘Alleviation of aerofoil dynamic stall moments via trailing edge flap flow control’, AIAA Journal, 42(1), pp.17–25. doi:10.2514/1.853

Foss, J.F. (2004) ‘Surface selections and topological constraint evaluations for flow field analyses’, Experiments in Fluids, 37(6), pp.883–898. doi:10.1007/s00348 004 0877 0

Gardner, A.D., Jones, A.R., Mulleners, K., Naughton, J.W. and Smith, M.J. (2023) ‘Review of rotating wing dynamic stall: Experiments and flow control’, Progress in Aerospace Sciences, 137, 100887. https://doi.org/10.1016/j.paerosci.2023.100887

Haller, G., Hadjighasem, A., Farazmand, M. & Huhn, F. (2016) ‘Defining coherent vortices objectively from the vorticity’, Journal of Fluid Mechanics, 795, pp.136–173. doi:10.1017/jfm.2016.151

Horn, J.T. and Leira, B.J. (2019) ‘Fatigue reliability assessment of offshore wind turbines with stochastic availability’, Reliability Engineering & System Safety, 191, 106550. https://doi.org/10.1016/j.ress.2019.106550

Hunt, J.C.R., Abell, C.J., Peterka, J.A. and Woo, H. (1978) ‘Kinematical studies of the flows around free or surface mounted obstacles; applying topology to flow visualization’, Journal of Fluid Mechanics, 86(1), pp.179–200. doi:10.1017/S0022112078001068

Ibáñez, C., Migliorini, M., Giannouloudis, A., Tejero, F. & Zachos, P.K. (2025) ‘Cluster based tracking method for the identification and characterisation of vortices’, in Proceedings of the 59th 3AF International Conference on Applied Aerodynamics, Strasbourg, France, 24–26 March 2025. Available at: https://www.researchgate.net/publication/391008385_Cluster-Based_Tracking_Method_for_the_Identification_and_Characterisation_of_Vortices

Jain, S. and Saha, U.K., 2020. ‘On the influence of blade thickness to chord ratio on dynamic stall phenomenon in H type Darrieus wind rotors’, Energy Conversion and Management, 218, 113024. https://doi.org/10.1016/j.enconman.2020.113024

Kern, J.S., Blanco, D.C.P., Cavalieri, A.V.G., Negi, P.S., Hanifi, A. and Henningson, D.S. (2024) ‘Direct numerical simulations of an aerofoil undergoing dynamic stall at different background disturbance levels’, Journal of Fluid Mechanics, 986, A3. https://doi.org/10.1017/jfm.2024.314

Kim, J. and Moin, P. (1985) ‘Application of a fractional-step method to incompressible Navier–Stokes equations’, Journal of Computational Physics, 59(2), pp.308–323. https://doi.org/10.1016/0021-9991(85)90148-2

Kim, J., Park, Y.M., Lee, J., Kim, T., Kim, M., Lim, J. and Jee, S. (2019) ‘Numerical investigation of jet angle effect on aerofoil stall control’, Applied Sciences, 9(15), article 2960. https://doi.org/10.3390/app9152960

Kim, T. and Jee, S., 2023. ‘Numerical investigation of impulsively generated high-speed jet for dynamic stall suppression’. Computers & Fluids, 251, p.105757. https://doi.org/10.1016/j.compfluid.2022.105757

Kissing, J., Kriegseis, J., Li, Z., Feng, L., Hussong, J. and Tropea, C., (2020), ‘Insights into leading edge vortex formation and detachment on a pitching and plunging flat plate’, Experiments in Fluids, 61(9), 208. https://doi.org/10.1007/s00348-020-03034-1

Küppers, J.P. and Reinicke, T., (2022), ‘A WaveNet based fully stochastic dynamic stall model’, Wind Energy Science, 7, pp.1889–1903. https://doi.org/10.5194/wes-7-1889-2022

Lee, H., Simone, N., Su, Y., Zhu, Y., Ribeiro, B.L.R., Franck, J.A. and Breuer, K., (2022), ‘Leading edge vortex formation and wake trajectory: Synthesizing measurements, analysis, and machine learning’, Physical Review Fluids, 7(7), 074704. https://doi.org/10.1103/PhysRevFluids.7.074704

Li, Z.-Y., Feng, L.-H., Kissing, J., Tropea, C. and Wang, J.-J., (2020), ‘Experimental investigation on the leading-edge vortex formation and detachment mechanism of a pitching and plunging plate’, Journal of Fluid Mechanics, 901, A17. https://doi.org/10.1017/jfm.2020.509

Matalanis, C.G., Bowles, P.O., Min, B.-Y., Jee, S., Kuczek, A.E., Wake, B.E., Lorber, P.F., Crittenden, T.M., Glezer, A. and Schaeffler, N.W., (2017), 'High-speed experiments on combustion-powered actuation for dynamic stall suppression', AIAA Journal, 55(9), pp.3001–3015. https://doi.org/10.2514/1.J055700

Martinez, Q., Omidyeganeh, M., Jagadeesh, C. & Manolesos, M. (2025) 'Large Eddy Simulations of an Aerofoil Undergoing One Shot Starting Cycles at Highly Unsteady Condition', Proceedings of the 59th 3AF International Conference on Applied Aerodynamics, Nantes, France, April 2025. doi:10.60711/AERO2025.20250402.8753383450051228

Martinez, Q., Omidyeganeh, M., Jagadeesh, C. and Manolesos, M. (2026), 'Transient development of the leading-edge vortex and its role in unsteady aerodynamic load variations', Physics of Fluids, 38(1), 017139. https://doi.org/10.1063/5.0310207

Mendelson, A. (1948), 'Effect of aerodynamic hysteresis on critical flutter speed at stall', NACA-RM-E8B04. Available at: https://ntrs.nasa.gov/citations/19930085553

Menon, K. and Mittal, R., (2019), 'Flow physics and dynamics of flow-induced pitch oscillations of an aerofoil. Journal of Fluid Mechanics', 877, pp.582–613. https://doi.org/10.1017/jfm.2019.627

Mulleners, K., Raffel, M. (2012), 'The onset of dynamic stall revisited', Exp Fluids 52, 779–793. https://doi.org/10.1007/s00348-011-1118-y

Mulleners, K. and Raffel, M., (2013), 'Dynamic stall development', Experiments in Fluids, 54(2), pp.1469–1477. https://doi.org/10.1007/s00348-013-1469-7

Müller-Vahl, H.F., Strangfeld, C., Nayeri, C.N., Paschereit, C.O. and Greenblatt, D. (2015), 'Control of thick aerofoil, deep dynamic stall using steady blowing', AIAA Journal, 53(2), pp. 277–295. https://doi.org/10.2514/1.J053090

Müller-Vahl, H. F., Nayeri, C. N., Paschereit, C. O. & Greenblatt, D., (2016), 'Dynamic stall control via adaptive blowing', Renewable Energy, 97, pp.47–64. doi:10.1016/j.renene.2016.05.053

Muzaferija, S. (1994) 'Adaptive finite volume method for flow prediction using unstructured meshes and multigrid approach', PhD thesis. London: Imperial College London (University of London). Available at: http://hdl.handle.net/10044/1/7728

Negi, P.S., Vinuesa, R., Hanifi, A., Schlatter, P. and Henningson, D.S. (2018), 'Unsteady aerodynamic effects in small-amplitude pitch oscillations of an aerofoil', International Journal of Heat and Fluid Flow, 71, pp. 378–391. https://doi.org/10.1016/j.ijheatfluidflow.2018.04.009

Nicholas, S. (2022), 'High fidelity simulation of turbulent flows over filamentous surfaces', Unpublished PhD thesis. London: City, University of London. Available at: https://openaccess.city.ac.uk/id/eprint/29198/

Nicholas, S., Omidyeganeh, M. and Pinelli, A. (2022), 'Numerical Investigation of Regime Transition in Canopy Flows', Flow, Turbulence and Combustion, 109, pp. 1133–1153. https://doi.org/10.1007/s10494-022-00363-5

Nikoueeyan, P. and Naughton, J.W. (2023) ‘Analysis of the unsteady surface pressure distribution of a pitching airfoil using modal decomposition’, Experiments in Fluids, 64(5), p. 100. https://doi.org/10.1007/s00348-023-03644-5

Ohmi, K. et al. (1991) ‘Further experiments on Vortex Formation around an oscillating and translating airfoil at large incidences’, Journal of Fluid Mechanics, 225, pp. 607–630. doi:10.1017/s0022112091002197.

Perić, M., Kessler, R. and Scheuerer, G. (1988) ‘Comparison of finite-volume numerical methods with staggered and colocated grids’, Computers & Fluids, 16(4), pp. 389–403. https://doi.org/10.1016/0045-7930(88)90024-2

Perry, A.E. and Fairlie, B.D. (1975) 'Critical Points in Flow Patterns', Advances in Geophysics, 18(Part B), pp. 299–315. https://doi.org/10.1016/S0065-2687(08)60588-9

Piomelli, U., Rouhi, A. and Geurts, B.J. (2015), ‘A grid-independent length scale for large-eddy simulations’, Journal of Fluid Mechanics, 766, pp. 499–527. https://doi.org/10.1017/jfm.2015.29

Prangemeier, T., Rival, D. and Tropea, C., (2010), ‘The manipulation of trailing-edge vortices for an aerofoil in plunging motion’, Journal of Fluids and Structures, 26(2), pp.193–204. https://doi.org/10.1016/j.jfluidstructs.2009.10.003

Rhie, C.M. and Chow, W.L. (1983) ‘Numerical study of the turbulent flow past an aerofoil with trailing edge separation’, AIAA Journal, 21(11), pp. 1525–1532. https://doi.org/10.2514/3.8284

Rival, D.E., Kriegseis, J., Schaub, P., Widmann, A. and Tropea, C., (2014), ‘Characteristic length scales for vortex detachment on plunging profiles with varying leading-edge geometry’, Experiments in Fluids, 55(1), 1660. https://doi.org/10.1007/s00348-013-1660-x

Rosti, M. (2016), ‘Direct numerical simulation of an aerofoil at high angle of attack and its control’, Unpublished PhD thesis. London: City, University of London. Available at: https://openaccess.city.ac.uk/id/eprint/15843/

Sakoe, H. and Chiba, S., (1978), ‘Dynamic programming algorithm optimization for spoken word recognition’, IEEE Transactions on Acoustics, Speech and Signal Processing, 26(1), pp.43–49. https://doi.org/10.1109/TASSP.1978.1163055

Schmid, P.J. and de Langre, E. (2003), ‘Transient growth before coupled-mode flutter’, Journal of Applied Mechanics, 70(6), pp. 894–901. doi:10.1115/1.1631591

Schwartz, M., Manzoor, S., Hémon, P. and de Langre, E. (2009), ‘By-pass transition to aerofoil flutter by transient growth due to gust impulse’, Journal of Fluids and Structures, 25, pp. 1272–1281. doi:10.1016/j.jfluidstructs.2009.08.001

Seidel, J., Fagley, C.P. and McLaughlin, T.E. (2015), ‘Computations of active open-loop flow control on a fluttering wing’, 33rd AIAA Applied Aerodynamics Conference, AIAA Paper 2015-2730, Dallas, TX, 23 June 2015. https://doi.org/10.2514/6.2015-2730

Smith, L., Fukami, K., Sedky, G., Jones, A.R. & Taira, K. (2024), 'A cyclic perspective on transient gust encounters through the lens of persistent homology', Journal of Fluid Mechanics, 980, Article A18. doi: 10.1017/jfm.2024.16.

Somasundaram, E.V., Brown, S.E., Litzler, A., Scott, J.G. & Wadhwa, R.R. (2021), 'Benchmarking R packages for Calculation of Persistent Homology', The R Journal, 13(1), pp. 184–193. doi: 10.32614/RJ-2021-033

Soto-Valle, R., Cioni, S., Bartholomay, S., Manolesos, M., Nayeri, C.N., Bianchini, A. and Paschereit, C.O. (2022), 'Vortex identification methods applied to wind turbine tip vortices', Wind Energy Science, 7, pp. 585–602. doi: 10.5194/wes-7-585-2022

Studer, H.L., (1936), 'Experimental investigation of wing flutter (Translation by WJ Stern.)', ARC, 277.

Tavner, P.J., Greenwood, D.M., Whittle, M.W.G., Gindele, R., Faulstich, S. and Hahn, B. (2013), 'Study of weather and location effects on wind turbine failure rates', Wind Energy, 16(2), pp. 175–187. https://doi.org/10.1002/we.538

Timmer, W.A. (2009), 'An overview of NACA 6-digit aerofoil series characteristics with reference to aerofoils for large wind turbine blades', 47th AIAA Aerospace Sciences Meeting including the New Horizons Forum and Aerospace Exposition, Orlando, Florida, USA, 5–8 January 2009. AIAA Paper 2009-268. https://doi.org/10.2514/6.2009-268

Towne, M.C. and Buter, T. (1994), 'Numerical simulation of dynamic-stall suppression by tangential blowing', 32nd Aerospace Sciences Meeting and Exhibit, American Institute of Aeronautics and Astronautics (AIAA) Paper 1994-184, Reno, NV, 10–13 January 1994. https://doi.org/10.2514/6.1994-184

Tseng, C.-C. and Cheng, Y.-E., (2015), 'Numerical investigations of the vortex interactions for a flow over a pitching foil at different stage', Journal of Fluids and Structures, 58, pp.291–318. https://doi.org/10.1016/j.jfluidstructs.2015.08.002

Valls Badia, P., Hickel, S., Scarano, F. and Li, M. (2025), 'Dynamic stall on airfoils with leading-edge tubercles', Experiments in Fluids, 66(3), 56. https://doi.org/10.1007/s00348-025-03981-7.

Vaserstein, L.N. (1969) 'Markov processes over denumerable products of spaces, describing large systems of automata', Problems of Information Transmission, 5(3), pp. 47–52

Victory, M. (1943), 'Flutter at high incidence', Reports and Memoranda No. 2048, Aeronautical Research Committee.

Villalpando, F., Reggio, M. and Ilinca, A. (2012), 'Numerical study of flow around iced wind turbine aerofoil', Engineering Applications of Computational Fluid Mechanics, 6(1), pp. 39–45. https://doi.org/10.1080/19942060.2012.11015401.

Wang, L., Alam, M.M., Rehman, S. and Zhou, Y. (2022) 'Effects of blowing and suction jets on the aerodynamic performance of wind turbine airfoil', Renewable Energy, **196**, pp. 52–64. https://doi.org/10.1016/j.renene.2022.06.126.

Wang, T. and Feng, L. (2025), ‘Gust alleviation strategy and mechanism for an aerofoil encountering periodical vertical gusts’, Physical Review Fluids, 10(6), p. 064902. doi:10.1103/PhysRevFluids.10.064902.

Watrin, D., Perry, T., Smith, M. and Dimitriadis, G. (2012) Computational Considerations for the Prediction of Stall Flutter. In: Proceedings of the 53rd AIAA/ASME/ASCE/AHS/ASC Structures, Structural Dynamics and Materials Conference, Honolulu, Hawaii, USA, 23–26 April 2012. Reston, VA: American Institute of Aeronautics and Astronautics, Paper AIAA 2012-1706

Weaver, D., McAlister, K.W. and Tso, J. (2004**),** ‘Control of VR-7 dynamic stall by strong steady blowing’, Journal of Aircraft, 41(6), pp. 1404–1413. doi:10.2514/1.4413.

Xing, S.-L., Xu, H.-Y. and Zhang, W.-G. (2022), ‘Trailing edge flap effects on dynamic stall vortex and unsteady aerodynamic forces on a pitching aerofoil’, International Journal of Aerospace Engineering, 2022, Article ID 1674074. https://doi.org/10.1155/2022/1674074

Xu, Z., Maria, A., Chelli, K., Dumouchel De Premare, T., Bilbao, X., Petit, C., Zoumboulis-Airey, R., Moulitsas, I., Teschner, T., Asif, S. & Li, J. (2023), ‘Vortex and core detection using computer vision and machine learning methods’, European Journal of Computational Mechanics, 32(5), pp. 467–494. doi: 10.13052/ejcm2642-2085.3252.

Yarusevych, S., Sullivan, P.E. and Kawall, J.G. (2009) ‘On vortex shedding from an airfoil in low-Reynolds-number flows’, Journal of Fluid Mechanics, 632, pp. 245–271. doi:10.1017/S0022112009007058.

Yousefi, K. and Saleh, R. (2014), ‘The effects of trailing edge blowing on aerodynamics characteristics of the NACA 0012 airfoil and optimization of the blowing slot geometry’, Journal of Theoretical and Applied Mechanics, 52, 165-179. ISSN 1429-2955. Available at: https://www.ptmts.org.pl/jtam/index.php/jtam/article/view/v52n1p165/1821.

Zhu, C. et al. (2023) ‘Effects of the Reynolds number and reduced frequency on the aerodynamic performance and dynamic stall behaviors of a vertical axis wind turbine’, Energy Conversion and Management, 293, p. 117513. doi:10.1016/j.enconman.2023.117513.

Zolghadr, B. and Khoshnevis, A.B. (2024), ‘Numerical study of dynamic stall effects on VR-12 airfoil with pitch oscillation and accelerated inflow’, Energy Science & Engineering, **12**(10), pp. 4478–4511. Available at: https://doi.org/10.1002/ese3.1896

Appendix A

A.1 Persistent Homology

In the field of topological data analysis, persistent homology is a tool for identifying the homology groups in a multivariate point cloud (Edelsbrunner et al., 2002) (Smith et al., 2024). This allows for a diagnosis of the data 'shape' that can be useful for modelling, classification, or segmentation purposes. This abstraction can be understood graphically through a persistence diagram which is constructed by monitoring the persistence, $p = birth - death$, of underlying topological features in the point cloud while varying the filtration level, ϵ. More rigorously, persistent homology is formulated using simplicial complexes. A simplicial complex is a collection of k-simplices such as vertices (0-simplices), edges (1-simplices), triangles (2-simplices), and their higher-dimensional analogues that are connected along shared faces. k-cycles, which are the subcomponents of this simplicial complex forming undirected closed loops, can be grouped into equivalence classes called homology groups. These homology groups formalize the number of holes in a given dimension of the complex by equation 60, where Z_k is the number of k-cycles and and $im(\partial_{k+1})$ denotes the image of the boundary operator.

$$H_k = \frac{Z_k}{im(\partial_{k+1})} \qquad 60$$

In other words, H_k encodes the essential k-dimensional features of the simplicial complex by counting cycles that are not themselves boundaries of higher-dimensional simplices. Persistent homology applies this framework to point cloud data by building a nested sequence of simplicial complexes (filtration) indexed by a scale parameter and by tracking when elements of H_k appear (birth) and disappear (death). Here, an example of this construction is given canonically for the case of 2D point-cloud with noise.

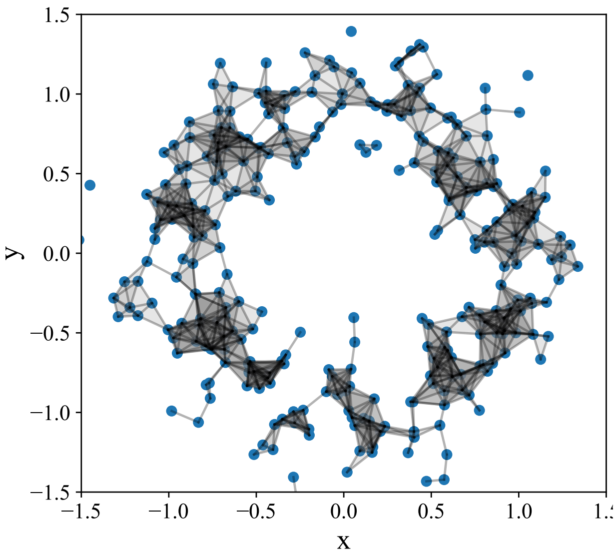

Figure 57. *Vietoris-Rips complex for 2D circular point cloud with noise at filtration level,* $\epsilon = 0.2$.

First, a Vietoris-Rips complex is built using the Ripser Python library (Bauer, 2021). This procedure consists of initialising spheres of radius ϵ at each vertex in the point cloud. These spheres gradually grow, allowing for intersections with neighbouring spheres. The intersection of two spheres forms an edge between them. More generally, for k 1 intersecting spheres, a k-dimensional simplex is formed between the corresponding vertices. A representation of the Vietoris-Rips complex is shown in figure 57 to demonstrate the vertex connectivity at an arbitrary filtration level, $\epsilon = 0.2$,.

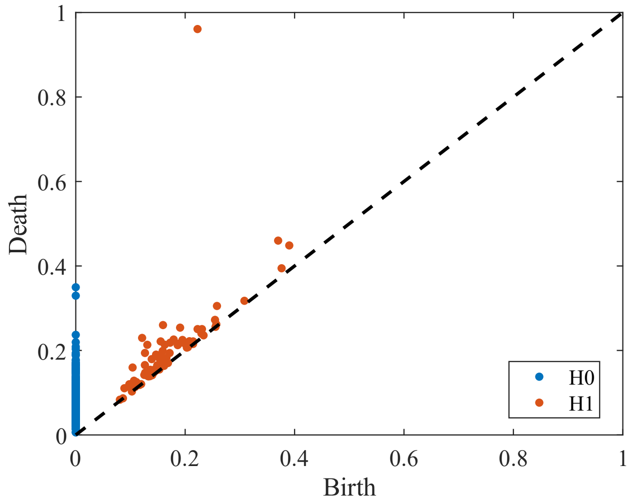

Figure 58. *Persistence diagram for point cloud data in figure 57 up to and including homology dimension* $k = 1$.

At each filtration level, ϵ_i, the homology groups H_k are computed for the corresponding complex K_ϵ. The persistence of these homology groups is monitored as birth/death coordinate pairs and plotted as a diagram to indicate long-lived k-dimensional holes within the data set. This is shown in figure 58 corresponding to the point cloud data in figure 57. In this case, a highly persistent 1-dimensional hole or loop exists within the data set as indicated by the isolated $H1$ data point. This point implicates that a loop is born at a filtration level, $\epsilon = 0.22$ and dies at $\epsilon = 0.96$ which is the longest-lived feature in this 2D point cloud. This example serves as a simplified demonstration of persistent homology but follows the same intuition when dealing with high dimensional data associated with CFD simulations.

A.2 Vortex Identification Pseudocode

```
BEGIN

LOAD CFD snapshot data

//→ Step 1: Build template
SELECT known vortex region (template centre + radius)
EXTRACT points inside this region
COMPUTE persistent homology of template region
STORE template persistence diagram

//→ Step 2: Search for similarity
DEFINE larger search region (guess centre + radius)

FOR each candidate point in search region:

DEFINE local region around candidate point
EXTRACT points within template radius

IF region has enough points:

   COMPUTE persistent homology of this region

   SELECT diagrams homology dimension

   COMPUTE distance between:
      candidate diagram AND template diagram
      (Wasserstein distance)

   STORE (x, y, distance)

END IF

END FOR

//→ Step 3: Build similarity field
INTERPOLATE distances over entire search region

//→ Step 4: Identify vortex core
COMPUTE distance weighted vorticity field
FIND location where distance is MINIMUM
RETURN location as most similar (vortex core candidate)

END
```

A.3 Jet Actuation Data

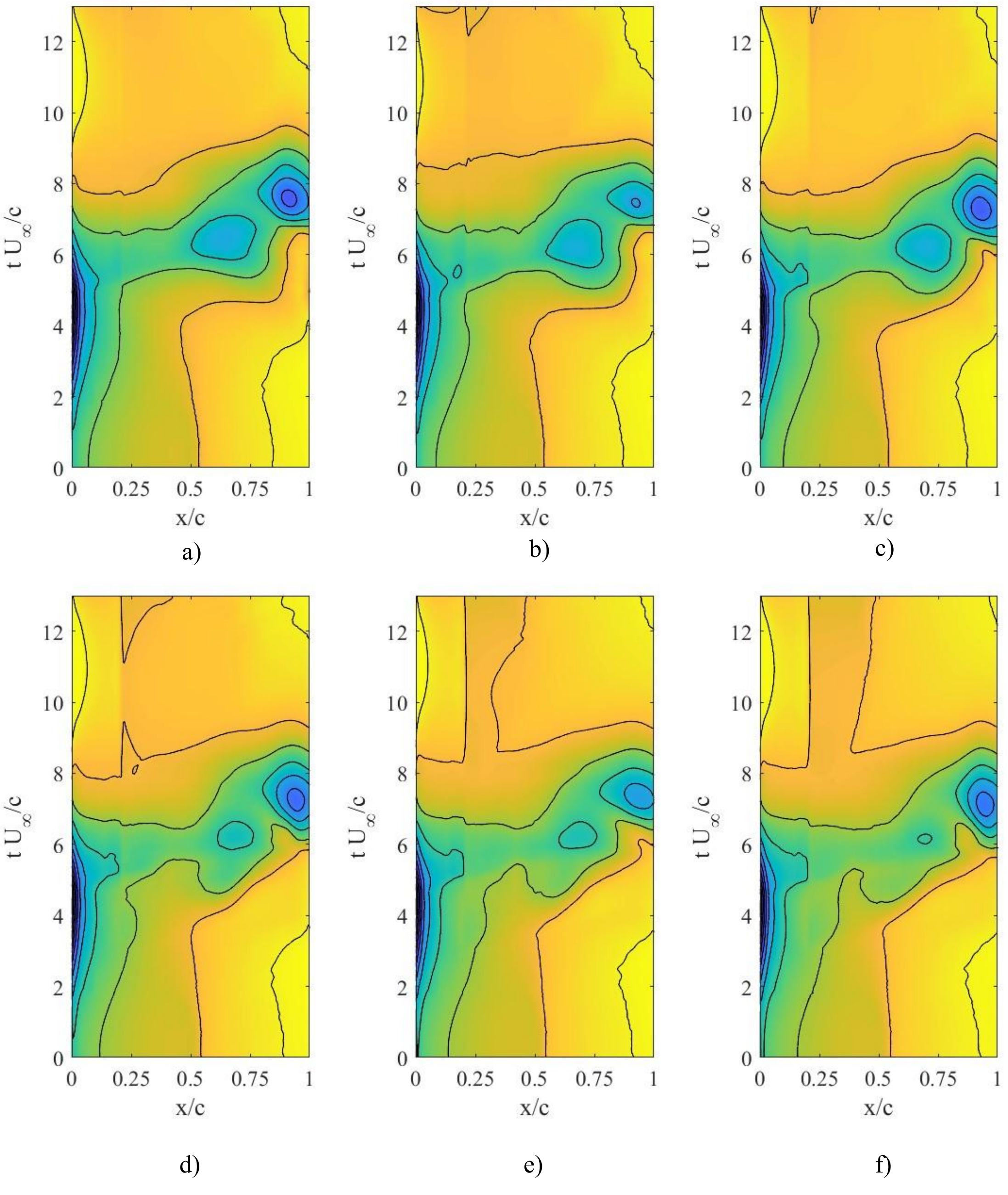

Figure 59. *Space-time pressure coefficient distribution contours along the aerofoil suction side for jet cases at* $C_I = 0.8$. β *varies in ascending order from a) to f). Contours are coloured between* $-3 \leq C_P \leq 0.1$.

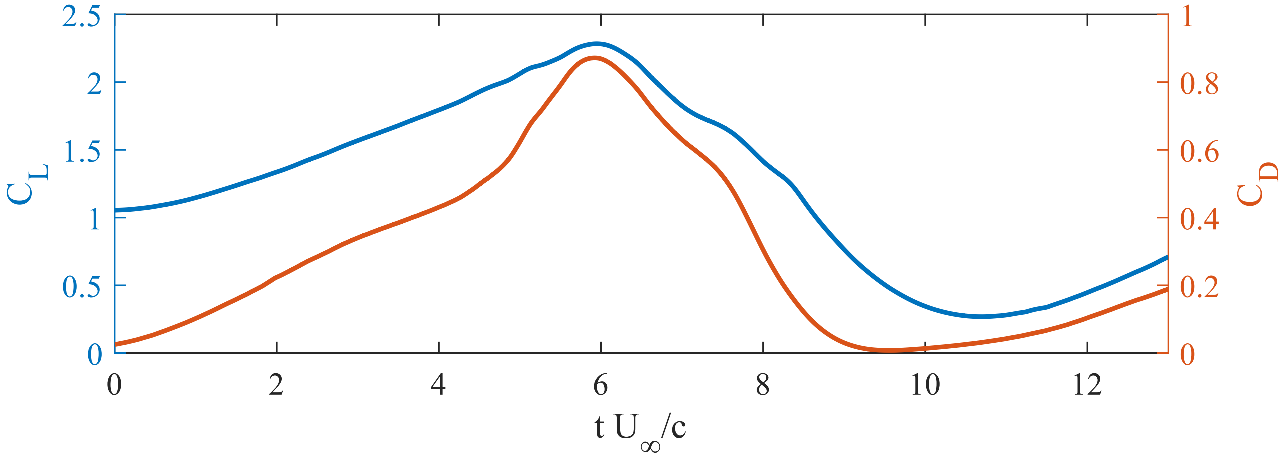

Figure 60. *Time resolved lift and drag coefficient traces corresponding to the jet-off baseline study. This data is used to compute the* ΔC_L *and* ΔC_D *profiles in figures 37 and 38, respectively.*

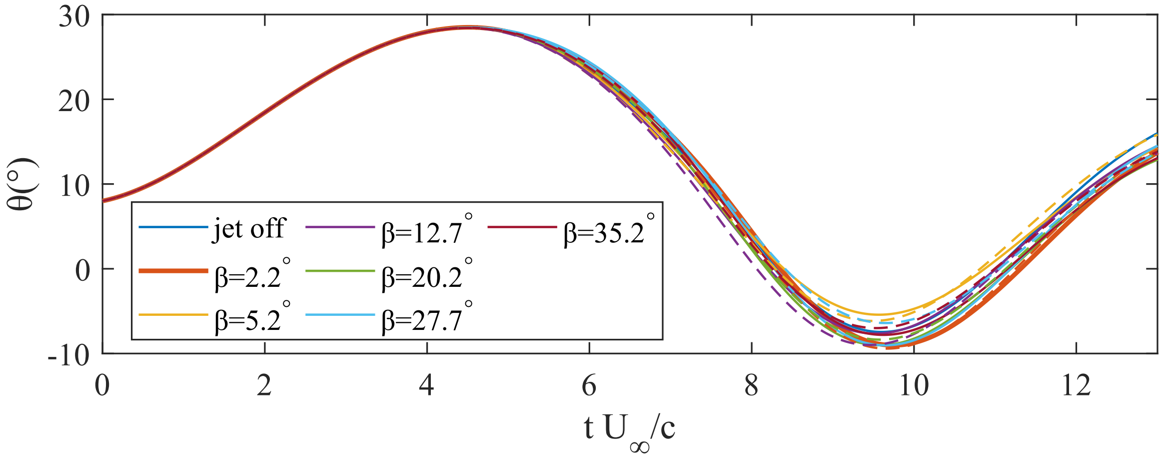

Figure 61. *Time resolved lift pitching angle trace for all cases. Bold and dashed lines correspond to* $C_I = 0.5$ *and* $C_I = 0.8$*, respectively.*

A.4 Tufts Visualisation

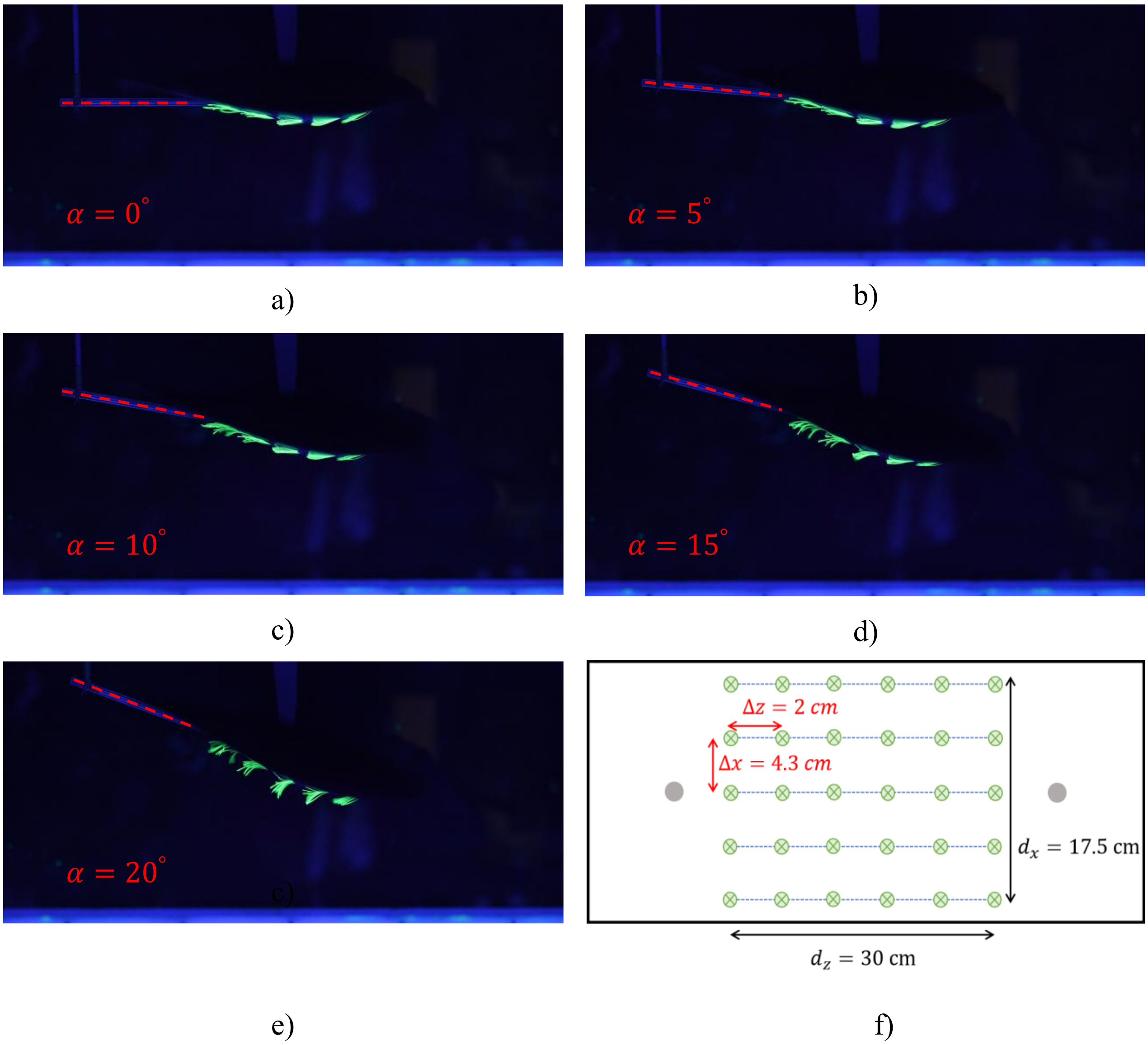

Figure 62. *NACA 63(3)418 cross sectional tufts visualisation of flow separation when increasing the static angle of attack. Figure f) represents a schematic layout of the tufts grid along the wing suction side.*

Appendix B

B.1 Correction 1

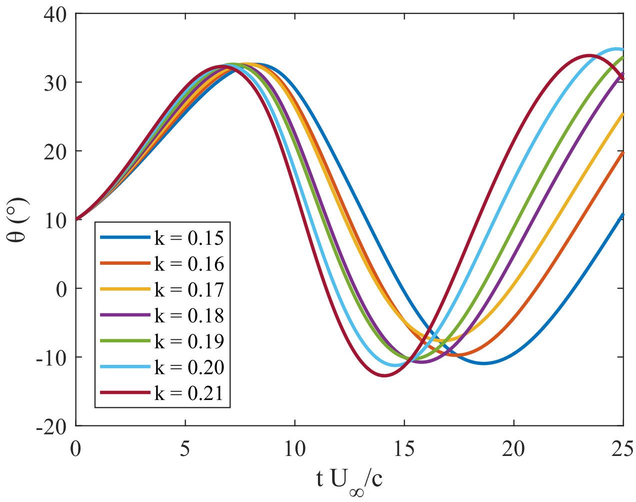

Figure 63. *Pitching angle trace versus time for NACA 63(3)418 aerofoil at mean incidence angle of* $\alpha = 10^{\circ}$.

In correspondence with figure 15, the pitching angle traces are presented in figure 63 for the parametric range $k = 0.15 - 0.21$. The x-axis is limited to a single cycle for the case of $k = 0.15$ to exemplify how a mapping between $\varphi = 0^{\circ} - 360^{\circ}$is constructed in figure 15. The primary reason why C_M and C_L do not reach their initial state over a single pitching cycle is due to a well-known hysteresis effect where complete state recovery is delayed. This lag in boundary layer recovery is what gives rise to a negative aerodynamic damping coefficient that permits the single degree of freedom flutter. Additionally, it is common to ignore initial transients within dynamic stall or stall flutter related research and simply conduct phase averaging over many ($N \geq 10$) cycles. This practice tends to smear cycle-to-cycle variability as it assumes a phase-locked behaviour which may not be wholly representative of the instability dynamics. Within this transient regime though, the difference between static and dynamic aerodynamic integral effects is evidently pronounced as per the discrepancy in C_M and C_L at 0° and 360°.

B.2 Correction 2

Regarding section 5.1, a Strouhal number of $St = 1.44$ is reported as the dominant vortex shedding frequency associated with the static NACA 63(3)418 aerofoil at $\alpha = 15^{\circ}$. If the projected aerofoil length, $c\sin(\alpha)$, is instead utilised as the characteristic length scale for equation 51 then $St = 0.373$. This value is of a much more comparable order to results published by Chang et al. (2022) where $St \approx 0.175$ was reported for a NACA 0012 aerofoil operating at $\alpha = 15^{\circ}$ and $Re_c = 10{,}000$. Two potential sources of error with our measurements may be attributed to the proximity of the probe location to the trailing-edge and double counting of wake events which grants the impression of a higher shedding frequency. If this adjusted Strouhal frequency is divided in half, then $St = 0.185$ which aligns well with

Yarusevych et al. (2009) who reported $St \approx 0.2$ for a NACA 0025 aerofoil at $\alpha = 10^{\circ}$ and $Re_c = 100{,}000$. They also utilised the chord projection length onto the cross-stream plane.

B.3 Correction 3

Figure 35 demonstrates the effects of the jet orientation angle on the static aerodynamic lift and pitching moment under constant blowing conditions. Most notably, as β increases the lift to drag ratio tends to deteriorate which is unfavourable for most real-world systems. This is the result of the constant blowing jet acting to deflect the attached boundary layer which pre-emptively stalls the aerofoil. One potential reason for this degraded aerodynamic performance is that our parametric range is restricted to a singular jet location and jet intensity that is inadequate at static conditions. In fact, the aerodynamic benefits or losses attributed to constant blowing can vary quite dramatically based on the operational regime. For example, Wang et al. (2022) showed that a perpendicular steady jet at $\frac{x}{c} = 0.2$ can delay the static stall angle of attack by a maximum of 2° while slightly increasing the lift coefficient compared to baseline measurements. Conversely, Müller-Vahl et al. (2015) demonstrated performance loss for a jet at $\beta = 20^{\circ}$ and $\frac{x}{c} = 0.05$ due to insufficient boundary layer re-energization at low injection rates. See figure 64 for a comparison of these two studies that have been sourced from the original work.

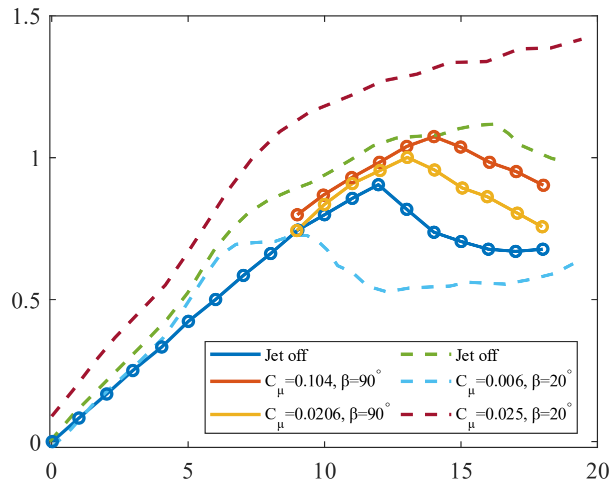

Figure 64. *Static aerodynamic lift trace with perpendicular surface blowing for NACA 0012 aerofoil (Solid and circles). Sourced and adapted from Wang et al. (2022). Quasi-static aerodynamic lift traces with $\beta = 20^{\circ}$ for NACA 0018 aerofoil (Dashed). Sourced and adapted from Müller-Vahl et al. (2015).*

The sensitivity of tuning jets to perform optimally in both static and dynamic environments pose a difficult challenge in real-world applications. For this reason, we have proposed (Chapter 6) that actuated jets may be a more favourable and robust flow control authority that does not inherently require static aerodynamic performance gains. Rather, unsteady load alleviation can be achieved at an injection cost that is lower than what is required to maintain boundary layer attachment at static conditions. This simplifies the task of system tuning as the optimisation targets are inherently less than what is required for constant blowing control authorities that operate at both static and dynamic conditions.

B.4 Correction 4

In this work, a semi-implicit integration scheme is utilised to advance the momentum equation. To clarify how this scheme works, we consider the prediction step for the discrete x-momentum equation where the convection and auxiliary source terms have been combined into the right-hand-side, RHS, and is treated explicitly in equation 61. $\widetilde{D}$ and D' refer to the wall normal (j) and remaining (i,k) flux contributions of the diffusive term. The convective fluxes were discretised using a second-order linear interpolation scheme and no flux limiter or artificial damping was applied.

$$\frac{u^{n+1}-u^{n}}{\Delta t}V_p = RHS(u^n,u^{n-1}) - G(p^n) \quad \widetilde{D}(u^n,u^{n+1}) \quad D'(u^n,u^{n-1})$$

RHS and D' terms are treated using the Adams-Bashforth scheme while $\widetilde{D}$ is treated via Crank-Nicholson to form a tridiagonal system of equations.

B.5 Correction 5

In section 3.5, it was claimed that a minimum of $t\frac{U_\infty}{c} = 20$ time units was sufficient to purge initial transients from the computational domain prior to computing the time-averaged aerodynamic loads C_L and C_D. Note that in some cases this threshold was extended as needed throughout the project to ensure that statistical stationarity was observed. To address this claim, we present the time-resolved C_L profile for the case of a NACA 63(3)418 aerofoil operating at $\alpha = 8^\circ$ in figure 65. Unfortunately, the original source data to compute figure 10 was deleted as the HPC administrator requested to purge unnecessary data from the cluster throughout this PhD project. The strategy throughout my candidacy was to retain all information and supplementary data prior to publication approval. Once a manuscript was accepted for publication, then auxiliary data was purged to begin the next set of simulations, parametric study, tests, etc. as to not exceed the allocated storage limit on both local and shared drives. Only data immediately presented in the publications and some relevant field files were retained due to the expense of storing high-fidelity LES data. For this reason, figure 65 only serves as a representative case of statistical stationarity that was utilised prior to actuated jet scenarios.

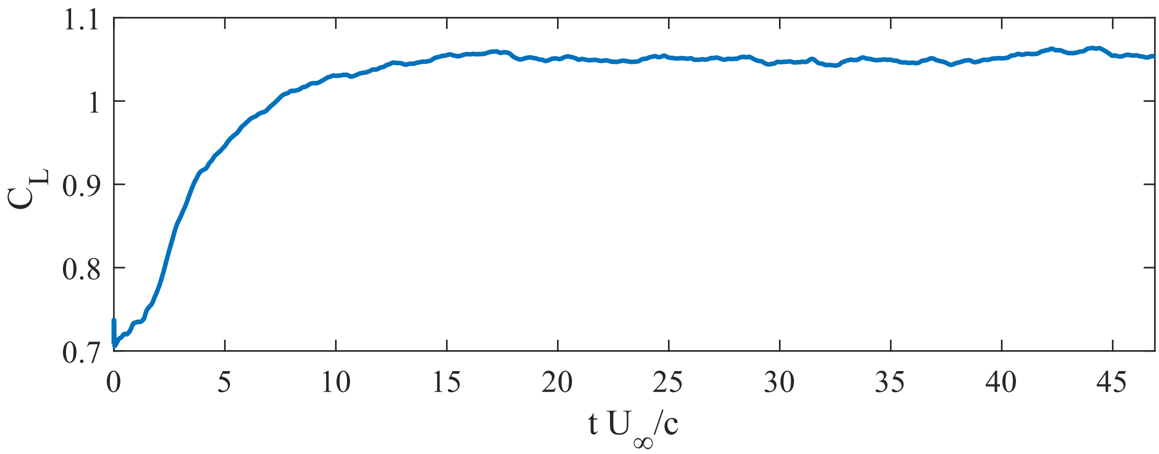

Figure 65. *Static aerodynamic lift versus non dimensional time for NACA 63(3)418 aerofoil at* $Re_c = 100{,}000$ *and* $\alpha = 8^\circ$.

It can be observed that the initial simulation transient ends just ahead of $t\frac{U_\infty}{c} = 20$ time units indicating that this timestamp is sufficient to start collecting time-averaged statistics. To clarify, this timestamp serves as a minimum simulation time across all parametric cases reported here. In practice though, simulating beyond $t\frac{U_\infty}{c} \geq 30$ was standard practice to safely ensure initial transients would not pollute the dynamic stall process during these single shot pitching cycles.

B.6 Correction 6

An example of a grid utilised throughout this work is provided in figure 66. This grid reflects an updated form of the original M4 mesh (Table 2) where grid biasing was added towards the aerofoil surface to aid with flow control related studies. Specifically, grid biasing was added to ensure a smooth pressure distribution around the jet boundary condition where high streamwise velocity gradients were present. Additionally, a deformable trailing-edge flap was initially constructed as a candidate flow control device to be used in our parametric studies.

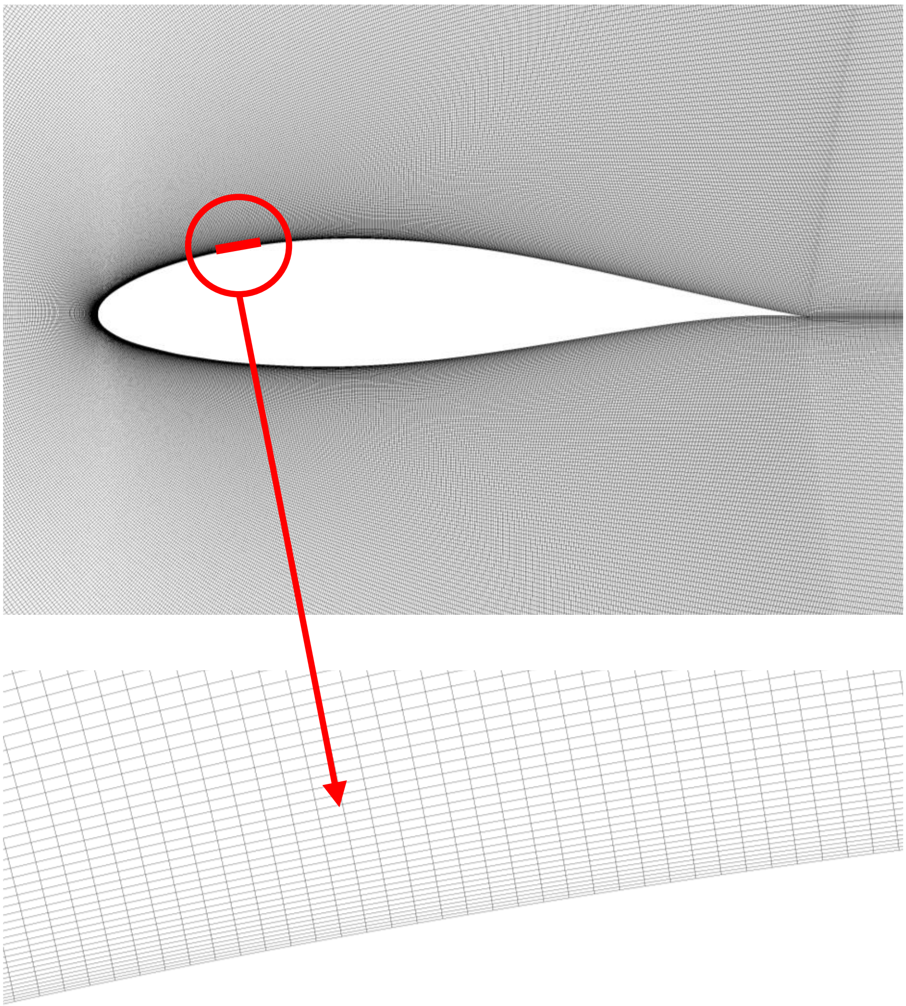

Figure 66. *M4 grid with biasing towards aerofoil surface. Dirichlet jet patch highlighted in red (top) and zoomed in (bottom).*

This necessitated the use of a direct forcing method applied between $\frac{x}{c} = 0.5$ and $\frac{x}{c} = 1$ where grid biasing was required to ensure a fine interpolation stencil that accurately resolves the immersed boundary. Despite this control authority being discarded throughout my candidacy, the biased grid was maintained as $\overline{x^+} \leq 14.22$, $\overline{y^+} \leq 0.938$, and $N = 42e{+}6$ which was sufficiently converged as reported in section 3.5.

B. Correction

It should be noted that scrutinising wall quantities such as C_L and C_D for the purpose of grid independence in dynamic stall or stall flutter related research is quite standard practice within the literature. For example, Zolghadr and Khoshnevis (2023) performed their mesh independence study by comparing the static lift coefficient at $\alpha = 0^{\circ}$ and $Re_c = 153{,}000$. They reported convergence at $N = 26{,}000$ cells which also translated to convergence in dynamic simulations operating at a reduced frequency of $K = 0.12$. Similarly, Watrin et al. (2012) conducted their grid evaluation utilising a static aerofoil configuration ranging between $\alpha = 0^{\circ} - 25^{\circ}$ prior to conducting their dynamic simulations for a NACA 0012 aerofoil at a reduced frequency of $K = 0.1$.

B. Correction

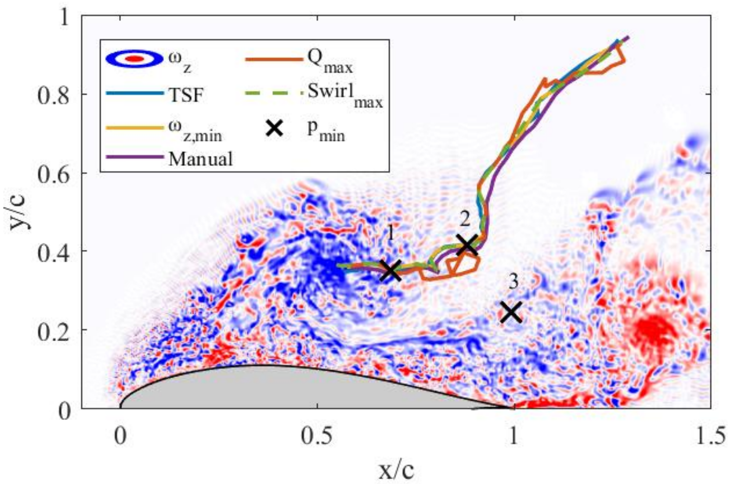

Figure 67. *Adaptation of figure 56 with the addition of a pressure minimum criteria for identifying the LEV at three successive but non-consecutive snapshots.*

The usefulness of the TSF was critiqued as the searching segment of our vortex tracking pipeline (chapter 7) could be quite time consuming despite the application of down-sampling. One suggestion was to utilise the pressure minimum to track the LEV as this may have similar accuracy but at a reduced computational cost. To evaluate this, we extracted the global pressure minimum at several snapshots to compare with our TSF based tracking pipeline. These results are presented in figure 67 where the 'x' markers identify the expected LEV at three successive but non-consecutive snapshots. During the adolescent LEV stages, p_{min} is a sufficient criterion to track the vortex core as it aligns quite well with the TSF based trajectory. Beyond the LEV detachment though, an introduction of counter rotating fluid about the trailing edge tends to blur the classification between an LEV and TEV. The interaction between these two coherent structures makes the global pressure minimum an insufficient criterion to adequately distinguish between the respective vortices as evidenced by the ‘x’ marker at timestamp 3 in figure 67. Further post-processing is likely required to help differentiate between the LEV and TEV such as a truncated search region, pressure thresholding, or coordination with alternative Eulerian based vortex definitions. One of the inherent benefits of our method is that the Vietoris-Rips complex utilised to compute the TSF can be constructed from any combination of field data. For example, we utilised u, v, p and ω_z point data to construct our complex in section 7.2 which naturally incorporates the pressure minimum signature into our defined template.